© Copyright 2022

Ruoming Peng

Electromechanically control the optoelectronic properties of 2D semiconductors

Ruoming Peng

A dissertation

submitted in partial fulfillment of the

requirements for the degree of

Doctor of Philosophy

University of Washington

2022

Reading Committee:

Mo Li, Chair

Arka Majumdar

Xiaodong Xu

Program Authorized to Offer Degree:

Electrical and Computer Engineering

University of Washington

Abstract

Electromechanically control the optoelectronic properties of 2D semiconductors

Ruoming Peng

Chair of the Supervisory Committee:
Professor Mo Li
Electrical and Computer Engineering

2D materials have exhibited rich distinct properties, which can cover a broad optical spectral range with strong light-matter interactions. The properties of 2D materials are very sensitive to the local environment so their properties are easily controlled by the external field. In this thesis, I will mainly discuss how the electrical and mechanical methods can control the interlayer coupling of 2D materials and modulate their optoelectronic properties. I will show two different material systems that can be controlled by external approaches.

In the first part, the electric field is utilized to modulate the optical absorption of black Phosphorus (bP) thin film. The modulation peaks of the bP flakes are related to the subband transitions which also show strong layer dependence. With 9 nm bP flake, the transitions with the same and different

band indexes have been observed and more than 5 percent modulation of absorption has been demonstrated in the thin film device.

This strong modulation of the bP absorption leads to optoelectronic applications such as integrated mid-infrared photodetectors and modulators. For the second part, we achieve the photodetection at the mid-IR region with the responsivity of 2.5 mA/W. Also, the 9 dB/mm modulation depth has been demonstrated in the straight waveguide device and more than 40 dB/mm are predicted based on the simulation of the ideal fabricated sample.

In the last part, I will show that the piezoelectric field of the surface acoustic wave can strongly interact with the bilayer transition metal dichalcogenides (TMDCs) so that the exciton can be spatially manipulated by the propagating acoustic waves with the propagation length exceeding 20 μm. Both temperature and power-dependence of the SAW devices have been characterized that we clearly resolve the transition from exciton localization to transport regime. Due to the strong acoustic modulation, more than 2 μm transport length has been achieved even at room temperature. This acoustic approach in general can also be applied to other physical systems such as Moire heterobilayers ($MoSe_2$/WSe_2) by considering the vertical dipole moment of the Moire exciton.

TABLE OF CONTENTS

List of Figures iv

List of Tables xiv

Chapter 1. Introduction 1

1.1 Two-dimensional material optoelectronics 1

1.2 Black Phosphorus for infrared photonics 3

1.3 Transition-metal dichalcogenides for excitonic devices 4

1.4 Electrical and strain modulation of the 2d materials 5

1.5 Scope of this thesis 10

Chapter 2. Electro-optic modulation in few-layer Black Phosphorus 12

2.1 Optoelectronic properties of black phosphorus 12

2.1.1 Anisotropic optoelectronic properties of black Phosphorus 12

2.1.2 Layer dependent properties of black Phosphorus 14

2.1.3 Optoelectronic devices based on few-layer black Phosphorus 16

2.2 Mechanisms for electro-optical modulation 19

2.2.1 Franz-Keldysh effect in solid 19

2.2.2 Quantum-confined Franz-Keldysh effect in black Phosphorus 20

2.3 Device fabrication and measurement schematics 22

2.4 Electro-optic modulation in few-layer black Phosphorus 24

2.5 Numerical analysis for few-layer black Phosphorus 28

2.6 Layer-dependent optical modulation of few-layer black Phosphorus 33

2.7 Conclusion and outlook 36

Chapter 3. On-chip integrated black Phosphorus devices for mid-IR application 37

3.1 Motivation and introduction 37

3.2 Working principle and fabrication 41

3.3 Numerical Simulation for integrated black phosphorus device 42

3.4 Measurement Schematics 44

3.5 Integrated black Phosphorus photodetector 45

3.6 Integrated black Phosphorus electro-optical modulator 47

3.7 The integrated platform for high-extinction modulation 49

3.7.1 Multi-pass waveguide design 49

3.7.2 Ionic liquid for stronger field modulation 50

3.7.3 The plasmonic nanogap for enhanced light-matter interaction 51

3.8 Conclusion and outlook 53

Chapter 4. Transport of 2D excitons with surface acoustic wave 54

4.1 Introduction 54

4.1.1 Excitons in Transition metal dichalcogenide 54

4.1.2 2D Excitonic transistor 58

4.1.3 Review of the surface acoustic wave and its application 60

4.2 Analysis of acoustic wave modulation 62

4.3 Device fabrication and measurement schemes 70

4.3.1 Device Fabrication 70

4.3.2 Measurement setup 70

4.4 Transport of 2D exciton at 100 K 72

4.5 Power dependent exciton transport at 100 K 75

4.6 Theory of exciton transport driven by surface acoustic waves 77

4.7 Temperature-dependent exciton transport 79

4.8 Conclusion and outlook 82

Chapter 5. Conclusion and outlook 84

5.1 Summary of this thesis 84

5.2 Future perspectives 86

Bibliography 89

Appendix A 105

LIST OF FIGURES

Figure 1.1. 2D materials covering a broad spectral range. Electromagnetic spectrum. Applications that utilize the different spectral ranges are presented in the top portion of the panel. NIR, MIR, and FIR indicate near-, mid-, and far-infrared, respectively. The atomic structures of hBN, MoS_2, bP, and graphene are shown in the bottom of the panel, left to right. The crystalline directions (x and y) of anisotropic bP are indicated. 2

Figure 1.2. Optical properties of few-layer black Phosphorus. (a) The lattice structure of few-layer BP, showing the puckered hexagonal crystal with two nonequivalent directions: AC (x-direction) and ZZ (y-direction). (b) Optical image of a representative 6L sample. Scale bar, 20 μm. (c) The real part of the optical conductivity σ for the 6L sample in b, in the unit of the universal optical conductivity $\sigma_0=\pi e^2/2$ h, with polarization angles of incident light from 15° to 90°, in steps of 15°. The marks E11 and E22 denote the first and second subband transitions, asterisks (*) denote hybrid transitions. 4

Figure 1.3. Valley-dependent carrier transport. a) The 2D hexagonal crystal structure of a monolayer transition metal dichalcogenide (TMDC) composed of transition metal atoms (blue) and chalcogen atoms (orange) resembles that of graphene but with broken inversion symmetry. A side view shows the 3D structure. The hexagonal Brillouin zone is shown labeling the Γ point and the two inequivalent +K and −K points. b) Valley-dependent optical selection rules for interband transitions in monolayer TMDCs. σ+ polarized light couples to the +K (red) valley, and σ− polarized light couples to the −K (blue) valley. 5

Figure 1.4. Gate and bias tuned photoresponse of the BP photodetector. a) Source-drain current versus bias voltage when optical signal is off (black line) and at various power levels (red: 480 µW; blue: 957 µW; green: 1.91 mW). b) Photocurrent versus gate voltage at various fixed bias voltages. The direction of the photocurrent changes as the gate voltage increases from negative values (where the BP has low doping) to positive values (where the BP is highly n-doped). The optical power in the waveguide is fixed at 1.91 mW. 6

Figure 1.5. Work mechanisms of bP electro-optic modulation. a) Schematic, energy band diagram, and wave functions of 5 nm thick BP QW with Ns = 1.4×10^{10} (intrinsic regime), 1×10^{12}

(QCFK regime), and 5×10^{12} cm^{-2} (BMS regime). Results are computed through self-consistent Schrö dinger-Poisson calculation. The energy zero is chosen to be at the bottom and center of the conduction band. (c) Energy dispersion diagrams for the lowest/highest conduction/valence subband under doping conditions listed above. The level of carrier occupancy is indicated by the shaded region. The corresponding formula for calculating Eg is also listed. 7

Figure 1.6. Calculated electronic band structure along the K-Γ line at zero (a) and 0.3 V/nm (b) vertical electric field. 9

Figure 1.7. Schematic representation of the strain-induced actively tunable bandgap of bP. Compressive and tensile strains induce redshift and blueshift of the bP bandgap, respectively. 10

Figure 2.1. In-plane anisotropic properties of black phosphorus. (a) Angular dependence of the DC electrical conductance of a black phosphorus transistor. (b) Angular dependence of the relative optical extinction measured on the same flake displayed in (a). (c) Angular-dependent photoluminescence yield of a black phosphorus flake with laser excitation (λ = 532 nm) polarized along the zigzag direction, armchair direction, and a 45° direction. (d) Calculated angular dependence of the black phosphorus Young's modulus. The calculation predicts that the zigzag direction is about four times stiffer than the armchair direction. 13

Figure 2.2. Layer-dependent band structure of black Phosphorus. (a) Observed optical resonance energy (solid squares) compared with the prediction (solid curves) by the phenomenological 1D tight-binding model. Empty squares are the interband optical transitions predicted by the tight-binding model that fall outside our measurement range. The lower and upper limits of our measurement range are marked by horizontal dashed lines. (b) Calculated GW quasiparticle band structure of monolayer, bilayer, trilayer, and tetralayer phosphorene (from left to right). Few-layer phosphorene is encapsulated between a sapphire substrate and an hBN capping layer in the calculation. As the number of phosphorene layers increases, the direct band gap at Γ decreases, and additional high energy subbands (marked by I, II, and III) emerge. 15

Figure 2.3. Black Phosphorus based nanodevices. (a) Ambipolar field-effect transistor. (b) Electrostatically gated PN junction displaying photovoltaic effect. (c) Nanoelectromechanical

resonator vibrating in the very-high frequency regime. (d) High-frequency photodetector coupled to a silicon waveguide. (e) Inverter amplifier based on MoS_2 and black phosphorus transistors, demonstrating the potential of black phosphorus for logic circuits........ 18

Figure 2.4. Performance of the GeSi EA modulator. (a) Extinction ratio at –7 V bias and insertion loss at 0 V bias as a function of wavelength. The effective operating spectrum range is 1,539–1,553 nm. (b) Dynamic EO response of the device in the frequency range of 10 MHz to 10 GHz with a dynamic driving voltage (Vpp) of 3 V. No frequency roll-off is observed up to 0.7 GHz, indicating that the device can still achieve an 8-dB extinction ratio at 0.7 GHz with Vpp = 3 V. The 3-dB bandwidth is 1.2 GHz, and the corresponding extinction ratio is 4 dB. 20

Figure 2.5. Schematic energy band diagram of BP three sample biases, $V_g < 0$, $V_g = 0$, and $V_g > 0$. The dashed lines in panel d mark the energies of each sub-band. The solid lines depict the wave function in each sub-band. The black dotted line marks the Fermi level. The red/blue/green vertical arrows in panel d show possible transitions that may contribute to the modulation level extrema observed. 22

Figure 2.6. Black phosphorus electro-optic modulator. (a) Schematic illustration of the BP modulator, featuring the normally incident mid-IR laser beam and the lightly p-doped silicon substrate as the back gate. The BP flake is oriented with the arm-chair (AC) crystalline axis along the x-axis and the zigzag (ZZ) crystalline axis along the y-axis. (b) Optical microscope image of the BP modulator. (c) Height profile (along the dashed line in b) obtained with atomic force microscope shows that the BP thickness is about 9 nm which corresponds to 17 layers. 23

Figure 2.7. Schematics of the mid-infrared BP modulation measurement setup. The incident light is divided into two paths which are locked with different frequencies by the chopper.24

Figure 2.8. Measurement of mid-IR electro-optic modulation in BP. (a) Measured extinction of the transmitted light for 9 nm BP device at three values of gate voltages $V_g = 0, \pm 150$ V. The incident light is linearly polarized with the electric field parallel to the AC crystalline axis. (b) The modulation level $\Delta T/T(0)$ for 9 nm thick BP at $V_g = \pm 150$ V for light polarization along AC (solid lines) and ZZ (dashed lines) crystalline axes. A maximal modulation of about 3% is obtained at a photon energy of 0.38 eV. (c) The modulation level measured as functions

of energy and gate bias for 9 nm thick BP. Three characteristic peaks can be observed at Ea = 0.38 eV, Eb = 0.43 eV, and Ec = 0.5 eV. 26

Figure 2.9. Theoretical calculation of electro-optic modulation for 9nm thick BP at room temperature. (a) The transition energy E_{ij} (left panel) and the wavefunction overlap S_{ij} (right panel) as a function of hole concentration ρ_h. (b) The real part of conductivity σ_{ij} (normalized to $\sigma_0=e^2/4\hbar$, the universal conductivity of graphene) for various transitions between ci and vj versus photon energy. (c) Contour plot of the modulation of the transmission as functions of energy and hole concentration. In (b) and (c), the broadening is $\eta = 6$ meV, except for the red lines in the top panel (b) where $\eta = 20$ meV. 32

Figure 2.10. 2D modulation mapping of three other devices with different BP thicknesses. The max modulation of 5% has been observed in 13 nm bP flake. The modulation mapping results for bP flakes varied significantly with flake thickness. 34

Figure 2.11. Layer dependence of electro-optic modulation in BP. (a) Gate voltage dependence of E_{11} and E_{22} in 9 and 12 nm thick BP. Squares denote the transition energy at zero gate voltage, obtained via interpolation of the modulation extrema at ±20 V. Contour plots of (b) E_{11} and (c) E_{22} transitions as functions of BP layer number and hole concentration computed via numerical methods. (d) Extracted transition energies at zero gate voltage vs BP layer number. The solid lines represent the data computed via eq 2.1. 35

Figure 3.1. Optical transmittance of the atmosphere (%/km). The atmosphere offers two main transparency windows located at 3-4 μm and 8-10 μm. 39

Figure 3.2. The absorption spectrum of the varied gas and organic molecules. The gas and organic molecules have strong vibrational absorption within the mid-IR region. 40

Figure 3.3. Device schematic and work principles. (a) Schematic illustration of the integrated bP modulator, featuring the guided mid-IR light by the silicon waveguide. The Si also performs as the back-gate electrode to modulate the optical properties of bP thin film. (b) Working principles of the bP modulator. Both Pauli blocking and the QCFK effect can contribute to the optical modulation of bP thin film. (c) Optical image of the integrated bP device. The bP flake is oriented with the armchair (AC) crystalline axis along the light propagation direction. 41

Figure 3.4. Simulation of the integrated bP devices. (a) Schematic structure of the free-space devices. Considering the multilayer structures, the extinction coefficient can be calculated from the transmission spectrum. (b) The calculated extinction coefficient of the bP thin film at different gate voltages. The optical absorption of bP is strongly modulated by the electric field especially in the optical spectrum range around 0.38 eV. (c) The simulation of the waveguide integrated device. The anisotropy of bP has been included in the simulation that the TM mode of the waveguide has a large mode overlap with bP thin film. 43

Figure 3.5. Measurement Schematics. (a) The setup design for the photodetection and modulation measurements of integrated bP device. The phase retarder with a polarizer is used to control the output polarization of fiber to be aligned with the TM mode of the Si waveguide. (b) The optical image of the inverse tapered structures. Inset: SEM image shows the zoom-in feature of the tapered end where the width of the tapered end is about 150 nm.................. 45

Figure 3.6. Integrated *bP* device for photodetection. (a) The responsivity spectrum of *bP* photoresponse. There are three resonances in the responsivity spectrum which are corresponded to the subband transitions of *bP* thin film. (b) The power-dependent photocurrent measurement of integrated *bP* device. The device can achieve the photodetection at sub μW regime. 46

Figure 3.7. Integrated *bP* device for optical modulation. (a) The measurement schematic for the integrated *bP* device. This device can be operated as both the photodetector and modulator. (b) The modulation level is measured as the function of the wavelength and applied gate voltage, featuring the max modulation of about 8 dB/mm. (d) Measured modulation at gate voltage $\pm 10\ V$, the device shows broadband modulation in the mid-IR range from 2800 nm to 3400 nm. 47

Figure 3.8. Characterization of the iL-gate devices. The optical images of (a) the multi-pass waveguide and (b) the bP-integrated waveguide. BP is indicated with the red-dashed line. The green square region is planarized with SiO_2. Scale bar: 20 μm. (c) The cross-sectional schematics of the iL-gate device. Inset: Field-effect modulation of BP conductance. (d) Transmission changes normalized to that of zero gate voltage scanned around 3-um at different gate voltages. The maximum modulation occurs as 10% at 2.98 um between gate voltages of −1 and 0.5 V. 50

Figure 3.9. Integrated plasmonic devices for enhanced optical modulation. a) Schematics of MIM-WG simulation. Scale bar: 40 nm. The electric field is highly confined near the edges of gold and BP nearby, enhancing light-matter interaction. b) The modulation strength, defined in the main text, is calculated with varying gold thickness and slot width. c) Figure of Merit, defined in the main text, considering both modulation depth and insertion loss. 52

Figure 3.10. Device schematic for the integrated plasmonic device. (a) 3D illustration of the plasmonic nanogap device. (b) The SEM image of the fabricated plasmonic device. The gap of the plasmonic device is 50 nm. 52

Figure 4.1. Excitonic device based on the transition metal dichalcogenides. (a) The waveguide integrated LED and photodetector based on monolayer $MoTe_2$. In LED mode, the light emitted from the p–n junction propagates through the waveguide and is coupled out at the grating coupler. In photodetector mode, incident light is coupled to the waveguide through the grating coupler and is detected by the $MoTe_2$ p–n junction. (b) Nanocavity laser based on the monolayer WSe_2. A continuous-wave nanolaser operating in the visible regime is thereby achieved with an optical pumping threshold as low as 27 nanowatts at 130 kelvin. (c) Bose-Einstein condensation of the exciton-polariton in an atomically thin crystal. Exciton–polaritons emerge from an atomically thin crystal of $MoSe_2$ embedded in a dielectric microcavity under optical pumping at cryogenic temperatures. (d) Strain and defect-engineered WSe_2 single-photon emitter. It enables site-controlled single-photon emission up to 150 K. 56

Figure 4.2. Interlayer valley excitons in 2D semiconductor heterostructures. (a) Energy-level diagram showing type-II band alignment for a typical MoX_2–WX_2 heterojunction. Ultrafast interlayer electron transfer to the MoX_2 or hole transfer to the WX_2 results in the formation of interlayer exciton states. (b) Illustration depicting spatially indirect, interlayer excitons in a MoX_2–WX_2 heterojunction. The oriented dipole moments out of the plane cause strong exciton repulsion as well as large Stark shifts under applied electric fields. (c) Map of photoluminescence emission as a function of applied gate voltages V_{TG} and V_{BG} when sweeping at constant doping. 57

Figure 4.3. Exciton transport in a van der Waals heterostructure. (a) Schematic of the device structure illustrating the top and bottom split gates, as well as electrical connections. (b) (c)

Numerically simulated exciton energy profile (red line) in the off (b, VTG = 0 V, VBG = −7 V) and on (c, VTG = 0 V, VBG = 0 V) states of the excitonic transistor. (d) (e) Real-space CCD images of the emitted PL intensity for the off (b) and on (c) states. The black dashed circle indicates the laser spot. Scale bar, 2 μm. 59

Figure 4.4. Control 2D potential energy of interlayer excitons by the electrical field. (a) Schematic structural diagram of one excitonic transistor. (b) Schematic of exciton energy offset for exciton dynamic regimes of trap, free diffusion, and spreading when applying negative (top), zero (middle), and positive (bottom) gate voltages, respectively. (c to e) Real-space emission intensity map for exciton trap, diffusion, and spreading, corresponding to gate voltage VG = −9, 0, and 11 V, respectively. The white dashed lines indicate the bottom electrode edges. Scale bars, 2 μm. (f) Emission intensity profiles across the electrode were extracted from the real-space emission intensity maps. The excitation spot was focused on the center of the electrode. The excitation power is ~200 nW operated at 532 nm............................ 60

Figure 4.5. Application of surface acoustic wave to different physical systems. (a) Propagating phonons coupled to an artificial atom. nonclassical interaction between surface acoustic waves and an artificial atom has been demonstrated in the regime of strong coupling. (b) Schematic of our diamond SAW device. The interdigital transducers (IDTs) generate acoustic waves due to the piezoelectric response of aluminum nitride (AlN). The modulation of SiVs in the diamond are probed using a focused laser beam. (c) Schematic of the experimental set-up. An interdigital transducer (IDT) launches a SAW train towards the single-electron circuit to remotely drive the electron transfer. (d) Photonic crystal nanocavity, deformed by surface acoustic wave (SAW). A periodic modulation of the optical mode exceeding eight times its linewidth has been resolved. (e) Samples for indirect exciton (IX) transport by surface acoustic waves (SAWs). *IX* transport by the moving modulation of the conduction (CB) and valence bands (VB) in a DQW. 61

Figure 4.6. The shape and electric profiles of the SAW on the $LiNbO_3$ substrate. a) The geometry profile of the SAW. The SAW is confined along the surface of the $LiNbO_3$ substrate. b) The electric field profiles along the propagation direction. The SAW carries a large perpendicular electric field which can interact with the interlayer exciton devices on the substrate. The periodic E field will create the periodic potential for the interlayer exciton. 63

Figure 4.7. The relation between the exciton average velocity and the exciton mobility at different SAW velocities. As you expect, the higher exciton mobility contributes to larger drift velocity. When exciton mobility is large enough, the exciton velocity will be saturated due to the limit of the SAW velocity. 65

Figure 4.8. Bilayer WSe_2 integrated with SAW devices. a. Schematic illustration of the h-BN encapsulated bilayer WSe_2 stacked with SAW devices. The IDTs generate SAW to transport the excitons in different directions. b. The propagating SAW modulates the energy of the excitons and transports them from the pump spot to the flake edge, where they recombine to generate photoluminescence. For simplicity, we only plot +z interlayer exciton in bilayer WSe_2. See S.I. for details. c, Optical microscope image of the device, with the white line outlining the bilayer WSe_2. Scale bar, 20 µm. d. The piezoelectric field profile of the SAW generated by the focusing IDT. The acoustic focal point has a waist of 3 µm and is at the edge of the bilayer WSe_2. The dotted line outlines the WSe_2 flake. Scale bar, 5 µm. e-f, The piezoelectric field distribution with (e) and without (f) the top ITO electrode. The field amplitude is calculated assuming an acoustic power density of 1mW/µm. The ITO electrode can efficiently suppress the in-plane piezoelectric field component (E_x), which causes undesirable exciton dissociation. 66

Figure 4.9. RF calibration of the IDT acoustic transducers. (a) RF reflection coefficient S11 measurement of the IDT devices. We test the IDTs with the varied number of periods N. Device with N=42 exhibits the best impedance matching according to the S11 measurements. (b) The vector analysis of the IDT resonance on a polar chart showing a strong acoustic resonance at 1.237 GHz with an on-resonance impedance 53.66 Ω+j3.77 Ω, closely matching the 50 Ω impedance of the RF source. (c) Equivalent circuit model of the IDT acoustic transducer for N=42 with component values of serial resistance R_s, shunt resistance R_l, capacitor Ce and admittance Y_a extracted from the data in (a) and (b). 68

Figure 4.10. The RF power ratio for different circuits components (Reflection, serial resistance Rs, shunt resistance $R_{l,}$ and admittance Y_a) calculated from the data in Fig.SI-11 (a) and (b). 69

Figure 4.11. The measurement setup for the exciton transport. The device is measured in the cryostat from 6 K to RT with the RF capability. 71

Figure 4.12. SAW-driven transport of IXs at 100 K. a-b, Real-space PL mapping (a), when SAW is off, and (b) when SAW is on with 6 mW power. Two bright emission spots appear at the edge of the flake and the focal point of the acoustic wave (see Figure 4.8 d) due to the SAW-driven transport of IXs. Insets: Illustration of free diffusion and SAW-driven drift of IXs. c-d, The spectral PL image at the same experimental conditions as a-b. The non-local exciton emission at the flake edge is clearly attributed to the IXs in WSe_2, which have an emission peak at 1.56 eV. e, The emission spectrum at the pump position slightly decreases when SAW is turned on. f, The emission spectrum at the flake edge position drastically increases when SAW is turned on. 73
Figure 4.13. SAW modulation of the control devices that do not have the top ITO to screen the in-plane piezoelectric field. No transport of IXs beyond the diffusion distance can be observed. Rather, the SAW piezoelectric field dissociates the IXs to free carriers to suppress the emission everywhere. 74
Figure 4.14. Acoustic power-dependent IX transport at 100 K. a-c PL images at different SAW power P_s of (a) 0 mW, (b) 4.5 mW, (c) 6 mW. The solid white line outlines the WSe_2 flake. The two bright emission spots at the edge of the WSe_2 flake highlight the SAW-driven transport of IXs. Scale bar, 10μm. d, The integrated emission intensity at the flake edge (in the area indicated by the yellow dashed box in a) depending on the SAW power P_s. The experimental data are fitted with the theoretical model that the transport exciton density exponentially depends on the square root of P_s. At low P_s, the exciton transport is diffusion-limited (blue shaded). A high P_s, SAW-driven transport is activated (red shaded). 75
Figure 4.15. Optical power-dependent measurement of exciton transport at 100 K with 6 mW SAW power. 76
Figure 4.16. Exciton transport by surface acoustic wave under disorder potential. (a) Schematic exciton gas in a trap with a characteristic depth in energy of Δ and length *L*. The exciton gas in quasi-equilibrium is shown in orange. (b) Schematic exciton gas when maximum electric potential gradient from SAW is applied, creating a shallower potential barrier on one side of the trap. The exciton population above the dotted line can travel with SAW. (c) Fitting the power-dependent PL intensity to the SAW power. 78

Figure 4.17. SAW-driven IX transport at varying temperatures. The spectral PL image of exciton transport at 6-200 K with SAW off (a, c, e, g) and on (b, d, f, h). For clarity, the data at each temperature is normalized separately. a, b, At low temperature (6K), IXs show narrow peaks as they are highly localized to recombination centers such as defects or couple strongly to local vibrational modes. SAW can delocalize the IXs so to suppress the emission. However, the transported IXs remain dark because of the reduced phonon-assisted recombination at low temperatures. c, d, At elevated temperatures (30 K), the IXs are thermalized with broad emission. SAW transport turns on with visible emission at the flake edge. e, f, At 100 K, SAW transport of IXs is most prominent as IXs have a sufficiently long lifetime and are less susceptible to defect trapping. G, h, At even higher temperatures, SAW transport, although still visible, is inefficient as exciton-phonon scattering dominates and the IX population lifetime is short. 80

Figure 4.18. Evaluation of the exciton transport at different temperatures. The exciton emission at the edge is normalized to the emission intensity at the pump center. The exciton transport reaches the maximum at 100 K. 81

Figure 4.19. Exciton transport at 290 K. The lower panels are zoomed in view of the dashed box. The exciton transport over ~2 μm can still be observed at room temperature owing to the strong SAW modulation. 82

LIST OF TABLES

Table 3.1. Overview of the mid-IR modulator 48

Table 4.1. The simulated piezoelectric field at 10 nm above the $LiNbO_3$ substrate with the top ITO electrode. 63

ACKNOWLEDGEMENTS

As time flies by, it has come to the end of my doctorate study. I still remember the moment when I join the group, I feel like a headless chicken that I have no idea what is “photonics”. I wrote down the quote by Nietzsche to encourage myself “*We should consider every day lost in which we have not danced at least once*”. There are many failures, but few successes throughout my whole Ph.D. study, but I always enjoy my everyday life in the Li group and devote myself to the study of photonics. I would not learn so much and obtained so many experiences without the help of my advisor, teachers, collaborators, friends, and family. With that, I would like to express my deep and sincere gratitude to all of them.

Foremost, I want to thank my advisor Prof. Mo Li for his instruction and support. During the last six years, I had a lot of discussions with Mo. He taught me a lot and patiently instructed me even though I have messed up in the first two years of my Ph.D. study. There were many days and nights that he discussed with me his ideas about my research projects, and I am always inspired by his motivation and passion for the research.

Also, I thank Dr. Nathan Youngblood, Dr. He Li, Dr. Huan Li, Dr. Han Zhao, Dr. Che Chen, and Dr. Qiyu Liu, the previous colleagues in our group, who are all very talented and hardworking. I enjoy the time working with them, nowadays, I still have many discussions with them about my research and career plan. Also, I want to thank the current groupmates Changming Wu, Seokhyeong Lee, Adina Ripin, Qixuan Lin, I-Tung Chen, and Bingzhao Li. They have expertise in different fields of photonics, teach and share their research experience with me a lot and give

me a broad view of the current photonics research. Especially, Changming, Seokhyeong, and Adina, my main collaborators in the group, gave me significant support to overcome the challenges of my project and make my ideas to be realized. Also, I want to acknowledge my friends Zhong Zhuang, Zhengyi Gong, Haoran Xue, Chen Zou, Jiajiu Zheng, Yupeng Zhu, Chunyao Zhao, Qichao Lu, etc. They really helped me a lot not only in life but also in research.

I sincerely appreciate Prof. Xiaodong Xu's kindness in sharing the measurement facilities in his group. I also collaborated with Jiayi Zhu in his group for the SAW modulation of the 2D materials and have discussions with many of his students. They gave me very useful guidance and help on the heterostructure fabrication and understanding of the device mechanism. Also, I would like to thank Prof. Arka Majumdar for the discussion of integrating 2D materials with photonic platforms, which help me a lot in future study and research. I appreciate that Prof. Ting Cao can join my thesis committee as GSR, I would like to thank him for his useful class on the physics of 2D materials which covered the basic concepts of the topology and optical property in low-dimensional systems. I had a lot of discussions with prof. Cao in regarding to the measurement results and career plan which help me to develop my own research plan.

Most of my work was conducted at the Molecular Analysis Facility, the National Nanotechnology Coordinated Infrastructure site at the University of Washington; UW NNCI Washington Nanofabrication Facility (WNF), and University of Washington (UW) Molecular Engineering Materials Center (MEM·C). I would like to thank all the technicians who have helped to provide those excellent facilities.

I would like to express my gratitude to my parents and my grandparents for their endless love, patience, encouragement, and support. They brought me up and dedicated their lives to supporting me and giving me a better life. I am sorry I cannot be with you during the COVID shutdown. Also,

it's my privilege to thank my girlfriend Wei Huang for her constant encouragement and support. Your prayer for me was what sustained me this far.

Last but not least, I would like to acknowledge the University of Washington. The peaceful and diverse environment at UW help me develop myself with full comfort and freedom. "*Be Boundless*" -I am proud to be part of the UW community that I believe we together are going to change the whole world. Thanks again to all of the above who have helped me and let me enjoy the important 6 years in my life. I wish you all live deep and suck out all the morrow of life. Best wishes for your bright future.

DEDICATION

This thesis is dedicated to my grandparents.

For their endless love, patience, encouragement, and support. I am sorry I could not be with you for the last few years.

Chapter 1. INTRODUCTION

Electron, photon, and phonon are three main types of elementary particles[1], which carry not only energy and momentum but also additional information including spin and orbital angular momentum[2]. In the solid-state system, these three particles usually coexist, under certain conditions, their interactions of them can be observed. Take the semiconductor as an example, the incident photon transfers its energy to the electron and excites the ground-state electron to a higher energy state which is known as band transitions[3]. Reversely, the electron at the excited state will relax to the ground state with the emitted photon. Meanwhile, the energy of an electron can also transfer to the phonon of the crystal lattice through the non-radiative process. While in the piezoelectric materials, the RF photon can efficiently couple to the phonon mode and excite the surface acoustic wave along the surface of the piezoelectric substrate[4]. Also, the generated phonon mode can change the local refractive index and shape of the photonic system which achieves the dynamic modulation of the photonic system known as the Brillouin scattering[5]. More importantly, the coupling of those elementary particles can be much stronger inside the 2D semiconductors due to the strong vertical confinement[6]. As result, the optoelectronic properties of 2D materials can be effectively controlled by external electronic or mechanical approaches[7].

1.1 TWO-DIMENSIONAL MATERIAL OPTOELECTRONICS

Considering the monolayer and few-layer thickness of 2D material, the vertical confinement implies the stronger interaction between photon, phonon, and electron[8]. Taking the monolayer transition metal dichalcogenides (TMDC) as an example, the reduced dielectric environment contributes to a stronger excitonic response, the optical absorption and photoluminescence are 2 orders of magnitude larger than the direct band-to-band transitions[9]–[12]. Also, different 2D

materials have varied electronic bandgap from insulating Boron Nitride (BN) and semiconducting transition metal dichalcogenides (TMDC), black Phosphorus (bP) to semimetal materials such as graphene. These materials can cover a very broad electromagnetic spectrum range from microwaves to ultraviolet rays as shown in figure 1.1.

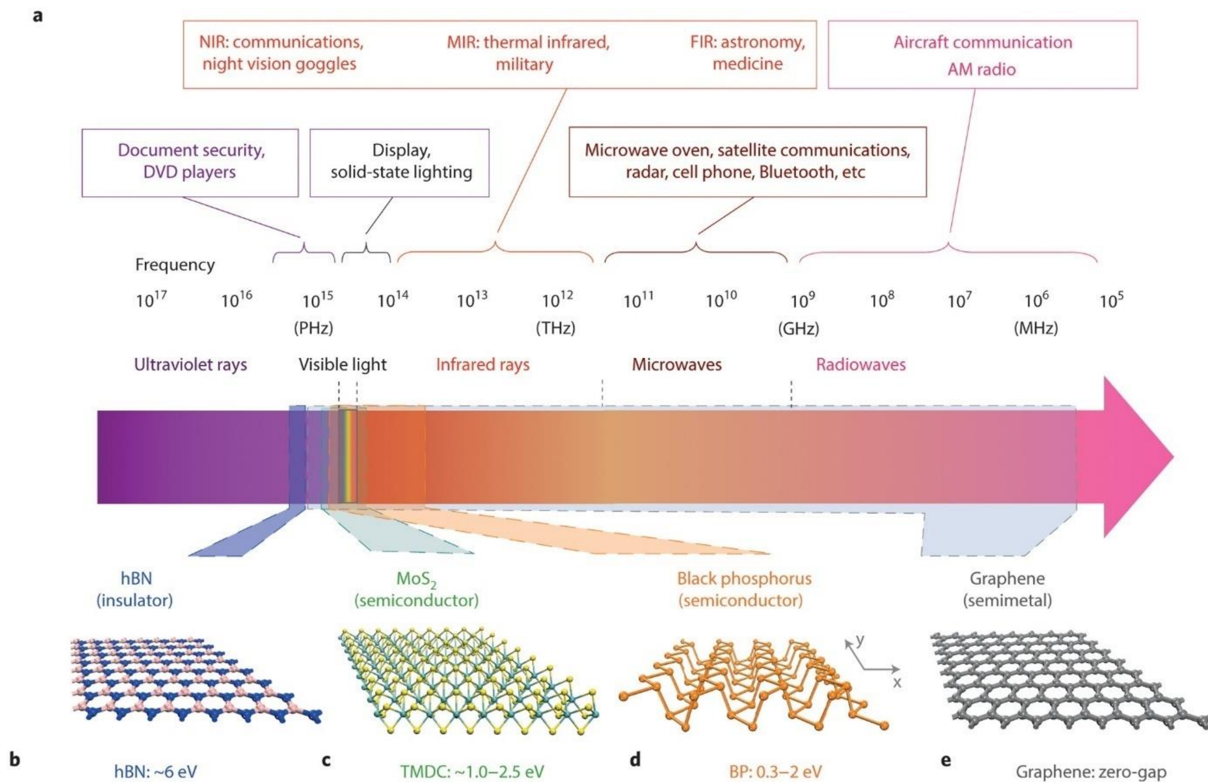

Figure 1.1. 2D materials covering a broad spectral range. Electromagnetic spectrum. Applications that utilize the different spectral ranges are presented in the top portion of the panel. NIR, MIR, and FIR indicate near-, mid-, and far-infrared, respectively. The atomic structures of hBN, MoS_2, bP, and graphene are shown in the bottom of the panel, left to right. The crystalline directions (x and y) of anisotropic bP are indicated.[8]

Despite the monolayer thickness, the monolayer TMDC exhibits strong photoluminescence[10], [13] and optical nonlinearity[14]. When integrated with photonic cavities, the exciton (bounded electron-hole pair) will be strongly coupled with photon, both the laser[15]–[17] and exciton-polariton[18]–[29] have been demonstrated in varied photonic platforms. While

black phosphorus has recently shown promising application in the mid-IR range[30]–[37], the electronic band structure could be effectively modulated by the external electric field which induces the change of the optical response[36]–[39]. Besides, 2D material can be easily transferred by van der Waals force without suffering the lattice mismatching[40]. This enables the integration of 2D materials with varied photonic and electronic platforms[30], [41]–[44] and makes it possible to construct vertical heterostructure devices[45].

1.2 BLACK PHOSPHORUS FOR INFRARED PHOTONICS

The schematic crystal structure of black Phosphorus (BP) is shown in figure 1.2 [35], the puckered structure indicates the anisotropic electronic band dispersion where the effective mass in the armchair direction is much smaller than the zigzag direction. As result, optical absorption and carrier mobility in the armchair direction is much larger than the zigzag direction as proved by several groups. Particularly, the band structure of BP has a direct band gap and strong layer dependence, the electronic bandgap will reduce from 1.8 eV to 0.33 eV as we increase the BP thickness which makes it the candidate material for the mid-IR range[46]. When alloy with Arsenide, the bandgap can be further reduced to the 0.1 eV which corresponds to the far-IR range[32]. The layer dependence behavior is attributed to the strong interlayer coupling which could be influenced by the perpendicular electric field[39].

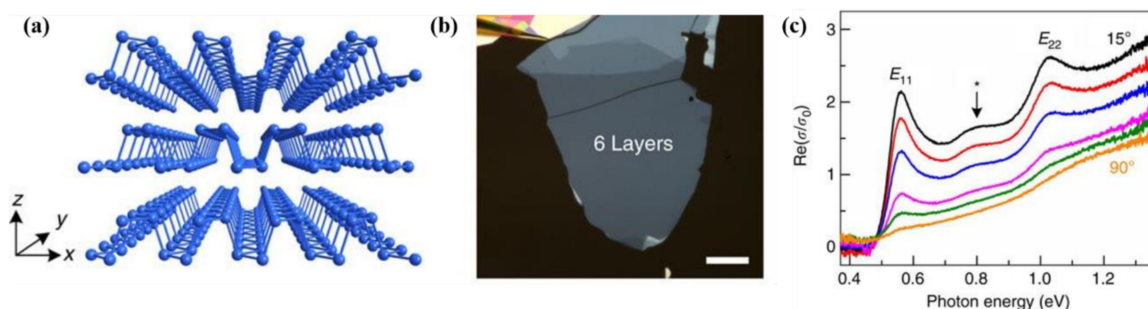

Figure 1.2. Optical properties of few-layer black Phosphorus. (a) The lattice structure of few-layer BP, showing the puckered hexagonal crystal with two nonequivalent directions: AC (x-direction) and ZZ (y-direction). (b) Optical image of a representative 6L sample. Scale bar, 20 μm. (c) The real part of the optical conductivity σ for the 6L sample in b, in the unit of the universal optical conductivity $\sigma_0=\pi e^2/2\,h$, with polarization angles of incident light from 15° to 90°, in steps of 15°. The marks E11 and E22 denote the first and second subband transitions, asterisks (*) denote hybrid transitions.[35]

Although the optical response such as photocurrent has long been studied[43], [47]–[53], the way to modulate the optical property is not fully understood yet. In this thesis, we demonstrated the optical modulation of few-layer BP and proposed the possible device schematic for the commercial optical modulator application.[33]

1.3 TRANSITION-METAL DICHALCOGENIDES FOR EXCITONIC DEVICES

As discussed before, the TMDC has unique electronic and optical properties[10]. The lack of inversion symmetry and strong spin-orbit interaction induce the breaking of the valley degeneracy[11], [54]–[58]. Each valley exciton will be locked with the electron spin and can only interact with certain helicity of the light when considering the angular momentum conservation as shown in figure 1.3. Also, it has strong and stable exciton resonance due to the vertical confinement. For MoS_2, the binding energy exceeds 300 meV which implies the room temperature application[59]. Within this confined system, it also exhibits strong many-body interactions as increasing the carrier densities. The more complex particles such as trion and biexciton are also predicted and measured[60]. When interacting with the photonic cavities, the confined photonic mode contributes to the stronger interaction with the excitonic resonance.

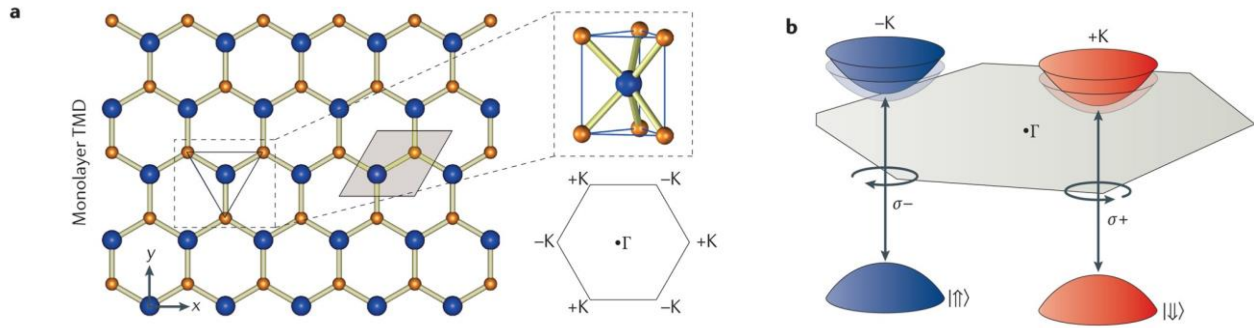

Figure 1.3. Valley-dependent carrier transport. a) The 2D hexagonal crystal structure of a monolayer transition metal dichalcogenide (TMDC) composed of transition metal atoms (blue) and chalcogen atoms (orange) resembles that of graphene but with broken inversion symmetry. A side view shows the 3D structure. The hexagonal Brillouin zone is shown labeling the Γ point and the two inequivalent +K and −K points. b) Valley-dependent optical selection rules for interband transitions in monolayer TMDCs. σ+ polarized light couples to the +K (red) valley, and σ− polarized light couples to the −K (blue) valley.[56]

However, the application of exciton in TMDC also encounters a few problems[12]. The main difficulty is that the transport of exciton is hard to control. Unlike free electrons which can be driven by the applied electric field, the exciton is a neutral particle formed by the bound electron-hole pair and will only be dissociated by the applied field[61]. Although, some prototype of the excitonic transistor based on interlayer exciton of TMDC heterostructure has been proposed and demonstrated[57], [62]. These devices require the diffusion of the exciton which needs large exciton density and is very inefficient. Besides, with the increase of exciton density, excitons prefer combining to be more complex particles such as trion, biexciton, or even ionized plasma which will impede the formation of the high-density exciton[60].

1.4 Electrical and strain modulation of the 2D materials

Electrical and strain modulation of 2D optoelectronic properties have been extensively studied in the past few years. The optical modulators based on different modulation mechanism has been

demonstrated in various 2D materials including graphene, TMDCs, and black Phosphorus[7]. The graphene, as the first discovered 2D material, has been utilized for an electro-optical modulator that broad optical bandwidth and fast operation speed up to 30 GHz have been achieved[63]–[66]. More recently, the majority of studies have been focused on the 2D semiconductors[48], [67]–[69] including the TMDCs and bP which show improved device performance compared to graphene and also strong resonant enhanced behaviors near the optical transition resonances.

The electrical conductance of bP-FET (field-effect transistor) can be modulated by the gate voltage with large on-off ratios [69]–[72]. With high k materials such as the AlOx, the modulation of the carrier concentration is more than 10^{12} cm^{-2} that the material can reach the heavily doped region [72], [73]. As result, the bP device exists both bolometric effect with negative photocurrent and photovoltaic effect with positive photocurrent which are determined applied gate voltage [32], [43], [47]. In the heavily doped region, the bP performs like metal and optical heating will lead to strong carrier scattering and reduce the conductivity of the bP. When operated in the intrinsic region, the optical excitation will contribute to the increase of free carriers and result in a positive photocurrent as shown in figure 1.4.

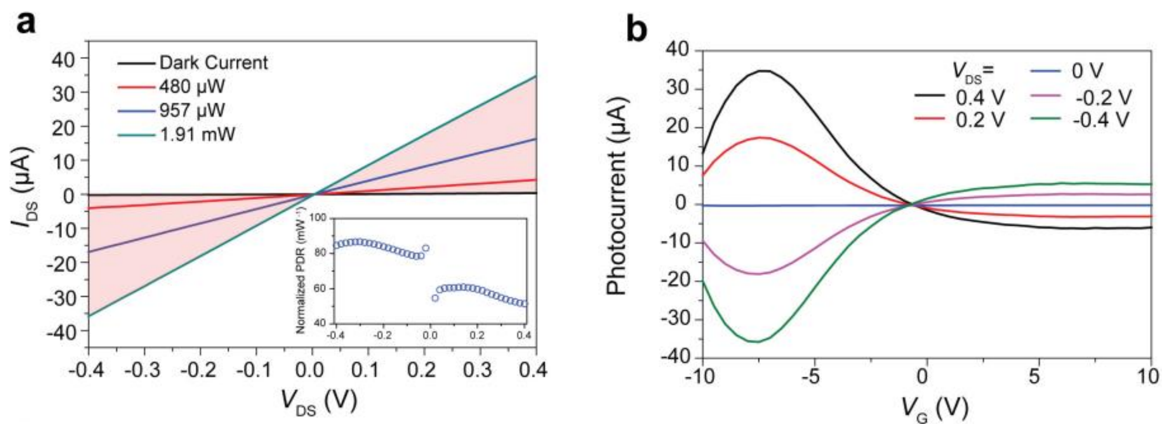

Figure 1.4. Gate and bias tuned photoresponse of the BP photodetector. a) Source-drain current versus bias voltage when optical signal is off (black line) and at various power levels (red: 480 μW; blue: 957 μW; green: 1.91 mW). b) Photocurrent versus gate voltage at various fixed bias

voltages. The direction of the photocurrent changes as the gate voltage increases from negative values (where the BP has low doping) to positive values (where the BP is highly n-doped). The optical power in the waveguide is fixed at 1.91 mW.[43]

The strong modulation of the carrier concentration of bP also influences material absorption[39]. As the Fermi-level more into the conduction or valance bands, the incident photon needs to have enough energy to overcome the Fermi-level due to the Pauli-blocking effect which is also known as the Burstein-Moss shift. As shown in figure 1.5, the optical transitions near the optical bandgap are suppressed when the bP is heavily doped.

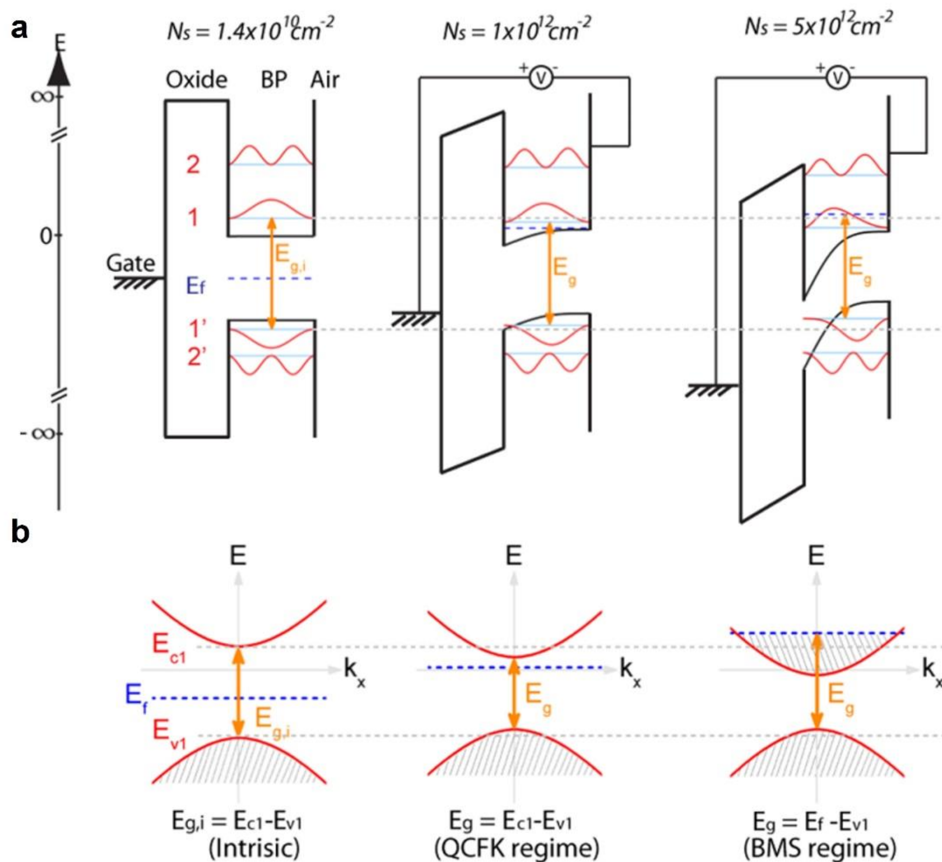

Figure 1.5. Work mechanisms of bP electro-optic modulation. a) Schematic, energy band diagram, and wave functions of 5 nm thick BP QW with Ns = 1.4×10^{10} (intrinsic regime), 1×10^{12} (QCFK regime), and 5×10^{12} cm^{-2} (BMS regime). Results are computed through self-consistent Schrö dinger-Poisson calculation. The energy zero is chosen to be at the bottom and center of the

conduction band. (c) Energy dispersion diagrams for the lowest/highest conduction/valence subband under doping conditions listed above. The level of carrier occupancy is indicated by the shaded region. The corresponding formula for calculating Eg is also listed.[39]

In addition to the doping effect, the back gate voltage also induces a large electric field across the bP flakes. The strong modulation of the band structure has been predicted by the tight-binding model and also experimentally confirmed by the ARPES (Angle-resolved photoemission spectroscopy)[38] and responsivity spectrum characterizations of bP[36]. The strong build-in electric field by surface doping can reduce the bandgap of the bP and even close the bandgap to form the semi-metal state. Also, according to the responsivity measurement, the photodetection range can be extended to 7 μm by applying the perpendicular electric field. The optical bandgap can be modulated from 0.35 eV to 0.18 eV. With the strong control of the optical bandgap, bP has been considered as the candidate material for the electro-optical modulator in the mid-IR regime. Besides the black Phosphorus, the TMDCs are also sensitive to electric field modulation[20], [28], [74]–[76]. Especially for the bilayer TMDCs, the electric field can break the inversion symmetry and contribute to the emergence of the valley effect or nonlinearity in the bilayer device[77], [78]. At the same time, the electric field will modulate the band structure and the energy of the exciton emission. As shown in figure 1.6, the bilayer WSe_2 has the indirect band transition contrary to the monolayer WSe_2[76]. As the electric field is applied, the layer degeneracy will be broken and the conduction band minimum and valance band maximum will shift in the opposite direction.

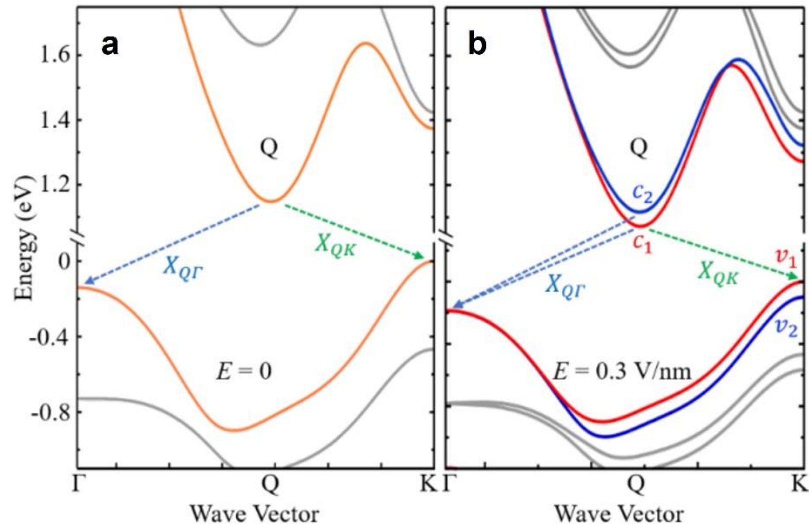

Figure 1.6. Calculated electronic band structure along the K-Γ line at zero (a) and 0.3 V/nm (b) vertical electric field.[76]

Considering the elastic properties of 2D materials, they can withstand the enormous strain that the band structure can be effectively modulated. As an example, the in-plane tensile strain efficiently weakens the interlayer coupling of bP [79], [80]. As shown in figure 1.7, the evolution of band structures in few-layer BP under in-plane biaxial strain has been systematically studied. The highly strain-sensitive nature of its bandgap contributes to variable-spectrum optoelectronics such as gas sensing. Continuous and reversible tuning of the operating wavelengths in light-emitting diodes and photodetectors based on bP flakes have been demonstrated that the multiple gases are detected solely using the bP as the light source [80].

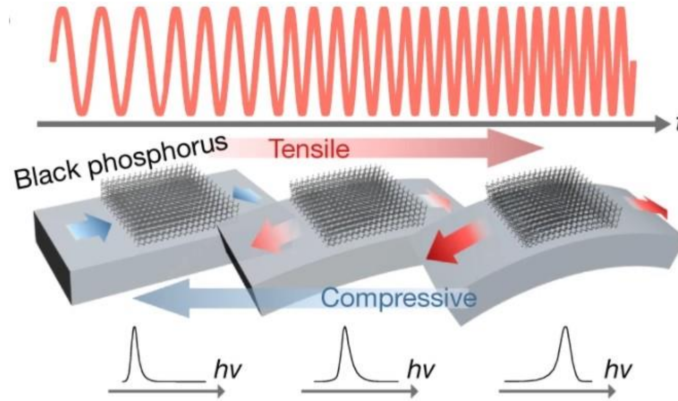

Figure 1.7. Schematic representation of the strain-induced actively tunable bandgap of bP. Compressive and tensile strains induce redshift and blueshift of the bP bandgap, respectively.[80]

Monolayer TMDCs are predicted to be strongly piezoelectric which has been closely studied for sensors, transducers, or piezo electronics[81]. A power density of 2 mW m^{-2} and a 5.08% mechanical-to-electrical energy conversion efficiency have been demonstrated in monolayer MoS_2. The strain can generate strong band structure tunning, while, it provides an excellent platform to control the photoluminescence, absorption, and band transitions[82]–[84]. With the tensile strain induced by the nanopillars, the exciton emission is highly localized and confined around the pillar region. By engineering the pillar shapes, a high yield of single-photon source has been achieved by the strain-induced quantum dots in the TMDCs[85]–[87]. The strain approach offers another degree of freedom to control the spatial energy profile for excitons that the deterministic creation of the single-photon emitters is achieved in the 2D systems.

1.5 Scope of this thesis

This dissertation consists of 5 chapters. It starts from the introduction of 2D optoelectronics in the first chapter. I discuss the coupling between the different physical degrees of freedoms including photon, phonon, electron where the interaction can be strongly enhanced in the 2D materials. The study of the physical phenomena in the 2D system contributes to the emergence of novel photonic

devices such as photodetectors and modulators. Besides that, I introduce a few unique optoelectronic properties of bP and TMDCs and discuss the physical origin of those properties. I also include the discussion of the electrical and mechanical modulation of the 2D materials in the first chapter that I aim to study the modulation of the 2D devices and propose for certain optoelectronic applications. In chap 2, I show the vertical electric field can control the interlayer coupling of bP and modulate the band structure of a few-layer device. As result, the transitions arise from the bP subbands where their energies can be modulated by the gate voltage. Based on the strong electro-optical modulation in chap 2, I consider the integration of bP with Silicon photonics device in chap 3. I start with the characterization and simulation of the bP flakes with the silicon waveguide structure. The modulation depth of the device is enhanced by the local photonic structures, and I show the potential of bP as the candidate materials for mid-IR photonics such as photodetectors and modulators. In chapter 4, I discuss the excitonic properties of the TMDC bilayer which can be controlled by the vertical electrical field. The spatial energy profile can be controlled to achieve excitonic applications. I consider the surface acoustic wave on the piezoelectric substrate which can generate a strong piezoelectric field. I show that the perpendicular field will couple to the interlayer exciton and achieve the periodic modulation of the exciton energy. As the acoustic wave propagates, the interlayer exciton is trapped at the local energy minimum and can transport together with the surface acoustic wave. In the last chapter, I summarize the dissertation work, provide insights for future improvement and also propose the application of those techniques to other material systems.

Chapter 2. ELECTRO-OPTIC MODULATION IN FEW-LAYER BLACK PHOSPHORUS

2.1 OPTOELECTRONIC PROPERTIES OF BLACK PHOSPHORUS

Among all the 2D materials, black phosphorus (bP) has the unique property that its bandgap varies with the number of layers over a very wide range, from around 0.3 eV in the bulk to approximately 1.5-2.0 eV in monolayers (the corresponding optical wavelength range is 0.62-4.3 μm) [31], [88], [89]. In addition, the hole mobility in bP is as high as 10^4 $cm^2/V\cdot s$ [69]and the effective mass of electrons and holes are small along the armchair crystal direction[90]. All of these make bP a very promising material for broadband, hyperspectral optoelectronic applications[8], [71].

2.1.1 *Anisotropic optoelectronic properties of black Phosphorus*

Black Phosphorus is rediscovered as an elementary layered material that each phosphorus atom is connected to three adjacent atoms to form the orthorhombic crystal structure[88], [91]. Considering the monolayer bP, it has a rectangular unit cell that the lattice constants along armchair and zigzag directions are 4.58 Å and 3.32 Å[69]. Due to this reduced in-plane crystal symmetry, the band dispersion of thin layer bP along armchair and zigzag directions will be different. The effective mass for electron and hole along the armchair direction is much smaller than the zigzag direction. As result, the physical properties including mobility, optical absorption, and photoluminescence show strong anisotropy along different crystal axis which has previously been studied by many groups. As shown in figure 2.1, the angular-dependent DC conductance is measured by patterning 6 pair electrodes along different directions which reveal the mobility

anisotropy for armchair and zigzag directions[90]. The optical extinction and photoluminescence are also characterized with strong anisotropy as we change the linear polarization of the incident light[92]. Larger optical absorption is expected along the armchair direction than the zigzag direction[35]. With the theoretical calculation, the mechanical property such as Young's modulus shows the similar angular dependent behaviors that zigzag direction is four times stiffer than armchair direction[93].

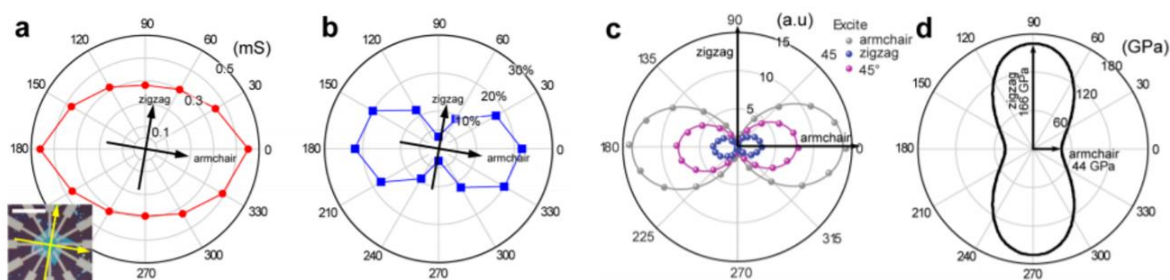

Figure 2.1. In-plane anisotropic properties of black phosphorus. (a) Angular dependence of the DC electrical conductance of a black phosphorus transistor. (b) Angular dependence of the relative optical extinction measured on the same flake displayed in (a). (c) Angular-dependent photoluminescence yield of a black phosphorus flake with laser excitation (λ = 532 nm) polarized along the zigzag direction, armchair direction, and a 45° direction. (d) Calculated angular dependence of the black phosphorus Young's modulus. The calculation predicts that the zigzag direction is about four times stiffer than the armchair direction.

Particularly, the anisotropic optical properties of bP contribute to the emergence of the polarization-dependent optical phenomena such as linear dichroism, polarization conversion, hyperbolic plasmon, and exciton-polariton. For few-layer bP, both transmission and reflection spectrum can be characterized by the Fourier-Transform Infrared (FTIR) microscopy[35], [46], [90]. As result, the real and imaginary parts of the refractive index are estimated based on the measured spectrum that the strong linear dichroism has been confirmed for bP with varied thickness[51], [94]. As the photon energy approaches the transition resonances, the linear dichroism can be further enhanced with large contrast for armchair and zigzag directions[35].

When integrating with the optical cavity, the reflected beam for different polarization will have a large phase difference[95], [96]. The polarization conversion can then be realized with tri-layer bP and performed as the tunable wave plates. Considering the strong tunability of the transition resonance under perpendicular electric field, the phase modulation of bP devices can be effectively controlled that phase retarder has been demonstrated[95]. The strong anisotropy also suggests the natural hyperbolic property of bP, the formed plasmon and exciton-polariton will preserve the in-plane anisotropy and form the hyperbolic dispersion[97], [98]. As predicted in bilayer bP, the imaginary part of the optical conductivity for armchair direction and zigzag direction can have opposite signs starting at 2.8 eV which results in a hyperbolic region starting at this frequency[98]. For the clean sample coupled to the microcavity, the optical conductivity of bP near excitonic resonance is also polarization determined and dominated by the anisotropic excitonic effect. The signs for the imaginary part of the optical conductivity will also be opposite and contribute to the unique excitonic polariton with hyperbolic dispersion. All those interesting discoveries in bP offer the new possibility to manipulate the polariton propagation and control the optical response with atomic thin films.

2.1.2 *Layer dependent properties of black Phosphorus*

Another interesting property of bP is the strong layer-dependent band structure[33], [35], [46]. The monolayer bP has a large electronic bandgap with 1.8 eV[46]. The bandgap will gradually decrease when increasing the bP thickness and reach 0.3 eV for the bulk bP crystal as shown in figure 2.2 (a). Considering the vertical confinement, the sub-bands will arise from the black phosphorus denoted as Ec1, Ec2… for the conduction bands and Ev1, Ev2… for the valance bands. All these sub-bands show the strong layer dependence owing to the interlayer coupling in the black phosphorus, while the allowed transitions between the valance subbands and conduction subbands

are labeled by their band indices such as I, II …According to the first-principle calculations, the large interlayer coupling between adjacent bP layers are predicted that both conduction and valance band structures are susceptible to the bP thickness. As shown in figure 2.2 (b), the subbands start to shrink as we increase the layer number of bP. For practical applications, if we pursue the device for certain photon energy, the thickness of bP can be predicted that the optical transitions of bP can match the energy of the incident photon.

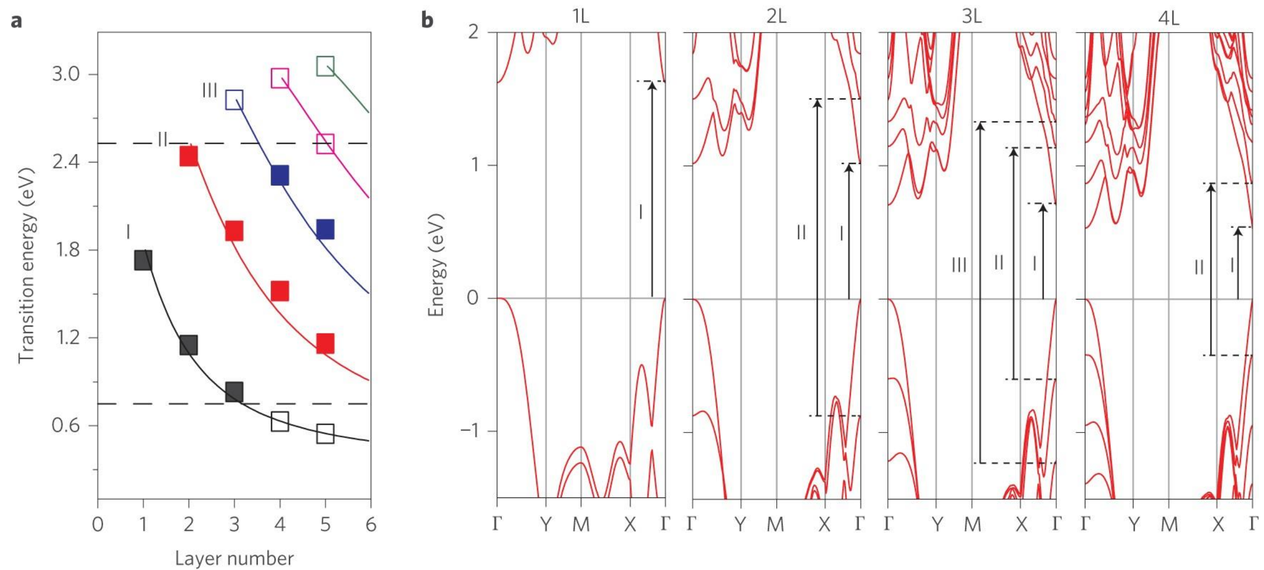

Figure 2.2. Layer-dependent band structure of black Phosphorus. (a) Observed optical resonance energy (solid squares) compared with the prediction (solid curves) by the phenomenological 1D tight-binding model. Empty squares are the interband optical transitions predicted by the tight-binding model that fall outside our measurement range. The lower and upper limits of our measurement range are marked by horizontal dashed lines. (b) Calculated GW quasiparticle band structure of monolayer, bilayer, trilayer, and tetralayer phosphorene (from left to right). Few-layer phosphorene is encapsulated between a sapphire substrate and an hBN capping layer in the calculation. As the number of phosphorene layers increases, the direct band gap at Γ decreases, and additional high energy subbands (marked by I, II, and III) emerge.[46]

More importantly, when adding the perpendicular field term to the Hamiltonian of the interlayer-coupled system, the corresponding energy for each transition will be modulated[39],

[99], [100]. The field can influence the interlayer coupling of the system, and cause the red shift of the transition energy also known as the quantum-confined Franz-Keldysh effect[39]. Meanwhile, by electro-static doping, the Fermi-level of bP can be shifted to the conduction or valance band and reach the so-called Pauli blocking regime. The energy below the Fermi level and related band will be forbidden, as result, the energy of the transition will have a blue shift. Both two effects are possible and important in the bP and make electro-optic modulation possible in this few-layer material. Under our field condition, we only resolve the modulation due to quantum confined Franz-Keldysh where the more detailed description and results are discussed in Chap 2.2.

2.1.3 *Optoelectronic devices based on few-layer black Phosphorus*

Indeed, many types of photodetectors based on black phosphorus have been demonstrated[43], [47]–[53], [101], operating in the visible and the near-IR bands. These photodetectors show high responsivity and low dark current—thanks to BP's bandgap, which is a significant advantage over graphene—and very high response speed[43], [52], [101]. Considering multilayer BP, its bandgap size around 0.3 eV makes it ideal for optoelectronic applications in the mid-IR range, which has many important applications such as spectroscopic chemical detection and free-space communication. It is highly desirable to realize mid-IR systems that are fully integrated, compact and portable for widespread applications. While mid-IR laser sources have become commercially available[102] and integrated photonic circuits have been developed on the ubiquitous silicon-on-insulator platform, mid-IR photodetection still relies on narrowband compound semiconductors such as InAsSb and HgCdTe[103], [104], which are difficult to be integrated with silicon. As an alternative, BP mid-IR photodetectors have already been demonstrated with promising performance. The 2D materials are easily integrated with silicon photonics by standard transfer technique. Both free-space and integrated photodetectors based on bP have been demonstrated

with high responsivity and speed[43], [47], [105]. Compared to the graphene detector[42], [106]–[109], the bP show significant improvement in its dark current that the detectivity of bP can be much better. For the speed of the device, the bP device can be operated exceeding 3 GHz owing to the high mobility of the bP[43]. When stacking with other 2D materials, the performance of bP detectors can be further improved. The bP-MoS2 heterostructure can form the type 2 band alignment with natural PN junction that the photoexcited charge carriers can be efficiently separated by the build-in field[110], [111]. Also, when operating in the reverse-bias regime, the leakage current will be suppressed by the PN junction. Due to the suppression of the dark noise, the high detectivity of 1.1×10^{10} cm $Hz^{1/2}$ W^{-1} at the mid-IR region has been demonstrated[111]. More recently, the bP-InSe heterostructure is fabricated with a clean interface and high material quality[112]. Considering the high mobility of bP and InSe thin film, the photoexcited carriers inside the vertical junction can be transported in the ballistic regime. For the reverse bias of the vertical junction, the ballistic avalanche phenomena have been observed that the on/off current ratio exceeds 10^4 and the average subthreshold slope is 0.25 mV dec^{-1}. As a result, the APD device can achieve the photon-detection with a limit of approximately 6,000 photons.

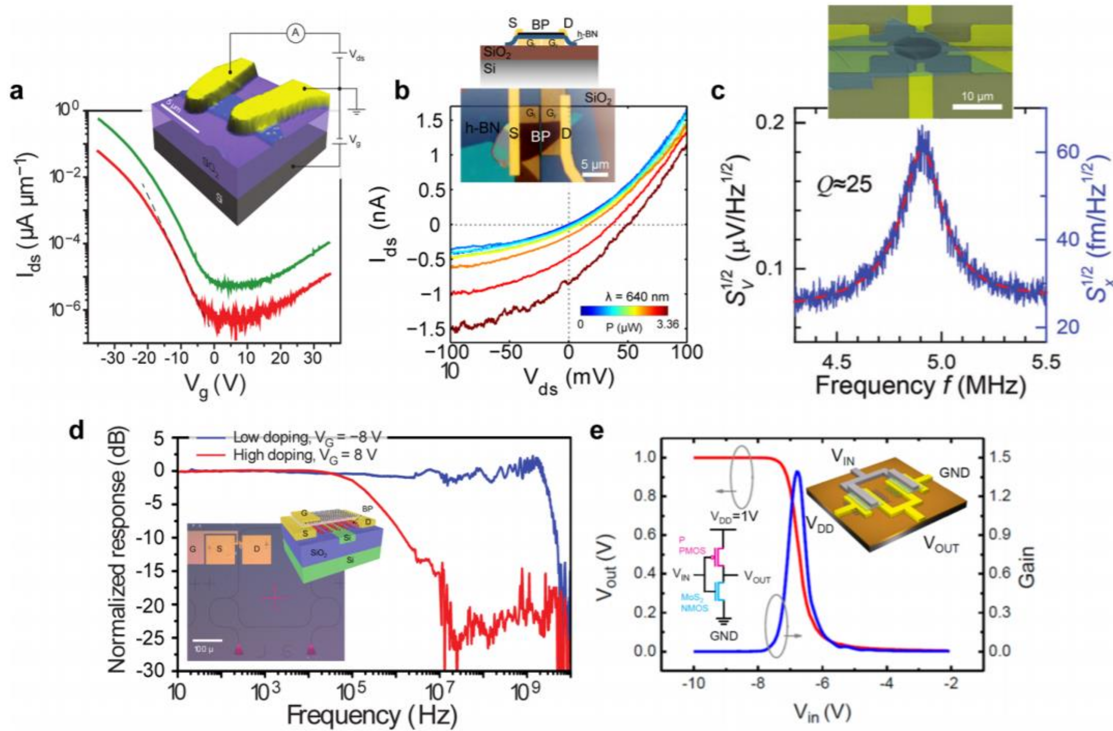

Figure 2.3. Black Phosphorus based nanodevices.[31] (a) Ambipolar field-effect transistor.[69] (b) Electrostatically gated PN junction displaying photovoltaic effect.[47] (c) Nanoelectromechanical resonator vibrating in the very-high frequency regime.[113] (d) High-frequency photodetector coupled to a silicon waveguide.[43] (e) Inverter amplifier based on MoS_2 and black phosphorus transistors, demonstrating the potential of black phosphorus for logic circuits.[114]

For the mid-IR optical modulator, multilayer BP is equally promising. Unlike the traditional materials which have very weak field response, strong field-effect tuning of its bandgap has been predicted in BP, and its infrared optical response at the mid-IR region has been measured[34], [39]. Its anisotropic band structure and interband coupling also imbued it with peak-like sub-band absorption features, which is advantageous for low voltage optical modulation. Although graphene has also been used for mid-infrared and terahertz modulation, metamaterial and metasurface structures are required to achieve sufficient efficiency[63]–[66], [109], [115], [116]. The graphene device mainly relies on the Pauli-blocking effect and change of the free carrier density that the modulation depth is quite limited. Also, the graphene suffers very strong free carrier absorption

and large dark current which also limits the potential application as the optical components. Contrary to the gapless band structure of graphene, the bP has a finite gap (> 0.3 eV) which suppresses both the free carrier absorption and dark current at room temperature (RT)[46], [69]. More importantly, the optical transitions of the bP can be engineered by its thickness from 1.8 eV to 0.3 eV that broadband application is promising. For 9 nm bP devices, the large electro-optical modulation at the mid-IR region is calculated[33], [39]. As result, bP devices offer a significant improvement on the detectivity as the photodetector and suppress the insertion loss as the modulator. All those properties make bP the candidate 2D materials for mid-infrared applications.

2.2 MECHANISMS FOR ELECTRO-OPTICAL MODULATION

2.2.1 *Franz-Keldysh effect in solid*

Bulk semiconductors exhibit the changes in the band transitions under the influence of the electric field, which is known as the Franz-Keldysh (FK) effect[117]. This effect is first observed in the CdS crystal, as the large field is applied, the optical absorption around the band edge will increase which indicates the decrease of the bandgap. Intuitively, the wavefunction of the electron and hole can tunnel into the gap region due to the large electric field, and induce the finite overlap between the electron and hole wavefunctions. With this effect, the corresponding energy to the absorption edge will have a red shift to the lower energy.

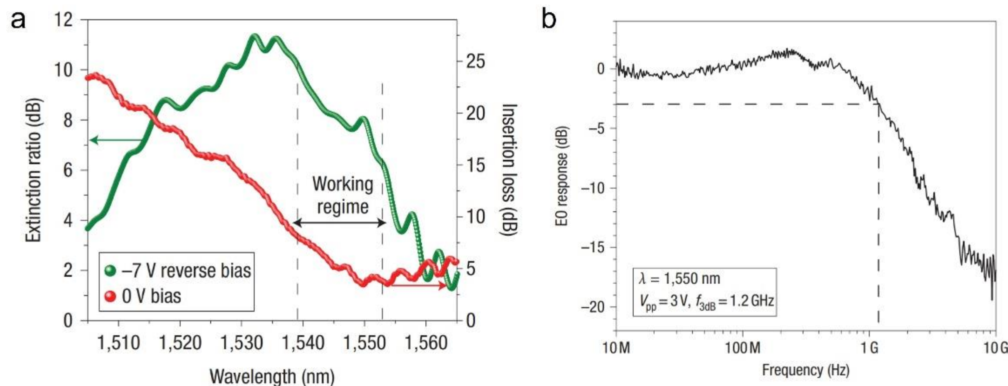

Figure 2.4. Performance of the GeSi EA modulator.[118] (a) Extinction ratio at –7 V bias and insertion loss at 0 V bias as a function of wavelength. The effective operating spectrum range is 1,539–1,553 nm. (b) Dynamic EO response of the device in the frequency range of 10 MHz to 10 GHz with a dynamic driving voltage (Vpp) of 3 V. No frequency roll-off is observed up to 0.7 GHz, indicating that the device can still achieve an 8-dB extinction ratio at 0.7 GHz with Vpp = 3 V. The 3-dB bandwidth is 1.2 GHz, and the corresponding extinction ratio is 4 dB.

The FK effect is nowadays widely used in the electro-absorptive modulator that GeSi, GeSn, and InGaAs are integrated with Si devices[119]–[121]. With the strained Ge-on-Si nanostructures, an enhancement on the FK effect has been observed which is ideal for telecommunication[118]. As shown in figure 2.4, the designed waveguide-integrated devices have achieved 10 dB modulation depth with a small active device area. Also, the ultralow energy cost and GHz modulation speed are realized when operating as the optical modulator.

2.2.2 *Quantum-confined Franz-Keldysh effect in black Phosphorus*

More interesting, this field modulation can be more significant in the 2D system. Considering the vertical confinement of the black Phosphorus, it will form the vertical quantum well and induce the discrete energy level denoted as Ec_1, Ec_2… and Ev_1, Ev_2…[33], [33], [37], [39]Additionally, the strong layer-dependent property of black Phosphorus suggests the possible gate modulation of the bP band structure. From the theoretical calculation, the bandgap of the bP will decrease as we increase the electric field. Will this effect, it has been demonstrated that a large build-in field induced by layers of K atoms can close the bandgap and form the anisotropic semimetal state where bP shows linear dispersion in armchair direction and quadratic dispersion in the zigzag direction. According to the first principle calculation, the conduction band and valance band will touch at the filed 4.5 V/nm. After the transition field, the topological phase could be obtained where the band inversion will occur. Unfortunately, our device is operated in the weak field

regime, the field is still far away from the transition electric field. Within this range, the electric field can be considered as the perturbation of the system and simply cause the red shift of the absorption edge.

In addition to the red shift of the absorption edge, the discrete energy level due to the vertical confinement will also contribute to the effect of the field modulation. Considering the flat band condition, the split energy level such as Ec_1, Ec_2… and Ev_1, Ev_2… can only be accessed with the same band indices due to the symmetry of the wavefunctions. Take the Ec_1 and Ev_2 as the example, the transition between these two levels is forbidden because the wavefunction of them are orthogonal with each other which the total integral of the wavefunction overlap will be 0 while the wavefunction of energy levels with the same band indices will have finite overlaps such as Ec_1 and Ev_1. However, the overlap between wavefunctions of different energy levels will change as the perpendicular field is applied. As result, it will cause the change of the optical absorption in few-layer BP and contribute to the electro-optic modulation in our devices. Considering the initial P-doped BP, the material has initial band bending due to the build-in field of the flake as shown in figure 2.5.

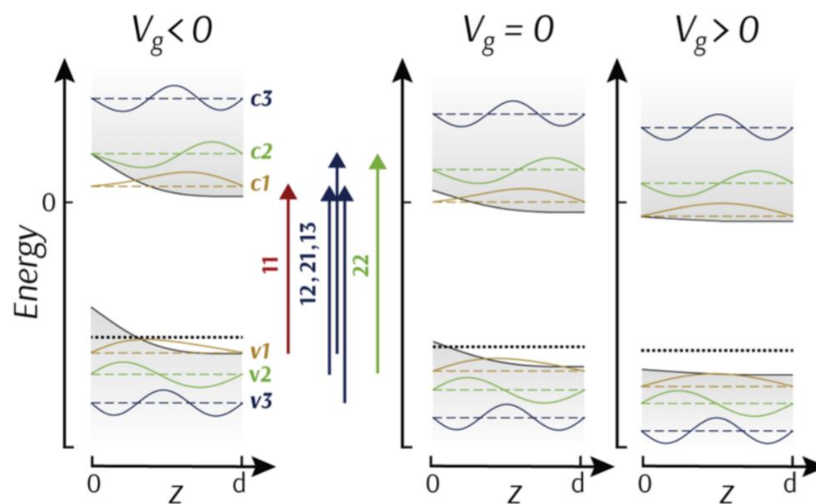

Figure 2.5. Schematic energy band diagram of BP three sample biases, Vg < 0, Vg = 0, and Vg > 0. The dashed lines in panel d mark the energies of each sub-band. The solid lines depict the wave function in each sub-band. The black dotted line marks the Fermi level. The red/blue/green vertical arrows in panel d show possible transitions that may contribute to the modulation level extrema observed.

2.3 DEVICE FABRICATION AND MEASUREMENT SCHEMATICS

To measure this electro-optic modulation in BP, we exfoliated multilayer BP flakes from bulk crystal and used the dry transfer method to transfer them onto a lightly doped silicon substrate with a layer of thermally grown silicon dioxide. To maximize the field at BP/SiO2 interface for optimal mid-IR absorption in BP, we set the SiO2 thickness to be 450 nm based on the calculation of the transfer matrix method. Titanium/gold top electrodes were patterned and deposited immediately after the transfer. Finally, 10 nm of alumina was deposited with atomic layer deposition (ALD) to encapsulate the BP layer and protect it from degradation. A schematic illustration of the device and measurement setup is depicted in Figure 2.6 (a). The optical image of a representative device is shown in Figure 2.6 (b). The thickness of the BP flake in Figure 2.6 (b) is determined to be 9 nm with atomic force microscopy (AFM), which corresponds to 17 monolayers.

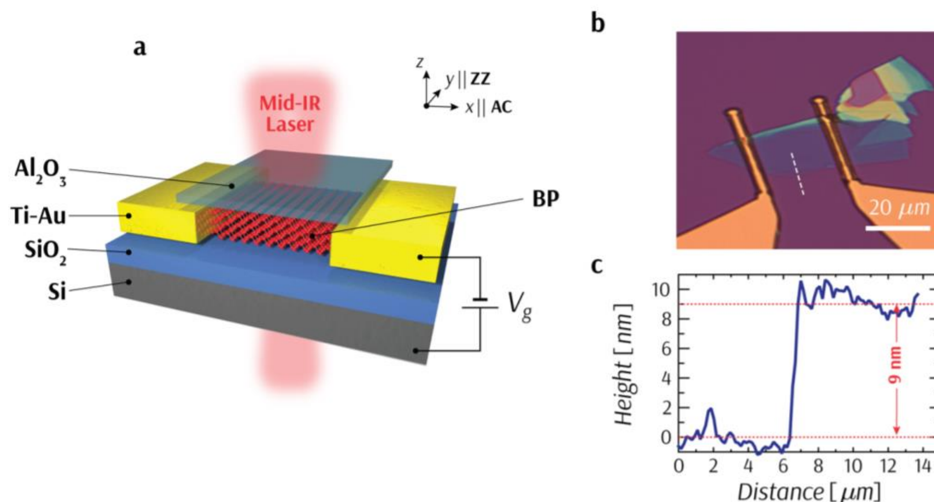

Figure 2.6. Black phosphorus electro-optic modulator. (a) Schematic illustration of the BP modulator, featuring the normally incident mid-IR laser beam and the lightly p-doped silicon substrate as the back gate. The BP flake is oriented with the arm-chair (AC) crystalline axis along the x-axis and the zigzag (ZZ) crystalline axis along the y-axis. (b) Optical microscope image of the BP modulator. (c) Height profile (along the dashed line in b) obtained with atomic force microscope shows that the BP thickness is about 9 nm which corresponds to 17 layers.

The measurement setup used in this study is schematically shown in Figure 2.7. An optical parametric oscillator (Firefly-IR, M Squared) with a tunable output wavelength range from 2.5 to 3.7 um is used in the measurement. The output mid-infrared light is split into a signal beam and a reference beam. Signal and reference beams are chopped by the inner and the outer part of the chopper which has different duty cycles. Therefore, the two beams are chopped at different frequencies to be differentiated. The signal beam is focused on the sample by a 15x objective to a spot of 20 μm in diameter which is smaller than the sample size. The transmission light of the signal beam is collected by the CaF_2 lenses and focused on an InAsSb photodetector (PD). The photodetector current is measured by a lock-in amplifier and the transmitted optical power is calculated. For the reference beam, the power is measured by the same photodetector connected to another lock-in amplifier locked to a different chopper frequency from that of the signal beam. In addition, a density filter in the path of the reference beam is used to balance the power of the signal beam and the reference beam. The relative transmission of the signal beam power is thus calculated by normalizing it to the reference beam power. In this way, the temporal fluctuation of the laser power and its variation during the wavelength scan is canceled out. By using this setup and averaging the measurement data, the accuracy of the measurement of the transmission can be better than 10^{-3}.

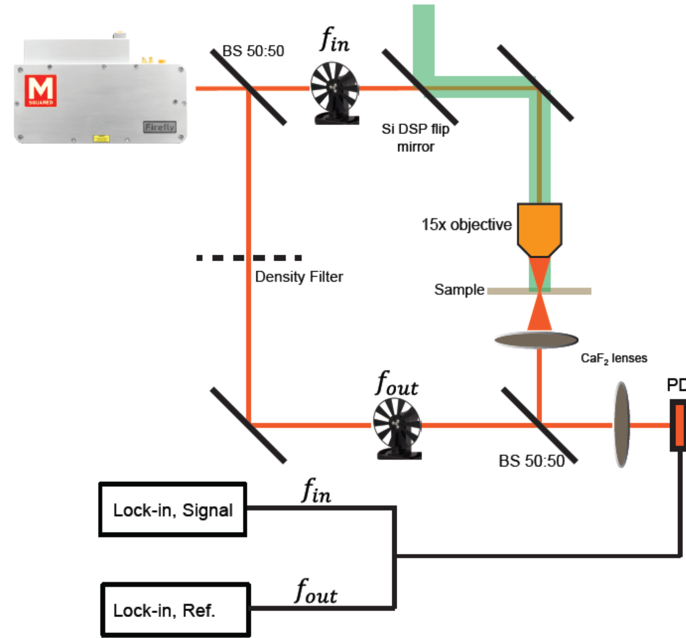

Figure 2.7. Schematics of the mid-infrared BP modulation measurement setup. The incident light is divided into two paths which are locked with different frequencies by the chopper.

To measure the electro-optic response, we used the Si substrate as the bottom gate while the top electrodes on the BP are grounded. Because silicon has low absorption in the mid-IR range and the substrate is double-side polished, transmission loss due to absorption by the substrate is negligibly small.

2.4 ELECTRO-OPTIC MODULATION IN FEW-LAYER BLACK PHOSPHORUS

Figure 2.8 (a) shows the measured extinction coefficient, defined as $1 - T(V_g)/T_0$, where T and T_0 denote the powers transmitted through the substrate with and without BP, respectively. The results are shown for three cases of $V_g = 0, \pm 150$ V applied to the back gate, the device is under normal illumination, and the incident light is linearly polarized along the armchair (AC) crystalline axis of BP. While the overall transmission shows non-monotonic energy dependence due to the interference effect in the multilayers of the device, one can observe the gate-induced modulation.

To reveal the electrostatic control of the transmission, we define the modulation level $[T(V_g) - T(0)]/T(0) = \Delta T/T(0)$, which is computed from the data in Figure 2.8 (a) and plotted in Figure 2.8 (b). $T(0)$ is the transmission when V_g=0 V, which is repeatedly measured and used as the reference point throughout the experiment. In this way, the absorption by the substrate and fluctuation of laser power is nulled out. The result shows a clear dependence on the photon energy with (positive and negative) peaks at 0.38 and 0.43 eV, respectively, where modulation level up to 3% is achieved when the gate voltage is switched between ±150 V. Because BP is linearly dichroic due to its anisotropic optical absorption, we also performed similar measurement with light polarization aligned with the zigzag (ZZ) axis. The result displayed as the dashed line in Figure 2.8 (b), shows a much weaker modulation level, as expected from theory. The 2D plot in Figure 2.8 (c) shows systematic measurement results of the modulation level when both photon energy and gate voltage V_g are continuously scanned, which revealed several features worth noting. First, $\Delta T/T(0)$ remains nearly zero, except in the close vicinity of two characteristic photon energies, E_a =0.38 eV and E_b =0.43 eV, where strong modulation can be observed. Second, the sign of $\Delta T/T(0)$ also shows dependence on the polarity of V_g. As V_g changes from negative to positive, at E_a, $\Delta T/T(0)$ changes from positive to negative, while at E_b, the modulation level experience a negative-to-positive sign flip. In addition, one can also spot in Figure 2.8 (c) a third characteristic energy with a relatively weak modulation in close proximity of E_c=0.5 eV, where the sign change with gate bias is similar to that observed at E_a. Finally, E_a shifts to the lower value with increasing $|V_g|$, whereas E_b shifts toward the higher value at the same time.

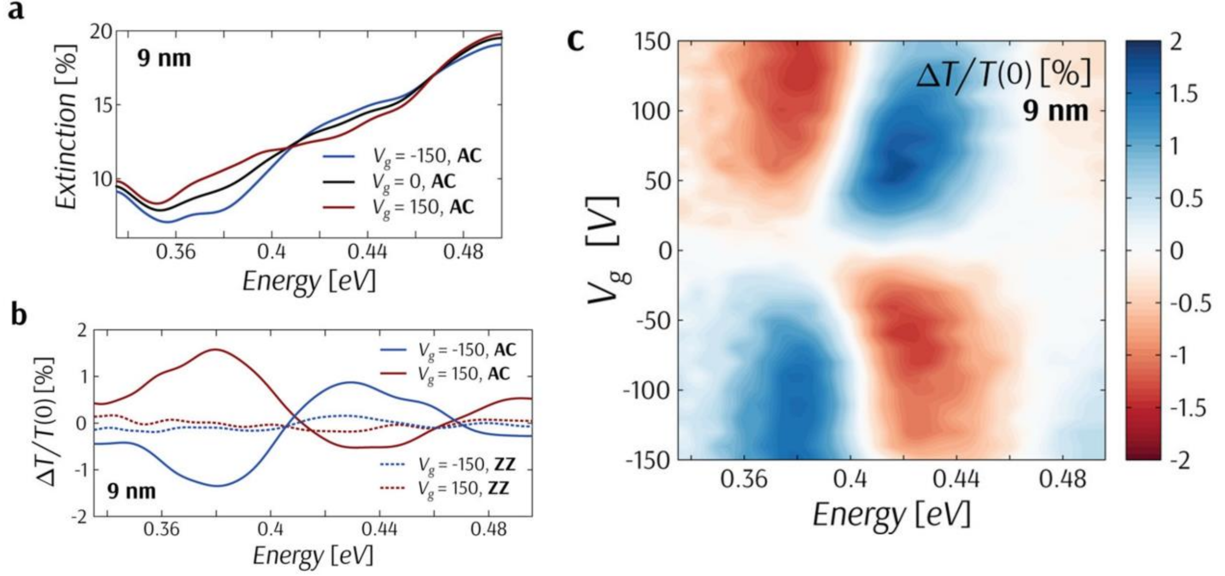

Figure 2.8. Measurement of mid-IR electro-optic modulation in BP. (a) Measured extinction of the transmitted light for 9 nm BP device at three values of gate voltages Vg = 0, ± 150 V. The incident light is linearly polarized with the electric field parallel to the AC crystalline axis. (b) The modulation level ΔT/T(0) for 9 nm thick BP at Vg = ±150 V for light polarization along AC (solid lines) and ZZ (dashed lines) crystalline axes. A maximal modulation of about 3% is obtained at a photon energy of 0.38 eV. (c) The modulation level measured as functions of energy and gate bias for 9 nm thick BP. Three characteristic peaks can be observed at Ea = 0.38 eV, Eb = 0.43 eV, and Ec = 0.5 eV.

To gain a qualitative understanding of the results, we argue that the characteristic energies ($E_{a,b,c}$) in figure 2.8 (c), where the modulation extrema take place, nearly coincide with the transition energies, E_{ij}, between the *i*-th conduction subband (c*i*) and *j*-th valence subband (v*j*). To verify, we compare the experimental values with those obtained with quasi-1D tight-binding model:

$$E_{ij} = \Delta_0 - 2(\gamma_c - \gamma_v) + \frac{\pi^2(\gamma_c i^2 - \gamma_v j^2)}{(N+1)^2} \tag{2.1}$$

where, Δ_0 is the monolayer bandgap and N is the number of layers. γ_c and γ_v denote nearest neighbor interlayer coupling for the conduction and valance bands, respectively. We emphasize that expression (1) is valid for flat-band conditions only. Although the latter is not the case in our

measurements (to be discussed later), Eq. (1) can still be used to gain an intuition of the characteristic energies' origin. Using the values of the parameters given in Reference, the transition energies in the energy range of interest for 9 nm BP can be estimated as E_{11}=0.39, E_{12}=0.41, E_{21}=0.43, E_{13}=0.44, and E_{22}=0.47 eV. The comparison suggests that the first and third modulation exterma in Figure 2.8 (c) are related to same-index transition energies E_{11} and E_{22}, respectively. The second characteristic energy in figure 2.8 (c), however, seems to originate from hybrid transitions, i.e., between sub-bands with $i \neq j$, though the weighted contribution of each hybrid transition is not clear.

We next examine the sign variation in $\Delta T/T(0)$ and its dependence on bias polarity. Hall measurement on the sample has shown that the BP is intrinsically p-doped with a hole concentration of ρ_h=5.5×10^{11} cm^{-2} at zero V_g. Because of the relatively thick oxide layer of the substrate, V_g applied to the back gate is insufficient to tune the BP to the n-doped regime, though the hole concentration ρ_h decreases as V_g changes from negative to positive. For 11 transition, as V_g becomes more negative, band bending makes the electron and hole wavefunctions more localized toward the opposite sides of the BP, thereby reducing the conduction-valance overlap and its corresponding oscillator strength. This leads to a decrease in the absorption at the corresponding photon energy and renders the transmission at negative V_g to be larger than $T(0)$, hence the positive $\Delta T/T(0)$ signs. Conversely, the transmission at positive V_g is lower than $T(0)$ thus the negative $\Delta T/T(0)$ sign. For 12 transition, however, the wavefunction overlap increases with the hole concentration. The latter renders a reverse V_g dependence for 12 relative to 11 and therefore, justifies the opposite signs in $\Delta T/T(0)$ at E_a and E_b of figure 2.8 (c). Similar behavior can also be anticipated for 21, or 13. We emphasize that the observed sign change of the modulation level at E_b due to the hybrid transitions in figure 2.8 (c) suggests that the BP cannot be

in the flat-band condition when V_g is zero because the hybrid transitions are forbidden under the flat-band condition. Instead, the trapped charges at the BP/SiO_2 interface may cause the intrinsic doping to be distributed non-uniformly among the sample layers and cause band bending.

2.5 NUMERICAL ANALYSIS FOR FEW-LAYER BLACK PHOSPHORUS

To describe the electronic energy spectrum, we use a combination of two Hamiltonians: a tight-binding model in the out-of-plane direction and a two-band $k \cdot p$ model for the in-plane. The full Hamiltonian reads as,

$$H = H_M \otimes I_{N\times N} + H_z \quad (2.2)$$

where N is the number of layers. H_M describes the low-energy electronic structure of monolayer BP around the Γ point,

$$\mathscr{H}_{\parallel} = \begin{pmatrix} \eta^c k_x^2 + \nu^c k_y^2 & \gamma k_x \\ \gamma k_x & -\eta^v k_x^2 - \nu^v k_y^2 \end{pmatrix} \quad (2.3)$$

The parameters $\eta^{c/v}$ and $\nu^{c/v}$ are related to in-plane effective masses of monolayer BP, via: $\eta^{c/v} = \hbar^2/2m_x^{c/v} \mp \gamma^2/\Delta$ and $\nu^{c/v} = \hbar^2/2m_y^{c/v}$. Δ=2.12 eV is the monolayer bandgap and $\gamma = 2.8\ eV \cdot Å$ denotes intralayer conduction-valence coupling. In-plane effective masses are assumed to be $m_x^c = m_x^v = 0.15\ m_0$, $m_y^c = 0.7\ m_0$, and $m_y^v = 1.0\ m_0$, where m_0 is the free electron mass.

H_z describes the interlayer coupling and is given by,

$$H_z = \begin{pmatrix} H^c & 0 \\ 0 & H^v \end{pmatrix} \quad (2.4)$$

where each diagonal block, $\mathscr{H}^s$ with $s \to c/v$ for conduction/valence bands, is similar to the Hamiltonian of a linear atomic chain:

$$\mathscr{H}^{s} = \begin{pmatrix} \varepsilon^{s} + \mathcal{U}_1 & \gamma^{s} & 0 & 0 \\ \gamma^{s} & \varepsilon^{s} + \mathcal{U}_2 & \ddots & 0 \\ 0 & \ddots & \ddots & \gamma^{s} \\ 0 & 0 & \gamma^{s} & \varepsilon^{s} + \mathcal{U}_N \end{pmatrix} \tag{2.5}$$

Here, $\varepsilon^{c/v} = \pm\Delta/2$ is the conduction/valence band edge in monolayer BP. We use $\gamma^{c} - \gamma^{v} = 0.88$ eV as suggested in reference[46]. The absolute values are then chosen such that $\gamma^{c}/\gamma^{v} = -m_z^{v}/m_z^{c}$, where $m_z^{c/v}$ is the out-of-plane effective mass of bulk BP for the conduction/valance band. The latter ensures that both the tight-binding model and effective mass approximation yield similar descriptions of the energy spectrum in the bulk limit. From the values reported for $m_z^{c} = 0.2\, m_0$, and $m_z^{v} = 0.4\, m_0$, [2, 3], we have: $\gamma^{c} = 0.59$eV and $\gamma^{v} = -0.29$eV.

The on-site energies U_i in (S1.4) are related to the applied electrostatic potential $\varphi(z)$ through $U_i = -e\varphi(z)$, where e is the electronic charge and z_i is the vertical position of the i-th layer. The electrostatic potential is obtained via self-consistently solving Poisson's equation,

$$\frac{d^2\varphi(z)}{dz^2} = -\frac{e[\rho_h(z) - \rho_e(z)]}{\epsilon_{bP}\epsilon_0} \tag{2.6}$$

where $\epsilon_{bp} = 8.3$ is the out-of-plane dielectric constant of BP[122], ϵ_0 is the vacuum permittivity, and ρ_h (ρ_e) denotes hole (electron) carrier density (per unit volume). The latter can be calculated from the eigenenergies, $E_{sj\boldsymbol{k}}$, and eigenvectors, $\Psi_{sj\boldsymbol{k}}$, of H.

To speed up the self-consistent calculation, we use a simplified approach based on an approximate separation of the Schrodinger problem in the in-plane and out-of-plane directions. At each iteration of the self-consistent loop, the eigenvalue problem (independent of $\boldsymbol{k}$) associated with $\mathscr{H}^{s}$ is solved numerically to obtain the eigenvalues E_j^{s} and normalized eigenvectors (modes)ψ_j^{s}, with$j \in [1, N]$. We disregard the field-induced coupling between the conduction and valence modes with different indices, as a first-order approximation, so that the full Hamiltonian

in (eq 2.2) can be decoupled into a set of N independent Hamiltonians, one for each pair of conduction and valence modes:

$$\mathscr{H}_j = \begin{pmatrix} E_j^c + \eta^c k_x^2 + \nu^c k_y^2 & \gamma k_x \\ \gamma k_x & E_j^v - \eta^v k_x^2 - \nu^v k_y^2 \end{pmatrix}. \tag{2.7}$$

Near the subband edges, the dispersion corresponding to (eq 2.7) is parabolic, $E_{j\boldsymbol{k}}^c \approx E_j^c + \hbar^2 k_x^2/2m_x^{cj} + \hbar^2 k_y^2/2m_y^{vj}$, where $m_x^{cj} = \hbar^2/[2\gamma^2/(E_j^c - E_j^v) + 2\eta_c]$ and $m_y^{cj} = \hbar^2/2\nu^c$. The corresponding density of states is $\mathcal{D}_j^c = \sqrt{m_x^{cj} m_y^{cj}}/\pi\hbar^2$. To further simplify the problem, we calculate the carrier densities $\rho_{e/h}$ by approximating the eigenvectors as $\Psi_{sj\boldsymbol{k}} \approx \Psi_{sj\boldsymbol{0}}$, where $\Psi_{sj\boldsymbol{0}}$ can be reconstructed as,

$$\Psi_{cj\boldsymbol{0}} = \begin{pmatrix} \psi_j^c \\ 0 \end{pmatrix}, \Psi_{vj\boldsymbol{0}} = \begin{pmatrix} 0 \\ \psi_j^v \end{pmatrix}, \tag{2.8}$$

We get:

$$\rho_e(z_i) = \frac{1}{a_z} \sum_j \mathcal{D}_j^c \, k_B T \ln\left[1 + \exp\left(\frac{E_F - E_j^c}{k_B T}\right)\right] |\psi_j^c(z)|^2, \tag{2.9}$$

and similarly for the hole case, where E_F is the Fermi level, $a_z = 0.54$ nm the interlayer distance, k_B Boltzmann's constant, and T=300 K the temperature.

Once convergence is reached, the Hamiltonian in (eq 2.2) is numerically diagonalized to get exact eigenvalues $E_{sj\boldsymbol{k}}$ and eigenvectors $\Psi_{sj\boldsymbol{k}}$. The quantities, $E_{ij} = E_{ci\boldsymbol{0}} - E_{vj\boldsymbol{0}}$ and $\mathcal{S}_{ij} = \langle \Psi_{ci\boldsymbol{0}} | \Psi_{vj\boldsymbol{0}} \rangle$ are defined in the main text as transition energy and wave function overlap, respectively.

The optical conductivity along the *x*-axis (AC direction) pertaining to $ci - vj$ transition, is then computed with Kubo formula:

$$\sigma_{ij}(\omega) = \frac{\hbar e^2}{i(2\pi)^2} \int \boldsymbol{dk} \; \frac{\left(f(E_{cik}) - f(E_{vjk})\right) \left| \langle \Psi_{cik} | \hat{v}_x | \Psi_{vjk} \rangle \right|^2}{\left(E_{cik} - E_{vjk}\right)\left(E_{cik} - E_{vjk} + \hbar\omega + i\eta\right)}, \tag{2.10}$$

where $v_x = \hbar^{-1} \partial H / \partial k_x$ is the velocity operator along the x-axis and *f()* is the Fermi-Dirac distribution function. η is a phenomenological broadening term to account for finite damping. The x-axis relative permittivity can subsequently be calculated via: $\epsilon(\omega) = 1 + i\sigma/\epsilon_0 \omega t_{bp}$, where $\sigma = \sum \sigma_{i,j}$ and t_{bp} is the BP thickness. It is understood that contributions to σ, due to intraband transitions are negligible in the energy range of interest.

To verify the qualitative picture, we resort to these multi-physics numerical techniques to solve for the transmission spectra of the geometry shown in figure 2.6 (a). The refractive indices for Al_2O_3 (10 nm), SiO2 (450 nm), and Si are taken from reference[123]. The full account of the models employed is described in the supplemental material, and the results are summarized in figure 2.9. The calculated transition energy E_{ij} and wavefunction overlap S_{ij} at versus hole density ρ_h are illustrated in figure 2.9 (a). As shown, in the relevant range of ρ_h, only the transitions 11, 12, 21, 22, and 13 lie in the energy range of interest. Among those, 13 has near-zero overlap and therefore does not contribute to BP's absorption. For those transitions that contribute, the overlap decreases with ρ_h for 11 and 22 transitions, while it increases for 12 and 21 transitions. Furthermore, the transition energy E_{11} decreases with ρ_h, while the rest are almost not affected by it. The observed trends, namely, the reduction of the optical gap and the localization of the conduction and valance band wavefunctions along the opposite sides of the BP, are indeed consistent with the Franz-Keldysh effect in quantum wells under perpendicular static electric field.

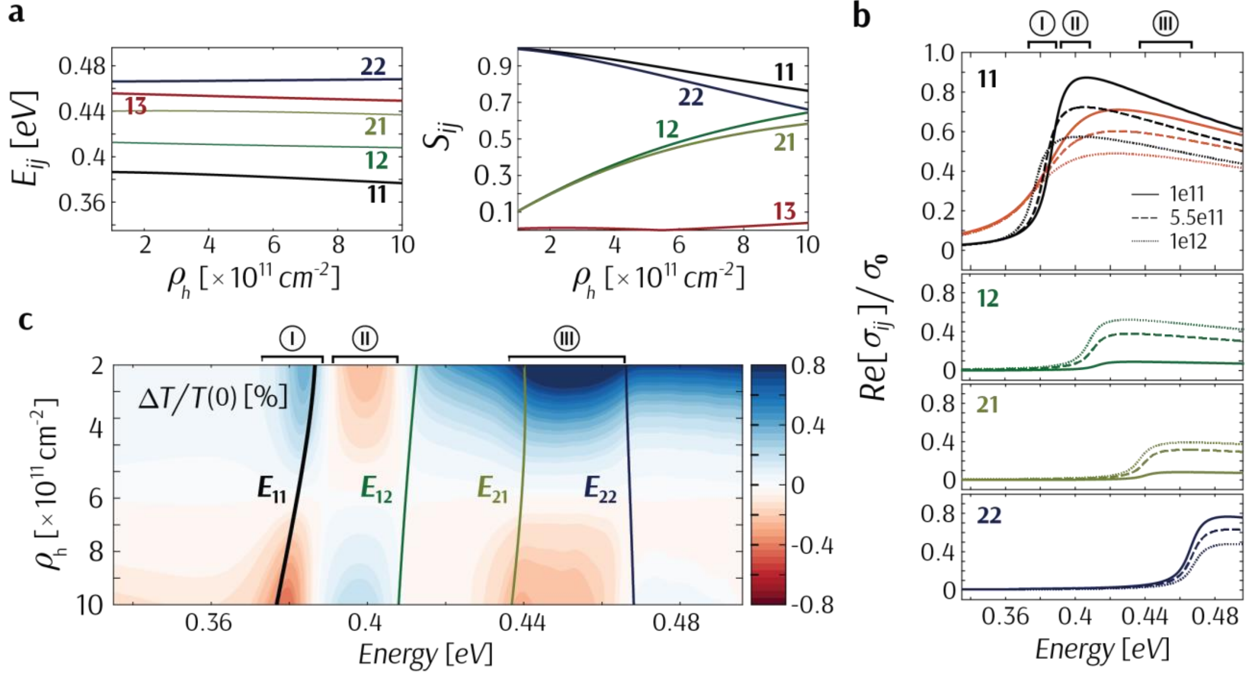

Figure 2.9. Theoretical calculation of electro-optic modulation for 9nm thick BP at room temperature. (a) The transition energy E_{ij} (left panel) and the wavefunction overlap S_{ij} (right panel) as a function of hole concentration ρ_h. (b) The real part of conductivity σ_{ij} (normalized to $\sigma_0=e^2/4\hbar$, the universal conductivity of graphene) for various transitions between ci and vj versus photon energy. (c) Contour plot of the modulation of the transmission as functions of energy and hole concentration. In (b) and (c), the broadening is $\eta = 6$ meV, except for the red lines in the top panel (b) where $\eta = 20$ meV.

The real part of the conductivity due to various subband transitions at three ρ_h values are shown in figure 2.9 (b). For the 11 transition, one can identify a red-shift in the absorption edge with increasing ρ_h, which is also observable for E_{11} in figure 2.9 (a). Furthermore, the consistent change in both conductivity peaks and overlap wavefunctions with ρ_h suggests a direct link between the two quantities. To compare with the experimental results, we calculate the modulation level $\Delta T/T(0)$ as a function of ρ_h and photon energy as shown in figure 2.9 (c), where $T(0)$ is the optical transmission when ρ_h=5.5×10^{11} cm^{-2}. From the figure, one can identify three energy intervals, specified as I, II, and II, where transmission modulation changes sign with ρ_h. Comparing

the results in figure 2.9 (b) and (c), it is evident that interval I and II are both related to 11 transition. More precisely, interval I originates from the shift in the absorption edge, while II is due to the change in wavefunction overlap. For interval III, however, all four transitions specified in figure 2.9 (b) contribute and the competition between 11 and 22 transitions on the one hand, and 12 and 21 on the other, determines how the modulation changes sign with ρ_h. Nonetheless, in general, a negative-to-positive sign flip in $\Delta T/T(0)$ with increasing ρ_h can mainly be attributed to same-index transitions. A positive-to-negative sign change of $\Delta T/T(0)$, however, has a more complex origin as it can be caused by both the energy shift of same-index transitions and the increase in wavefunction overlap of the hybrid transitions. The two mechanisms can be discriminated, however, via inspecting the energy separation of the immediate next sign flip. To elaborate, if the positive-to-negative sign change in $\Delta T/T(0)$ were due to the shift in E_{ii} transition, an opposite sign flip in modulation level should follow at immediate energies. This is due to the fact that for same-index transitions, the red shift in the absorption edge is always followed by a decrease in the wavefunction overlap (see e.g. the top panel in figure 2.9 (b)).

2.6 LAYER-DEPENDENT OPTICAL MODULATION OF FEW-LAYER BLACK PHOSPHORUS

As discussed before, the band structure of BP shows significant thickness dependence. The bandgap decreases from 1.8 eV for the monolayer to 0.3 eV for the bulk. We next focus on how bias-induced modulation of transmission spectra depends on BP thickness. We have fabricated several devices with BP flakes of different thicknesses and performed the same measurement as for the device with 9nm BP in the main text. In figure 2.11 of the main text, the positions in the energy of the modulation peaks were extracted from the 2D contour plots of the devices, as shown in figure 2.10. We extracted the modulation peaks at different gate voltages and interpolated them

to the zero gate voltage condition. Compared with the 9nm devices, more modulation peaks and features are observed in thicker devices, as expected from theory. Particularly in a 13 nm device (figure 2.10 (b)), more than 5% modulation in transmission was observed, which shows great potential for an integrated BP modulator operating in the mid-infrared.

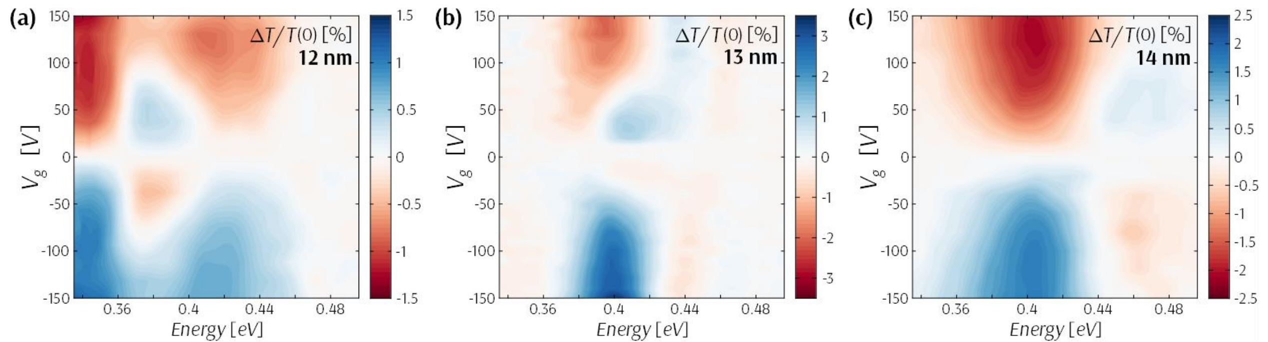

Figure 2.10. 2D modulation mapping of three other devices with different BP thicknesses. The max modulation of 5% has been observed in 13 nm bP flake. The modulation mapping results for bP flakes varied significantly with flake thickness.

In figure 2.11 (a), we report the same-index transition energies Eii extracted from the contour plots of modulation level by tracing the modulation extrema. As shown, E11 in a 9 nm thick device remains nearly unchanged with gate bias. For a different device with 12 nm thick BP, however, we observe E_{11} decreases monotonically for a positive-to-negative change of Vg, whereas E_{22} exhibits a maximum at Vg = 20 V. These observations are indeed consistent with the results obtained via our numerical calculation. In figure 2.11 (b), E_{11} shows a much stronger red shift with increasing ρh in thicker BP than in thinner BP. For E_{22}, it develops a maximum with ρh as the number of layers increases. We should mention that, for hybrid transitions, it is not possible to pin down the Vg modulation of individual hybrid transitions as they overlap to form one modulation extrema (e.g., figure 2.9 (c)).

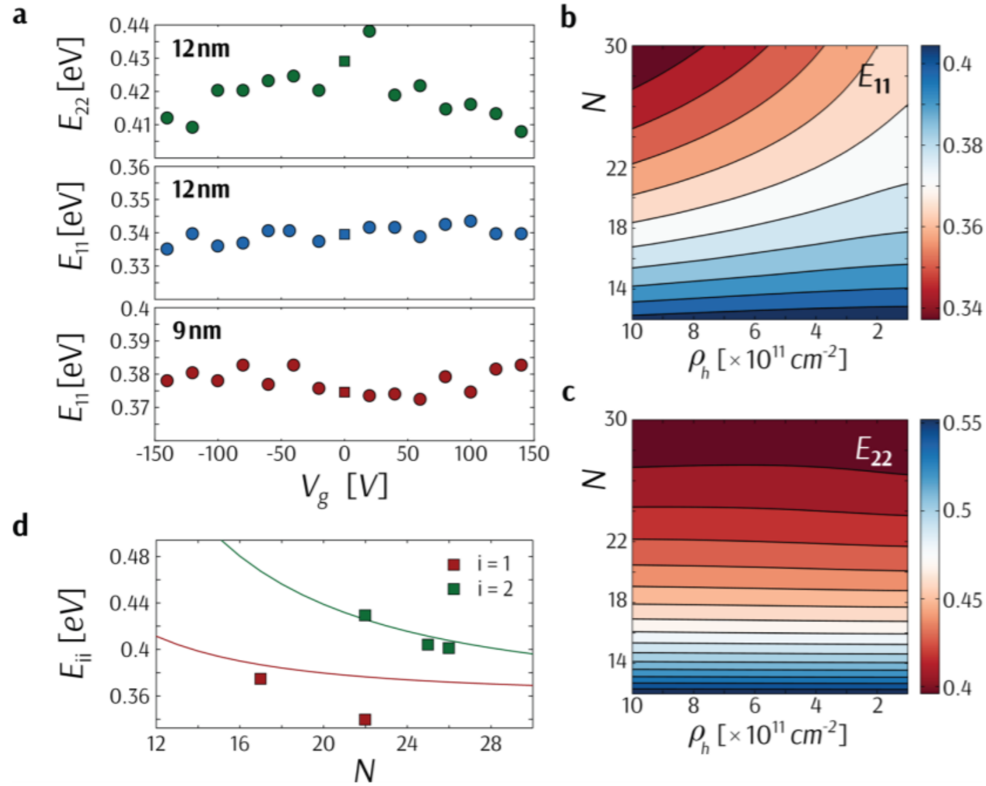

Figure 2.11. Layer dependence of electro-optic modulation in BP. (a) Gate voltage dependence of E_{11} and E_{22} in 9 and 12 nm thick BP. Squares denote the transition energy at zero gate voltage, obtained via interpolation of the modulation extrema at ±20 V. Contour plots of (b) E_{11} and (c) E_{22} transitions as functions of BP layer number and hole concentration computed via numerical methods. (d) Extracted transition energies at zero gate voltage vs BP layer number. The solid lines represent the data computed via eq 2.1.

In figure 2.11 (d), the same-index transition energies at zero Vg are shown as a function of the number of layers N. The strong decrease in transition energies with N is evident. Also shown in the figure are the energy transitions obtained from Eq. 2.1. While the extracted E_{22} at zero Vg follows Eq. 2.1, for 11 transition, Eq. 2.1 cannot properly recover the fast-descending trend observed in the measurements. These can be explained by referring to figure 2.8 c showing the presence of band bending at zero Vg in our samples. Compared with the E_{22} transition, the E_{11} transition is more susceptible to this band bending and therefore does not follow Eq. 1, which

describes only the flat-band condition. The deviation further increases in thicker samples as the first conduction (valance) subbands move toward lower (higher) energies, thereby sensing the band bending more effectively.

2.7 Conclusion and outlook

In conclusion, we have demonstrated electro-optic modulation of multilayer BP in the mid-IR range, which is dominated by the quantum confined Franz−Keldysh effect. Peaks of modulation level at different photon energies are related to contributions from optical transitions between different subbands, which show strong layer and gate voltage dependence. We expect the performance of a BP electro-optic modulator would be improved significantly when a high-k dielectric material such as HfO_2 is used as the gate oxide. When integrated with a waveguide, the light will propagate along the plane of the BP with a much longer interaction length. A recent study, using parameters consistent with our experimental results, predicts that a modulation level of 0.05 dB/ μm is attainable in a waveguide integrated BP modulator (shown in the next chapter). This suggests that a 5 dB modulation depth can be achieved with a 100 μm device. Such an electro-absorptive modulation utilizing the interband transition in BP as a narrowband 2D semiconductor should be much more efficient than using the carrier plasma dispersion effect in silicon. The performance can be further improved with novel device design and integration, as those have been proposed and implemented for graphene-based modulators working in the near-infrared regime. The above results and prospects indicate that BP is a very promising material in mid-IR optoelectronic devices for a wide range of applications.

Chapter 3. ON-CHIP INTEGRATED BLACK PHOSPHORUS DEVICES FOR MID-IR APPLICATION

Black Phosphorus has unique optical properties that have been exploited for many optoelectronic applications[124]. The strong tunability of the optical absorption, as well as the layer-dependent band structure, affords broadband and efficient optical photodetection and modulation from visible to mid-IR range[46], [49]–[52], [101]. While integrated mid-IR technology has been advancing rapidly due to the increasing demands for optical communication[125] and molecule sensing[126], [127], the mid-IR devices still rely on bulk materials that are not compatible with Si photonic platforms. Here, we demonstrated the integrated black Phosphorus devices for both photodetection and optical modulation within the mid-IR range. The black Phosphorus device is integrated with the Si waveguide and is modulated by the gate voltage to achieve the photodetection responsivity of 2.5 mA/W and optical modulation depth with 8 dB/mm in the experiment, and more than 40 dB/mm in the simulation. The simultaneous photodetection and modulation indicate that black phosphorus is the ideal material for realizing the integrated photonic devices for the mid-IR range which can lead to unprecedented optoelectronic applications.

3.1 MOTIVATION AND INTRODUCTION

Two-dimensional (2D) materials, including graphene, transition metal dichalcogenides (TMDCs), hexagonal boron nitride (h-BN), and black phosphorus (*bP*), have been the candidate materials for the active optoelectronic components in integrated photonics[8]. Varied types of 2D materials including the insulator, semiconductor, and semimetal enable the realization of the photodetectors, optical modulators, and light emitters[9], [24], [41], [80], [128] which can cover a broad optical spectrum range from ultraviolet to infrared and even terahertz regime. Even more exciting is the

strong tunability of the 2D materials where the strain, field, and doping can significantly modulate the properties of the materials such as optical absorption, photoluminescence, etc. Among all the 2D materials, black phosphorus (*bP*) has the unique property that its bandgap varies with the thickness due to its strong interlayer coupling. As result, the bandgap of the *bP* is layer dependent ranging from around 0.3 eV in the bulk to approximately 1.5-2.0 eV in monolayers (the corresponding optical wavelength range is 0.62-4.3 μm)[46]. In addition, *bP* has strong anisotropy electrical and optical properties, the effective mass of electrons and holes are small along the armchair crystal direction which indicates the excellent transport properties with hole mobility as high as 10^4 $cm^2/(V{\cdot}s)$[69]. Unlike the low-mobility TMDCs and gapless graphene, *bP* stands out from the 2D family as a very promising material for high-speed, low-loss, and hyperspectral optoelectronic applications. Indeed, varied optoelectronic devices based on black phosphorus have been demonstrated, operating in the visible and the IR bands[43], [129]. As the photodetectors, *bP* devices show high responsivity and low dark current which has improved performance compared to the graphene—and very high operation speeds up to 20 GHz[105]. Although the intrinsic black phosphorus is air-sensitive and degrades fast when interacting with water and oxygen[130]–[133], the recent progress in the chemical passivation has dramatically improved the air stability and extended the lifetime of the *bP* devices which can operate in the ambient condition over three months without discernible degradation in device performance[134]–[136].

Recently, the integrated Lidar technique, as well as the free space communication, has drawn attention[137]–[139]. Varied novel photonic devices have been proposed for self-driving vehicles where high-speed detectors and modulators are highly desirable. For free-space communications, our atmosphere offers several transparent windows in the mid-IR regime.

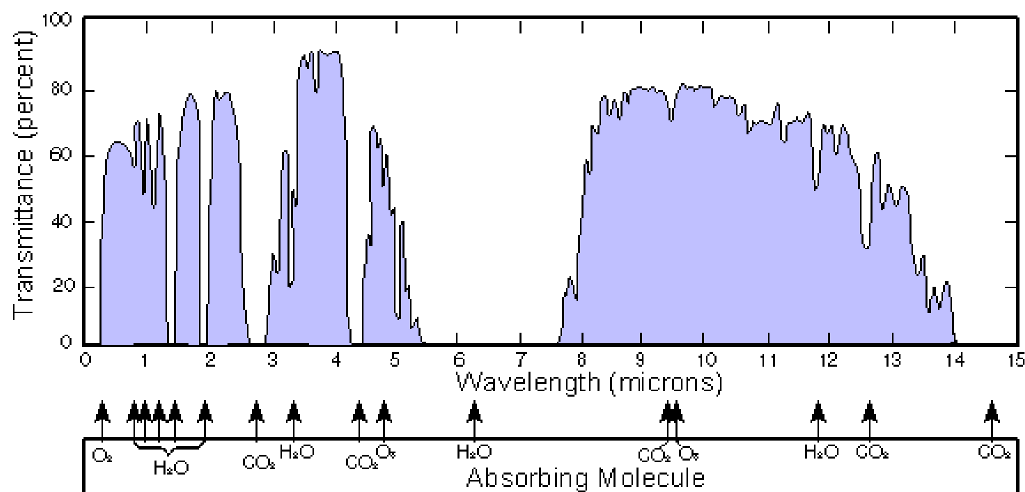

Figure 3.1. Optical transmittance of the atmosphere (%/km). The atmosphere offers two main transparency windows located at 3-4 µm and 8-10 µm[140].

Considering the multilayer *bP* with the bandgap around 0.3 eV, it is the ideal material for the optoelectronic devices operating within the transparent window around 3 µm.

Meanwhile, the development of mid-IR photonics will also benefit the research in chemistry and biology. Varied chemical molecules and gases have strong vibration absorption in the mid-IR regime, which can be used as the identifiers for molecule identification and gas sensing[126], [127].

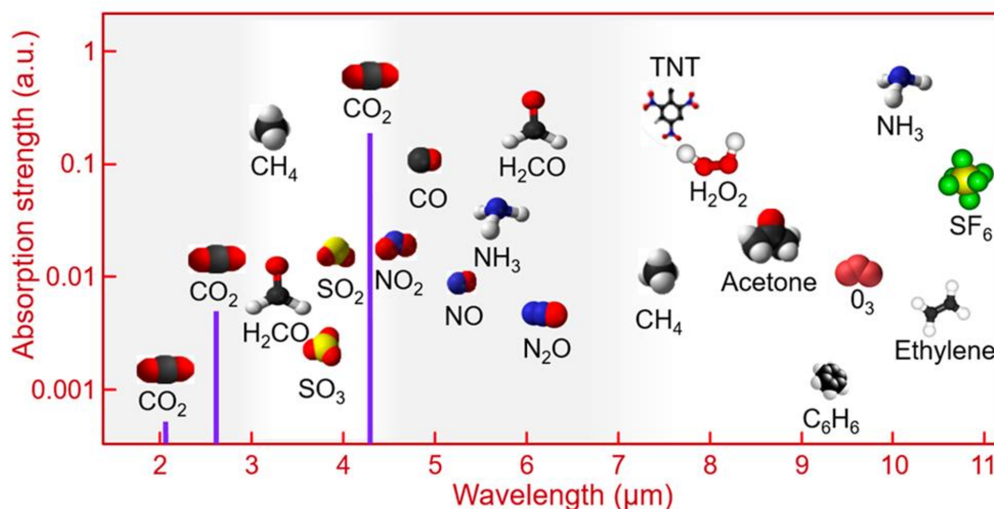

Figure 3.2. The absorption spectrum of the varied gas and organic molecules. The gas and organic molecules have strong vibrational absorption within the mid-IR region[141].

Although the mid-IR photonics has become crucial for the development of optical communication and chemical sensing, the commercial devices for the mid-IR regime still rely on the traditional bulk materials including InAsSb and HgCdTe which are usually high cost and unable to integrate with the Si photonic platform[102]–[104]. As an alternative, 2D materials such as *bP* and graphene have already been demonstrated for photodetection and electro-optical modulation in the mid-IR regime. Unlike the traditional materials which suffer the lattice mismatch during the growth process, the Van-der-Waals material can be easily stacked onto the patterned photonic structures by the wet or dry transfer methods. This enables the integration of the *bP* with Si photonics for the low-loss and high-speed photodetection and optical modulation. As recently reported by several groups, the optical absorption and electronic band structures of few-layer *bP* can be strongly modulated by the external electric field. Both quantum-confined Franz-Keldysh effect and Pauli-Blocking effect can significantly influence the optical absorption of *bP* which enables the strong optical modulation in the mid-IR regime[33], [37], [39]. Here, we integrated *bP* with the Si

photonic platform and demonstrated the broadband photodetection and optical modulation for the mid-IR regime especially for the atmosphere transparent window of the free space communication. By collaborating with the simulation results based on our materials characterization, we conclude that *bP* can be the candidate material for varied commercial applications including the photodetectors and modulators.

3.2 WORKING PRINCIPLE AND FABRICATION

To demonstrate waveguide integrated *bP* devices, we first design the rib waveguide structures with 400 nm etching depth, 600 nm height, and 1.6 μm width which can confine the optical mode with low propagation loss around 3 μm wavelength. The schematic of the *bP* integrated device is shown in figure 3.3 (a). With the patterned waveguide, 400 nm thickness SiO_2 is then deposited to planarize the substrate. Then 20 nm atomic layer deposition (ALD) Al_2O_3 is grown for electrical isolation and also for the gate dielectric materials. After the transfer of *bP* onto the waveguide region, the Titanium/Au electrodes are deposited by the Ebeam evaporation as the source, drain, and gate contacts.

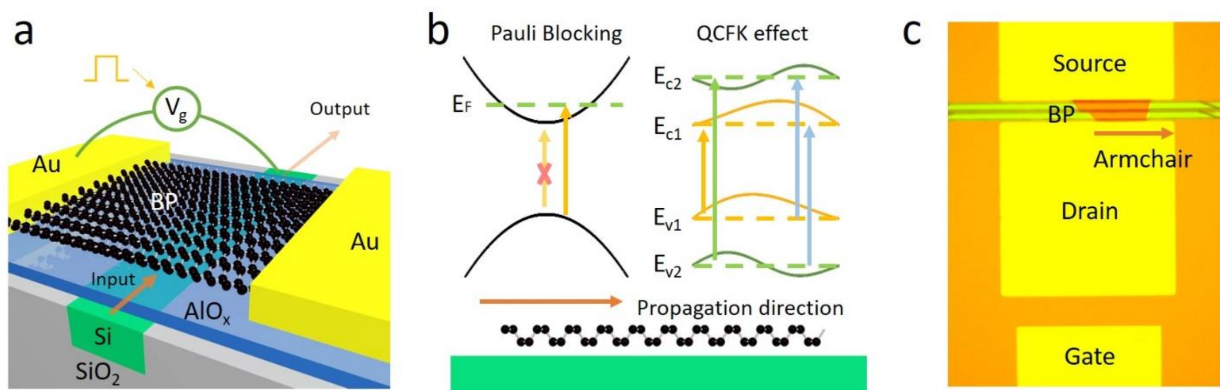

Figure 3.3. Device schematic and work principles. (a) Schematic illustration of the integrated bP modulator, featuring the guided mid-IR light by the silicon waveguide. The Si also performs as the back-gate electrode to modulate the optical properties of bP thin film. (b) Working principles

of the bP modulator. Both Pauli blocking and the QCFK effect can contribute to the optical modulation of bP thin film. (c) Optical image of the integrated bP device. The bP flake is oriented with the armchair (AC) crystalline axis along the light propagation direction.

With this device geometry, the integrated *bP* devices, in principle, can work as photodetectors and modulators simultaneously. As the voltage is applied between the source and drain contacts, the photocurrent is then efficiently collected. Meanwhile, as we applied the gate voltage, the doping and electric field are then induced to the *bP* thin film and modulate the optical absorption inside the materials according to the previous works. As shown in figure 3.3 (b), the change of the doping level in the *bP* results in the Pauli blocking effect also known as the Burstein-Moss shift which can effectively suppress the optical absorption. Meanwhile, the electric field results in the reduction of the bandgap and causes an opposite shift of the wavefunctions for electrons and holes, which is known as the quantum-confined Franz-Keldysh effect. It's responsible for the change of the wavefunction overlapping between electrons and holes and modulation of the *bP* absorption. By adopting these mechanisms, we then fabricated devices based on the device schematic shown in figure 3.3 (a). The optical image of our particular device with patterned electrodes is shown in figure 3.3 (c). By considering the anisotropy absorption of *bP*, the armchair direction is aligned with the propagation direction of the waveguide mode by the polarization-resolved Raman spectroscopy. According to the previous demonstration, this results in a stronger light-matter interaction with the TM mode of the Si waveguide.

3.3 Numerical Simulation for Integrated Black Phosphorus Device

Then, we apply the transfer matrix method to our free-space transmission measurement results to characterize the optical properties of the *bP* thin film. The *bP* devices can then be considered as

the stacked multilayers shown in figure 2a. By importing the refractive index of each layer, we can construct the transfer matrix for the material interface (M) and the optical propagation (P).

$$M = \frac{1}{t_{21}} \begin{bmatrix} t_{12}t_{21} - r_{12}r_{21} & r_{21} \\ -r_{12} & 1 \end{bmatrix}$$

$$P = \begin{bmatrix} e^{j\phi} & 0 \\ 0 & e^{-j\phi} \end{bmatrix} \tag{3.1}$$

By applying the transmission spectrum of the devices shown in Figure 3.4 (a), the extinction coefficient of the *bP* thin film at different gate voltages is then extracted. Here, the shaded area in the figure is corresponding to the transparent windows in the mid-IR regime where the extinction coefficient of *bP* in this range is also strongly modulated by the electric field. More importantly, the shaded region resides in the transparency window of the atmosphere which makes bP a candidate material for free-space communication.

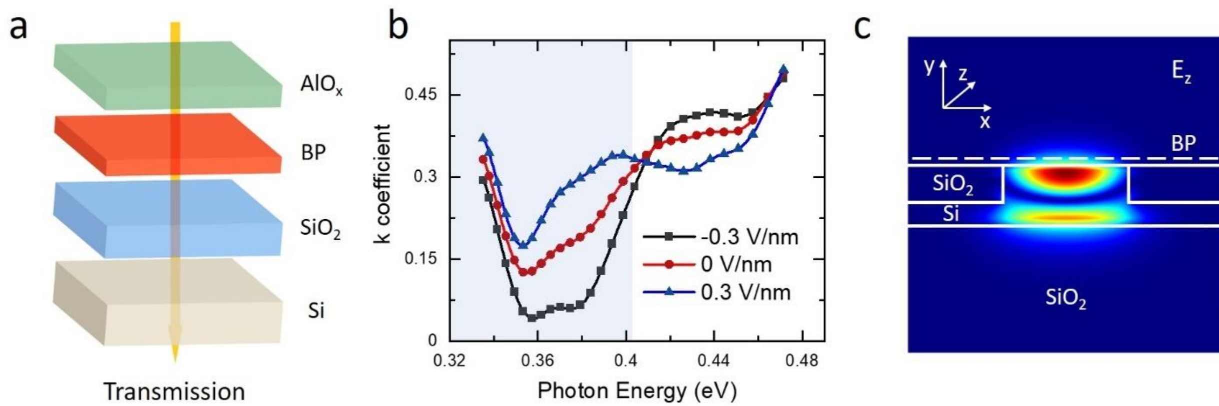

Figure 3.4. Simulation of the integrated bP devices. (a) Schematic structure of the free-space devices. Considering the multilayer structures, the extinction coefficient can be calculated from the transmission spectrum. (b) The calculated extinction coefficient of the bP thin film at different gate voltages. The optical absorption of bP is strongly modulated by the electric field especially in the optical spectrum range around 0.38 eV. (c) The simulation of the waveguide integrated device. The anisotropy of bP has been included in the simulation that the TM mode of the waveguide has a large mode overlap with bP thin film.

Considering this strong modulation of *bP* properties, we simulate the integrated *bP*-waveguide devices. We design the Ridge waveguide structure; the width is 1.6 um with a total height of 600 nm. Considering the anisotropic property of BP, the armchair direction of BP is aligned with the Ez component of the TM mode in the waveguide, which we expect most interaction with the mode of the waveguide, and more modulation could be achieved. We construct the anisotropic matrix of BP and simulate the absorption of the fundamental TM mode as indicated in figure 3.4 (c).

With the electric field ranging from -0.3 V/nm to 0.3 V/nm, the modulation depth can reach 40 dB/mm. the integrated *bP* devices show improved performance compared to other types of materials with integrated photonic platforms including graphene, Ge-Si, GeSn/SiGeSn MQW, Si free carrier absorption[64], [118], [119], [121], [142]. Also, by adopting the sandwiched photonic design for the graphene integrated devices, the modulation depth can be further enhanced (see section 3.7). Among varied types of 2D materials, *bP* integrated devices have the strongest modulation with very low loss in the mid-IR region. According to the simulation of the waveguide integrated *bP* devices, 5 dB modulation with less than 1 dB insertion loss can be realized with 90 μm *bP* which meets the requirements for commercial applications.

3.4 Measurement Schematics

To measure the optical modulation of the integrated bP devices, the butt coupling setup is then introduced which can support the broadband transmission with high coupling efficiency. We used a mid-IR optical parametric oscillator (Firefly-IR, M Squared) as the light source outputting in the spectral range of 2.5-3.7 μm. As shown in figure 3.5, the tunable mid-IR light is coupled to mid-IR fiber which is connected to the end of the waveguide devices.

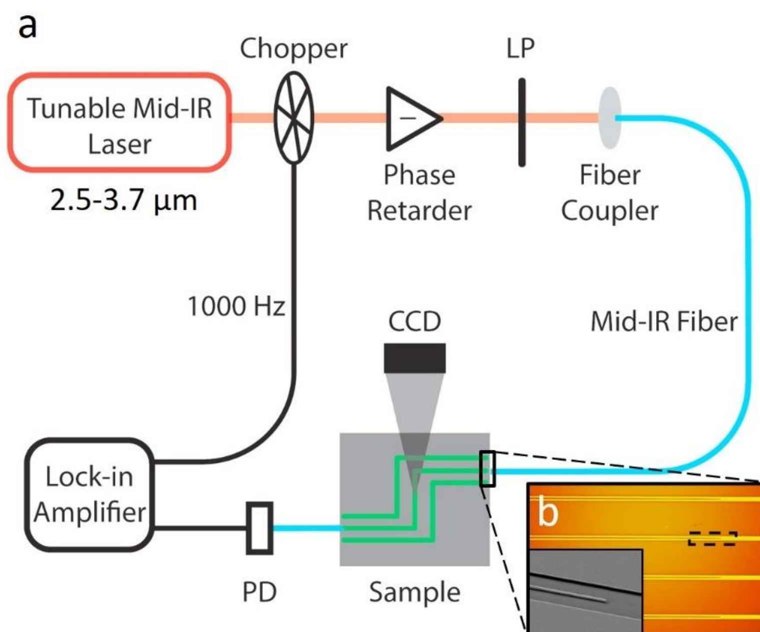

Figure 3.5. Measurement Schematics. (a) The setup design for the photodetection and modulation measurements of integrated bP device. The phase retarder with a polarizer is used to control the output polarization of fiber to be aligned with the TM mode of the Si waveguide. (b) The optical image of the inverse tapered structures. Inset: SEM image shows the zoom-in feature of the tapered end where the width of the tapered end is about 150 nm.

To increase the coupling efficiency, the inverse tapered structures at the end of the waveguide are used to overcome the mode mismatching between the fiber and the Si waveguide. With the help of this tapered structure, the mid-IR light can be efficiently coupled from fiber to the waveguide and propagates through the *bP* devices. Then the light is collected by another mid-IR fiber connected with a photodetector for the transmission measurement. According to the SEM image of the device, the end of the taper is around 150 nm which will have the divergent mode profiles close to our mid-IR fiber. For the particular device, the optical transmission is calibrated which has transmitted signal several magnitude orders larger than the noise.

3.5 INTEGRATED BLACK PHOSPHORUS PHOTODETECTOR

To characterize the device performance of *bP* devices, we first apply the bias voltage to measure the photocurrent when incident the mid-IR light. By scanning the optical wavelength, we measure

the photocurrent/responsivity spectrum of the *bP* devices at bias voltage 0.2 V. From the responsivity spectrum of the *bP* device, there are three resonances which are corresponding to the band transitions of the *bP* thin film. Considering the 14-nm bP thin film, there are four possible band transitions located within our light source range. According to the band transition diagram shown in figure 3.6 (a), the first and third responsivity peaks are related to E_{11} and E_{22} transitions, while, the hybrid transitions of E_{12} and E_{21} cause the small bump in between. These hybrid transitions should be symmetry forbidden. However, the initial doping and band bending inside *bP* break the symmetry and enable the hybrid transitions.

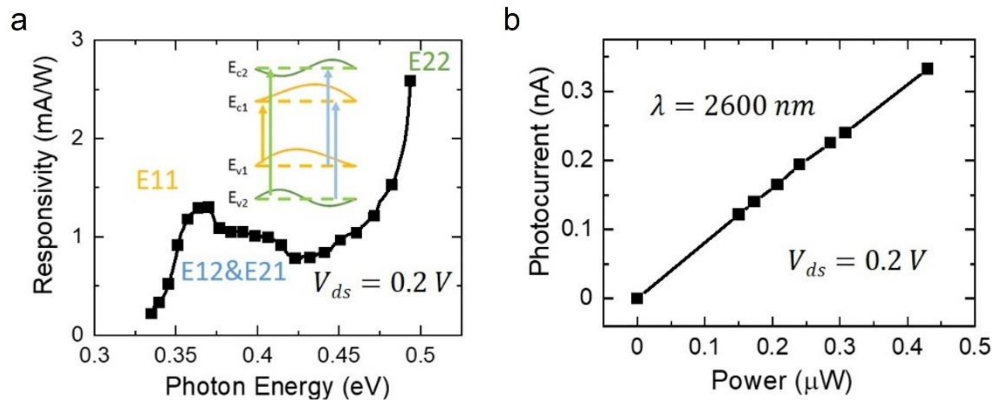

Figure 3.6. Integrated *bP* device for photodetection. (a) The responsivity spectrum of *bP* photoresponse. There are three resonances in the responsivity spectrum which are corresponded to the subband transitions of *bP* thin film. (b) The power-dependent photocurrent measurement of integrated *bP* device. The device can achieve the photodetection at sub μW regime.

Here, we demonstrate an integrated *bP* photodetector for mid-IR applications with external responsivity up to 2.5 mA/W. At a certain wavelength (λ=3 μm), the power-dependent optical response of integrated *bP* devices is characterized. The photocurrent of *bP* devices shows the linear dependence with the incident power which is crucial for photodetection.

3.6 INTEGRATED BLACK PHOSPHORUS ELECTRO-OPTICAL MODULATOR

Finally, we demonstrated the broadband mid-IR modulator by integrating the bP with Si waveguide and characterized the modulation depth of the integrated device. For the gate modulation, we connect the gate electrode with the Si rib waveguide. As the gate voltage is applied, the electric field will be formed through the Si to modulate the bP thin film. Considering the high-k dielectric layer (AlO_x), the optical absorption of bP is efficiently modulated, and consequently, the transmission of the integrated bP device is modulated by the external electric field. The 2D plot in figure 3.7 (a) shows systematic measurement results of the modulation level when both wavelength λ and gate voltage V_g are continuously scanned. The modulation M always refers to the transmission when the gate voltage is 0 V: $M = [T(V_g) - T(0)]/T(0) = \Delta T/T(0)$.

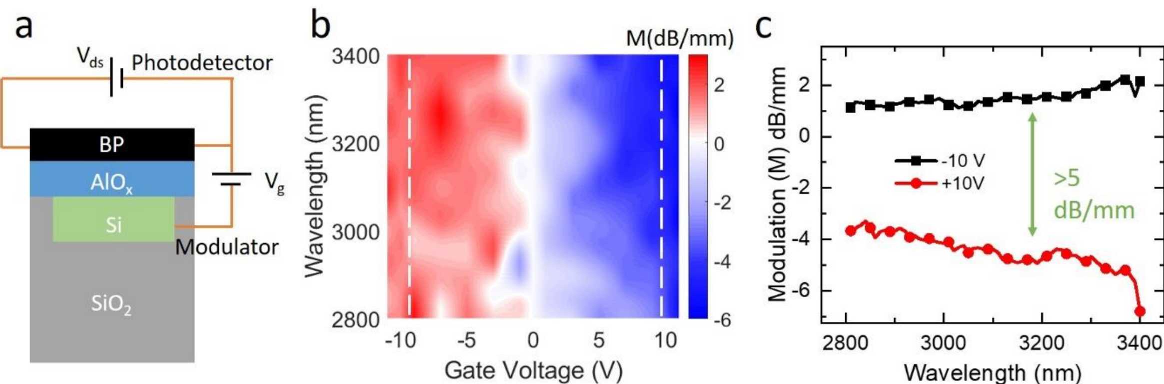

Figure 3.7. Integrated bP device for optical modulation. (a) The measurement schematic for the integrated bP device. This device can be operated as both the photodetector and modulator. (b) The modulation level is measured as the function of the wavelength and applied gate voltage, featuring the max modulation of about 8 dB/mm. (d) Measured modulation at gate voltage $\pm 10\ V$, the device shows broadband modulation in the mid-IR range from 2800 nm to 3400 nm.

According to the modulation results, the transmission of the devices is depending on the applied gate voltage. At a certain wavelength, the modulation depth is up to 8 dB/mm. For characterization, we extracted the modulation of the transmitted signals at two different gate voltages ($\pm 10\ V$). As

shown in figure 3.7 (c), the *bP* device shows a broadband modulation from 2800 nm to 3400 nm. The reason that measured modulation is weaker than the simulation, can be explained by the fact that the gate voltage induced through the intrinsic Si back gate cannot efficiently modulate the bP. With more efficient gate control such as ionic liquid, the modulation depth can be further enhanced. Also, the waveguide region of the device is not a perfectly flat substrate that induces the inhomogeneous broadening of transition resonances and significantly degrades the performance of the bP modulator. The more careful planarization method such as the Chemical Mechanical Polishing (CMP) and the device geometry with the top gate electrodes can contribute to the stronger modulation results.

Although the modulation is relatively weak compared to the simulation results, the modulation depth measured in our integrated *bP* device is already comparable to the graphene mid-IR modulator (sandwiched in the ChG waveguide)[143]. As shown in Table 3.1, the modulator device based on the free-carrier absorption of Si only has a modulation depth of about 0.5 dB/mm which is much smaller than the results measured in the integrated bP device.

Table 3.1. Overview of the mid-IR modulator

EO Materials	**Max MD (dB/mm)**	**Wavelength (μm)**
Si (free-carrier)	0.5	2
Graphene (Sim.)	8.2	2.05-2.45
Graphene (Exp.)	7.8	2.05-2.45
BP (Sim.)	>40	3-3.4
BP (Exp.)	8	2.8-3.4

To compare with the other integrated modulator devices, our bP devices already show improvement in the modulation depth. The current performance is still below the early simulation

results or other theory predictions, 40 dB here, there is much freedom we could improve in this system by optimizing the fabrication process and protecting the bP from degradation. Here, we also compare our bP device to the commercial acousto-optic modulator (ISOMET) [144] which usually has an aperture size of 6*14 mm to achieve enough modulation depth. The integrated bP devices show advantages over other types of optical modulators that the footprint of the modulator can be further reduced with a similar modulation depth.

3.7 THE INTEGRATED PLATFORM FOR HIGH-EXTINCTION MODULATION

Considering the waveguide integrated devices, the modulation is far below the simulation results. There are a few problems with these waveguide devices. First, only the evanescent field is leaked into BP, the light-matter interaction is very small. As result, it requires a 180 μm long device to achieve enough modulation. Secondly, the etched waveguide region must be planarized for the following transfer process of BP. Typically, the SiO_2 is deposited to fill the etching region and planarize the device. However, the thermal evaporated SiO_2 is very lossy in the mid-IR range and causes additional internal loss in the waveguide devices. The last but most important thing is that the planarized region cannot be perfectly smooth, the transferred BP on this region will be very ununiform. This will degrade the optical property of the BP because 2D materials are very sensitive to the surface interactions and the local strain.

3.7.1 *Multi-pass waveguide design*

Considering the exfoliation of the bP flake, it would be challenging to achieve >100 μm size device. With the flake size of 50 μm, the interaction length would be limited which results in a small modulation depth. Fortunately, by taking the advantage of Silicon photonics, enough modulation depth can be achieved within a 50 μm × 20 μm footprint. By designing the multi-pass

waveguide as shown in figure 3.8, the light would propagate through the device with 5 passes. According to our simulation, 5dB modulation depth with less than 1 dB insertion loss can be achieved in this multi-pass waveguide device.

3.7.2 *Ionic liquid for stronger field modulation*

As discussed above, the waveguide device suffers the weak back gate modulation due to the intrinsic silicon. Also, the atomic layer deposition of AlO_x for the gate and material protection will add additional insertional loss to the waveguide device. With the complicated fabrication process, the bP thin film will expose more to the ambient condition which can degrade the optoelectronic properties of bP. To achieve the stronger gate modulation, the ionic liquid(iL) BMIM-BF4 is deliberately chosen for ambient and room temperature measurement because it is reported that the air degradation of BP thin film can be protected for tens of days in the air by directly applying the iL on the BP flake[145]. The applicable voltage window of the iL is from -1 V to 1 V which can modulate the carrier concentration of the thin film in the order of $10^{13}/cm^2$. It can achieve more than 10 times of the modulation range by using the AlO_x dielectric layer.

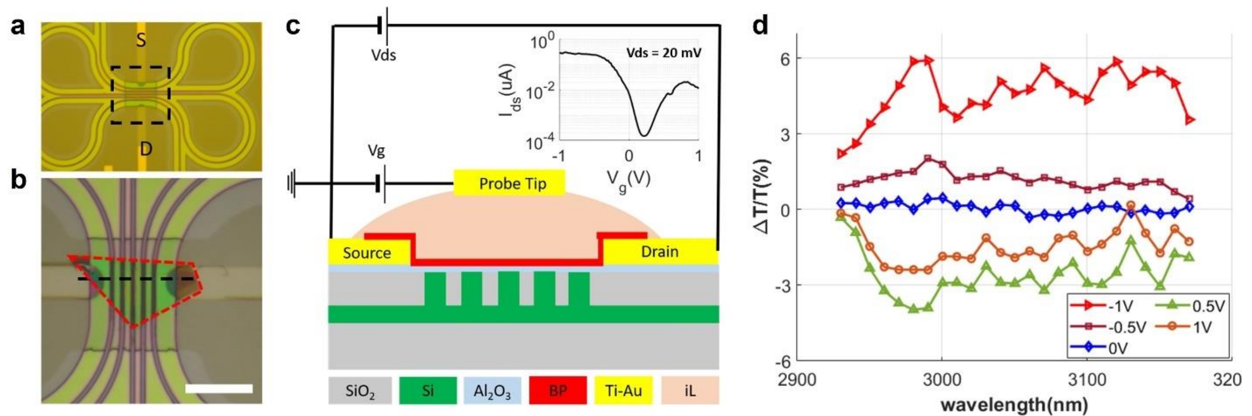

Figure 3.8. Characterization of the iL-gate devices. The optical images of (a) the multi-pass waveguide and (b) the bP-integrated waveguide. BP is indicated with the red-dashed line. The green square region is planarized with SiO_2. Scale bar: 20 µm. (c) The cross-sectional schematics

of the iL-gate device. Inset: Field-effect modulation of BP conductance. (d) Transmission changes normalized to that of zero gate voltage scanned around 3-um at different gate voltages. The maximum modulation occurs as 10% at 2.98 um between gate voltages of −1 and 0.5 V.

The electrical characterization of the test iL device shows a strong gate modulation of bP conductivity with a bias voltage of 20 mV (Figure 3.8). The IV characteristics indicate the effective doping of bP by ionic liquid with an on-off ratio over 1000 and the charge neutral point at 0.3 V. The modulation of optical transmission for the iL device was demonstrated with more than 10 dB/mm and a wide spectral range from 2950 nm to 3150 nm.

3.7.3 *The plasmonic nanogap for enhanced light-matter interaction*

To further enhance the performance of the optical modulation, the plasmonic nanogap geometry is also introduced. A more compact footprint and higher modulation depth can be achieved by using a metal-insulator-metal plasmonic waveguide (MIM-WG) structure because of its strong field enhancement, which increases light-matter interaction[146]. The plasmonic guided mode for 3.3-μm light is simulated with FEM with and without BP integrated on top of the waveguide, according to the geometry shown in Figure 3.9 (a) with the varying gold thickness (t_{au}) and slot width (w_{slot}). The refractive index (n) and anisotropic extinction coefficient (k) of BP are cited from reference[146]. After the plasmonic mode is simulated, the absorption coefficient (dB/μm) is calculated from the imaginary part of the complex effective mode index.

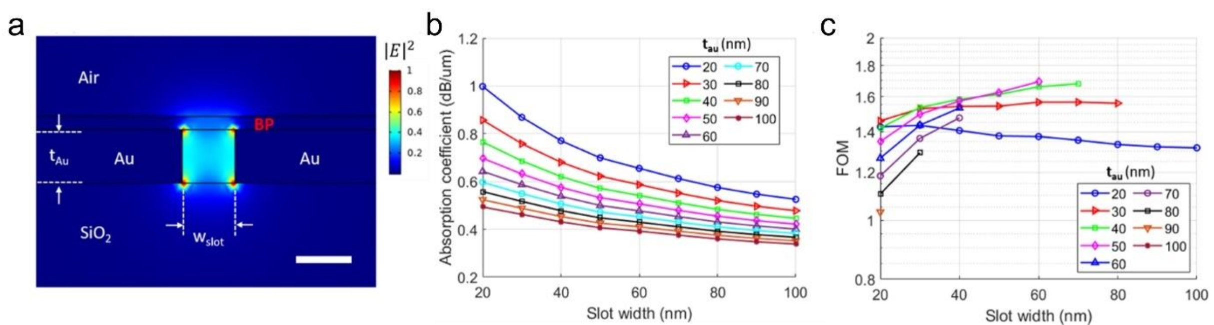

Figure 3.9. Integrated plasmonic devices for enhanced optical modulation. a) Schematics of MIM-WG simulation. Scale bar: 40 nm. The electric field is highly confined near the edges of gold and BP nearby, enhancing light-matter interaction. b) The modulation strength, defined in the main text, is calculated with varying gold thickness and slot width. c) Figure of Merit, defined in the main text, considering both modulation depth and insertion loss.

The modulation strength is calculated from the change of the absorption coefficient when assuming the extinction coefficient of BP is modulated between 0.3 and 0.05. The results show that only 5 μm long MIM-WG with 20 nm slot width and 20 nm gold thickness is sufficient to achieve 5 dB modulation depth (*M*). However, as the gap size and thickness of gold reduces, the insertion loss also increases. To optimize for a high modulation depth (*M*) while minimizing the insertion loss (*IL*), we define a figure of merit (FOM) as: FOM=*M*/*IL* with the restriction that *M*>5 dB and device length less than 10 μm. With these conditions, we find 50-nm thick gold is optimal for achieving *M*=5 dB, *IL*=2.5 dB with a BP flake of 8 μm long.

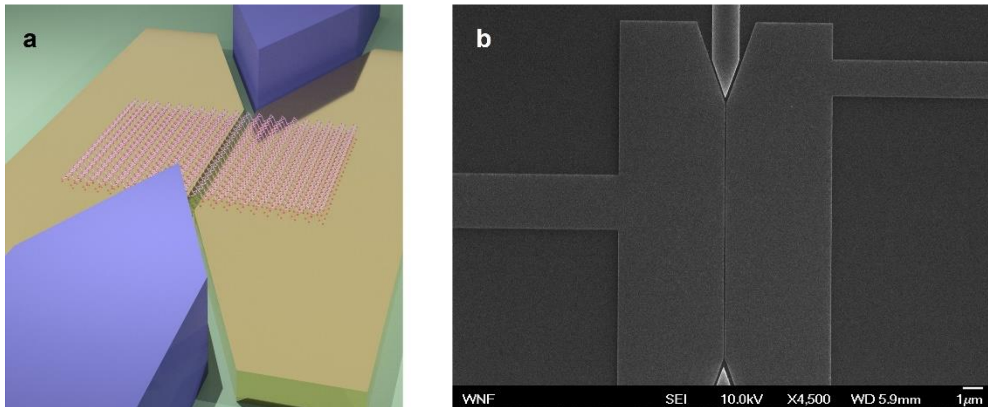

Figure 3.10. Device schematic for the integrated plasmonic device. (a) 3D illustration of the plasmonic nanogap device. (b) The SEM image of the fabricated plasmonic device. The gap of the plasmonic device is 50 nm.

The schematic of the plasmonic device is shown in figure 3.10, the armchair direction is aligned with the TE mode of the plasmonic waveguide which has stronger absorption in the bP flake. For

the fabrication of the device, we first patterned the Si waveguide with a tapered coupler by Ebeam lithography and ICP etching. Then, aligned writing of the plasmonic nanogap has been patterned with less than 10 nm deviation by using the high-resolution mode of the JEOL-6300 Ebeam system. As shown in figure 3.10 (b), we have fabricated the nanogap with 50 nm and well-aligned with the Si tapered coupler.

3.8 CONCLUSION AND OUTLOOK

In summary, we have demonstrated the waveguide integrated bP photodetector and modulator for the mid-IR applications. For the photodetection, a broadband photoresponse is demonstrated with the responsivity up to 2.5 mA/W. Meanwhile, we achieve the optical modulation with the modulation depth of 8 dB/mm in the experiment and 40 dB/mm based on the simulation. We believe that the large modulation predicted by our simulation is promising as we introduce the top gate geometry to achieve more efficient grate control and also planarize the waveguide region to reduce the inhomogeneous broadening of bP optical resonances. By taking advantage of the novel photonic design such as plasmonic waveguide, and photonic crystal structures, the modulation depth can be further enhanced which can easily meet the criteria for the commercial applications. The above results for the simulation and experiment of the integrated bP device indicate that bP has great potential in mid-IR photonics, especially for broadband photodetection and optical modulation.

Chapter 4. TRANSPORT OF 2D EXCITONS WITH SURFACE ACOUSTIC WAVE

Excitons are elementary optical excitation in semiconductors. The ability to manipulate and transport these quasiparticles would enable excitonic circuits and devices for quantum photonic technologies. Recently, interlayer excitons in 2D semiconductors have emerged as a promising candidate for engineering excitonic devices due to their long lifetime, large exciton binding energy, and gate tunability. However, the charge-neutral nature of the excitons leads to a weak response to the in-plane electric field and thus inhibits transport beyond the diffusion length. Here, we demonstrate the directional transport of interlayer excitons in bilayer WSe_2 driven by the propagating potential traps induced by surface acoustic waves (SAW). We show that at 100 K, the SAW-driven excitonic transport is activated above a threshold acoustic power and reaches 20 µm, a distance at least ten times longer than the diffusion length and only limited by the device size. Temperature-dependent measurement reveals the transition from the diffusion-limited regime at low temperature to the acoustic field-driven regime at elevated temperature. Our work shows that acoustic waves are an effective, contact-free means to control exciton dynamics and transport, promising for realizing 2D materials-based excitonic devices such as exciton transistors, switches, and transducers up to room temperature.

4.1 INTRODUCTION

4.1.1 *Excitons in Transition metal dichalcogenide*

Two-dimensional (2D) transition metal dichalcogenide (TMDC), such as MoS_2 and WSe_2, has shown the potential in enabling the next generation of optoelectronic devices such as nanolaser,

photodetector, and nonlinear optics elements[9], [12], [15], [24], [41], [44], [147]–[150]. With improved sample quality, 2D TMDC and their heterostructures have shown high photoluminescence quantum yields, long exciton lifetime, large nonlinear optical coefficients, and efficient electrooptic tunability. Thanks to the reduced screening effects at monolayer limit, exciton binding energy can reach several hundred meV[11]–[13], orders of magnitude higher than that in conventional semiconductors such as GaAs or InGaAs[151]. The large exciton binding energy makes it possible to realize stable exciton-polariton and Bose-Einstein condensation (BEC) in these 2D materials at room temperature[152]–[154]. Furthermore, the hexagonal lattice structure with broken inversion symmetry gives rise to the valley degree of freedom, which can be selectively addressed with circularly polarized light[11], [54], [155]. TMDCs have integrated with photonic cavities to enhance the light-matter interaction to reach the strong coupling regime in which exciton-polaritons are formed[22]–[29], [156]. Because exciton-polaritons have ultrastrong nonlinearity, photon-like coherence, and excitonic interactions, they present a prototypical model system for studying quantum optical phenomena, many-body physics (e.g. BEC), and developing low-threshold nano lasers and chip-based quantum simulators.

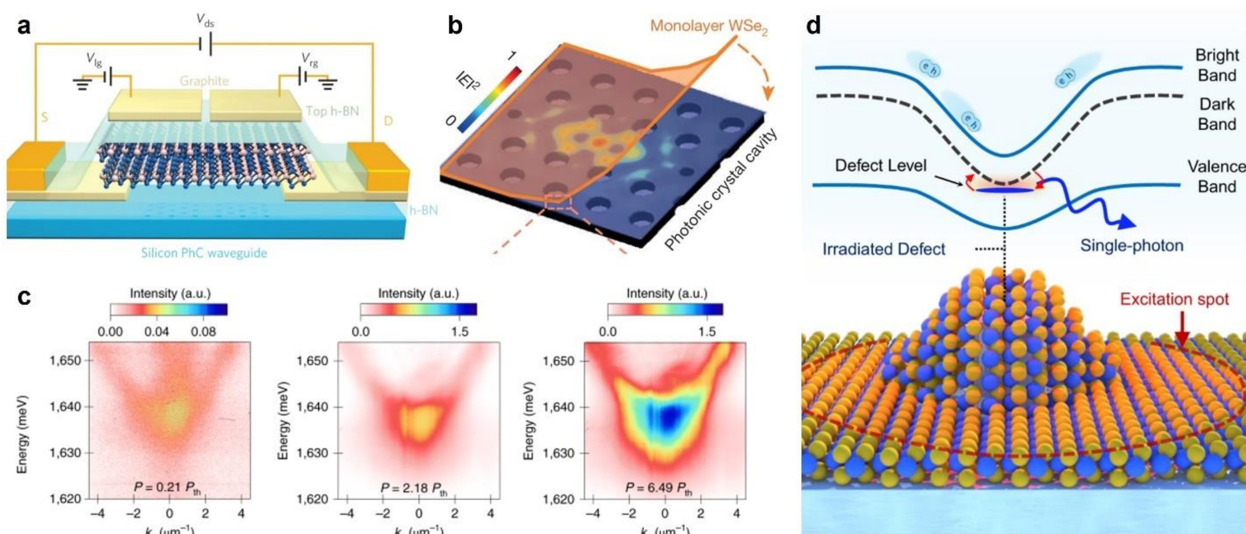

Figure 4.1. Excitonic device based on the transition metal dichalcogenides. (a) The waveguide integrated LED and photodetector based on monolayer $MoTe_2$. In LED mode, the light emitted from the p–n junction propagates through the waveguide and is coupled out at the grating coupler. In photodetector mode, incident light is coupled to the waveguide through the grating coupler and is detected by the $MoTe_2$ p–n junction.[44] (b) Nanocavity laser based on the monolayer WSe_2. A continuous-wave nanolaser operating in the visible regime is thereby achieved with an optical pumping threshold as low as 27 nanowatts at 130 kelvin.[16] (c) Bose-Einstein condensation of the exciton-polariton in an atomically thin crystal. Exciton–polaritons emerge from an atomically thin crystal of $MoSe_2$ embedded in a dielectric microcavity under optical pumping at cryogenic temperatures.[154] (d) Strain and defect-engineered WSe_2 single-photon emitter. It enables site-controlled single-photon emission up to 150 K.[157]

Excitons in semiconductor systems can be optically excited and read out, thereby encoding and storing optical signals into the excitons' spin, valley, and orbital degrees of freedom[56]. In analogous to electronic circuits, circuits with excitons as the active information carriers have been envisioned, which transport and manipulate excitonic states with applied electrical and magnetic fields[57], [62]. Transducing between photons and solid-state media, such excitonic circuits can directly process optical signals and regenerate light without additional optical-electrical conversions so that they can be very efficient[158]. However, unlike electrons or holes, charge-neutral excitons experience no net force under uniform electric fields. They can also be dissociated by a moderately strong in-plane electric field if the binding energy is small, for example, in GaAs quantum well systems[159], [160]. Therefore, diffusion has been one of the main mechanisms utilized for exciton motion in GaAs[161], [162] and 2D materials[62], [163], [164]. Particularly, in GaAs systems, the high mobility of exciton has enabled 10s of microns diffusion length at low temperature[158]. Compared to GaAs quantum wells, excitons in 2D transition metal dichalcogenides (TMDCs) (e.g., MoS_2, $MoSe_2$, WS_2, WSe_2) have strong resonances even at room temperature (RT) [13], [17], [26], [165], making them promising for a plethora of optoelectronic

and quantum applications[8], [16], [27], [29], [152]. Particularly, the indirect excitons (IXs) in bilayers and heterobilayers of TMDCs have additional desirable properties[152], [166]–[169]. Because these IXs consist of electrons and holes separated in different layers and valleys, their population lifetimes at low temperatures are up to 100s of nanoseconds[58], facilitating long-range transport before relaxation. Importantly, IXs have a permanent perpendicular dipole moment so that their energy can be tuned with an out-of-plane electric field[74], [170]. Taking interlayer exciton of $MoSe_2/WSe_2$ heterostructure as an example, the electron and hole are located in a different layer and form type-II band alignment with the vertical PN junction. This will contribute to a perpendicular polarization for interlayer exciton and can interact with the perpendicular electric field. As shown in the figure 4.2, the interlayer exciton energy shifts due to the applied field with a perpendicular dipole polarization about $e \times 7.5 \times 10^{-10}$ m.

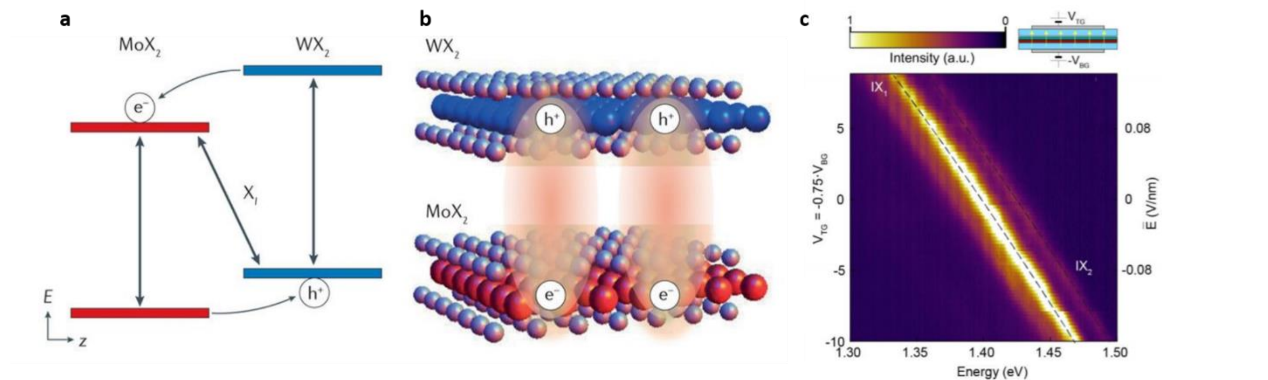

Figure 4.2. Interlayer valley excitons in 2D semiconductor heterostructures. (a) Energy-level diagram showing type-II band alignment for a typical MoX_2–WX_2 heterojunction. Ultrafast interlayer electron transfer to the MoX_2 or hole transfer to the WX_2 results in the formation of interlayer exciton states. (b) Illustration depicting spatially indirect, interlayer excitons in a MoX_2–WX_2 heterojunction. The oriented dipole moments out of the plane cause strong exciton repulsion as well as large Stark shifts under applied electric fields. (c) Map of photoluminescence emission as a function of applied gate voltages V_{TG} and V_{BG} when sweeping at constant doping.[55]

More interesting, with the small-angle twisting of the $MoSe_2$ and WSe_2, the signature of trapped exciton induced by the Moire potential has been confirmed which can create the photon within the quantum regime and be the candidate system for achieving the programmable single-photon emitter arrays[167]–[169], [171].

4.1.2 *2D Excitonic transistor*

Considering the layer-separated electron and hole of the interlayer exciton, this indirect exciton formed in this heterostructure will have the perpendicular electric polarization that the energy of the exciton shifts in response to the perpendicular electric field[57], [172], [173]. Inspired by this, the energy of interlayer exciton is controlled by the vertical field and the energy gradient will be responsible for the drift current of the exciton referring to the electron case. Based on this local control of the exciton profile, people have developed the idea of the exciton transistor based on the interlayer system. As we discussed before, the $MoSe_2/WSe_2$ system supports the interlayer exciton with fixed dipole polarization. As we apply the electric field, the exciton diffusion could be controlled. With the electric field, you could create a potential barrier that will impede the exciton diffusion. Compared to the free diffusion case, there was an obvious difference. This is a prototype of the exciton transistor where the exciton flow is impeded by the energy barrier as shown in figure 4.3. However, due to the low diffusion coefficient of the interlayer system, the exciton diffusion is limited, here only shows 1 µm propagation[57].

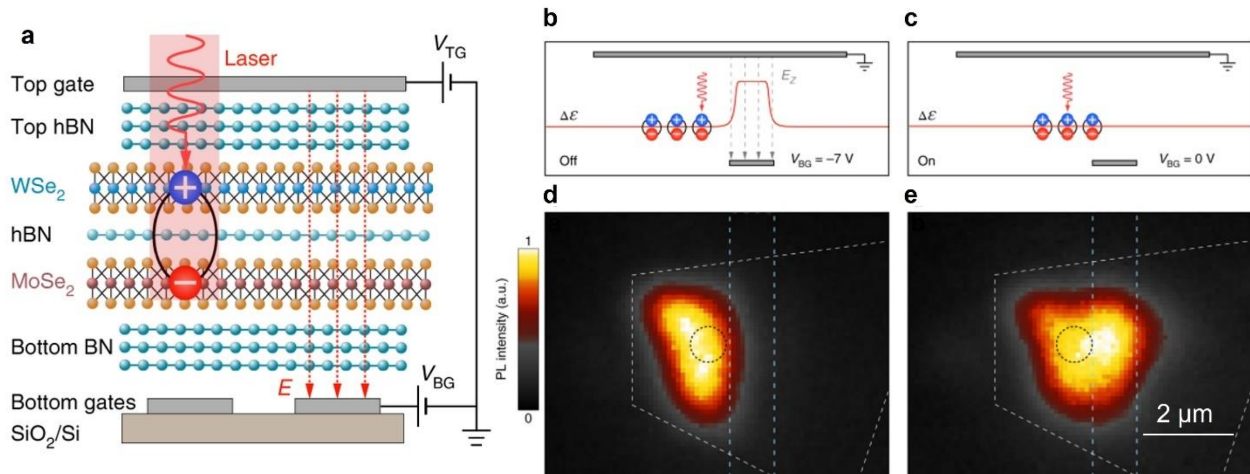

Figure 4.3. Exciton transport in a van der Waals heterostructure. (a) Schematic of the device structure illustrating the top and bottom split gates, as well as electrical connections. (b) (c) Numerically simulated exciton energy profile (red line) in the off (b, VTG = 0 V, VBG = −7 V) and on (c, VTG = 0 V, VBG = 0 V) states of the excitonic transistor. (d) (e) Real-space CCD images of the emitted PL intensity for the off (b) and on (c) states. The black dashed circle indicates the laser spot. Scale bar, 2 μm.[57]

After this, the Singapore group has discovered the interlayer exciton in the bilayer WSe2 system which has a larger diffusion coefficient compared to the twisted Moire system as shown in figure 4.4[173]. The exciton flux show a stronger effect, where the exciton trap and spreading state have a larger difference and the effective propagation length is around 2 μm. Currently, all the demonstrations of the 2D exciton transistor rely on the exciton repulsion which needs large exciton density and the propagation length is limited.

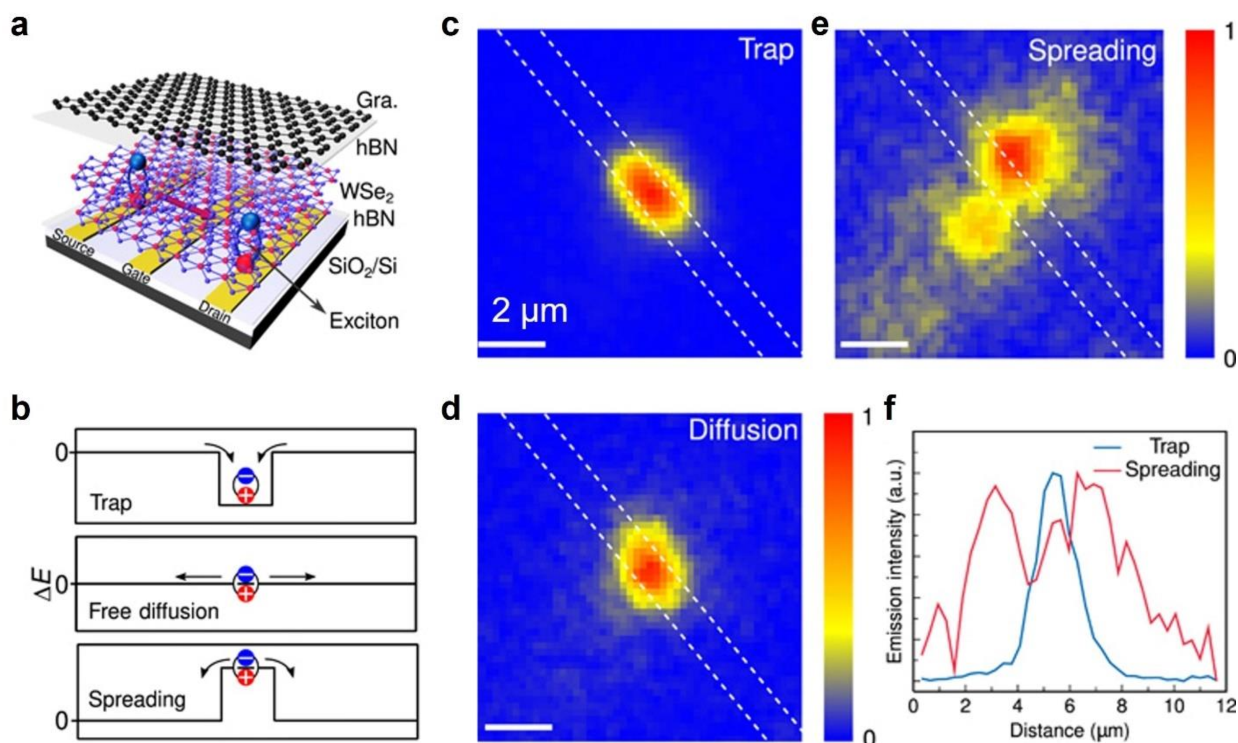

Figure 4.4. Control 2D potential energy of interlayer excitons by the electrical field. (a) Schematic structural diagram of one excitonic transistor. (b) Schematic of exciton energy offset for exciton dynamic regimes of trap, free diffusion, and spreading when applying negative (top), zero (middle), and positive (bottom) gate voltages, respectively. (c to e) Real-space emission intensity map for exciton trap, diffusion, and spreading, corresponding to gate voltage VG = −9, 0, and 11 V, respectively. The white dashed lines indicate the bottom electrode edges. Scale bars, 2 μm. (f) Emission intensity profiles across the electrode were extracted from the real-space emission intensity maps. The excitation spot was focused on the center of the electrode. The excitation power is ~200 nW operated at 532 nm.[173]

4.1.3 *Review of the surface acoustic wave and its application*

The surface acoustic wave is the phonon wave that propagates along the surface of the materials. It's usually exited on the piezoelectric substrate by using the interdigital transducers[174]. The surface acoustic wave has many interesting properties: I. It's the highly confined RF waves that can be shrined down to the sub-micron scale. II. It's the strain wave together with the piezoelectric

field. III. It can easily interact with varied physical and quantum systems such as the transmon qubits, spin qubits, and color centers as shown in figure 4.5[175]–[179]. Recently, the acoustic approach especially the surface acoustic wave has become a standard technique in quantum computing that could couple and modulate the superconducting qubits[174]. With those properties, the acoustic approach can also be applied to other systems such as photonic and excitonic systems.

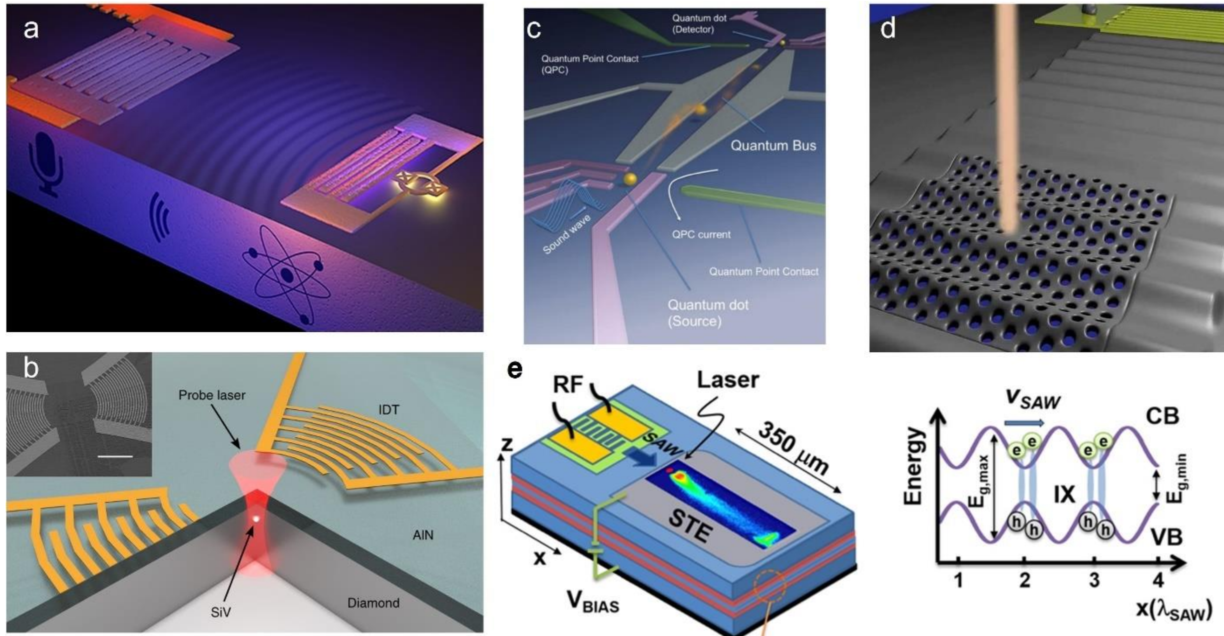

Figure 4.5. Application of surface acoustic wave to different physical systems. (a) Propagating phonons coupled to an artificial atom. nonclassical interaction between surface acoustic waves and an artificial atom has been demonstrated in the regime of strong coupling.[178] (b) Schematic of our diamond SAW device. The interdigital transducers (IDTs) generate acoustic waves due to the piezoelectric response of aluminum nitride (AlN). The modulation of SiVs in the diamond are probed using a focused laser beam.[175] (c) Schematic of the experimental set-up. An interdigital transducer (IDT) launches a SAW train towards the single-electron circuit to remotely drive the electron transfer.[177] (d) Photonic crystal nanocavity, deformed by surface acoustic wave (SAW). A periodic modulation of the optical mode exceeding eight times its linewidth has been resolved.[176] (e) Samples for indirect exciton (IX) transport by surface acoustic waves (SAWs). *IX* transport by the moving modulation of the conduction (CB) and valence bands (VB) in a DQW.[179]

To actively transport excitons with controlled directionality, surface acoustic waves (SAW) have been employed to effectively transport excitons in GaAs quantum wells[174], [179]–[182]. Over 100s of microns transport distance is achieved at a temperature below < 4K[179], [180]. However, the low exciton binding energy of only a few meVs in GaAs prohibits operation at higher temperatures. In comparison, the exciton in the 2D TMDCs have much larger binding energy that can be stable even up to room temperature. However, the earlier attempts to the exciton in TMDCs only show strong dissociation of the exciton into free carriers[183], [184]. The in-plane component of the piezoelectric field will couple to the exciton and induce the shift of the electron and hole in the opposite direction. As result, only the emission suppression and the stark shift of the exciton have been observed in the TMDCs. For this report, we are coupling the perpendicular component of the piezoelectric field to the interlayer exciton of TMDC bilayers which can contribute the net force to the exciton motion. By screening the in-plane filed with the top ITO cladding, the strong acoustic transport of the exciton has been observed that the exciton transport can exceed 20 μm.

4.2 ANALYSIS OF ACOUSTIC WAVE MODULATION

To estimate the effect of the SAW modulation, we simulate the 1 μm wavelength SAW mode on the $LiNbO_3$ substrate. The SAW is propagating along the z-direction which exhibits the largest piezoelectric response. The geometry profile and E_z field distribution are shown in the Figure 4.6 (a) and (b), the periodic E_z field would propagate along with the SAW. With ITO cladding, the in-plane field of the acoustic wave can be effectively suppressed that exciton dissociation will become negligible. Once the exciton is formed, it will be trapped into the potential minimum induced by

the piezoelectric field and then carried by the propagating SAW. As a result, we expect the exciton to propagate with long distance and recombine at a position away from the laser pump spot.

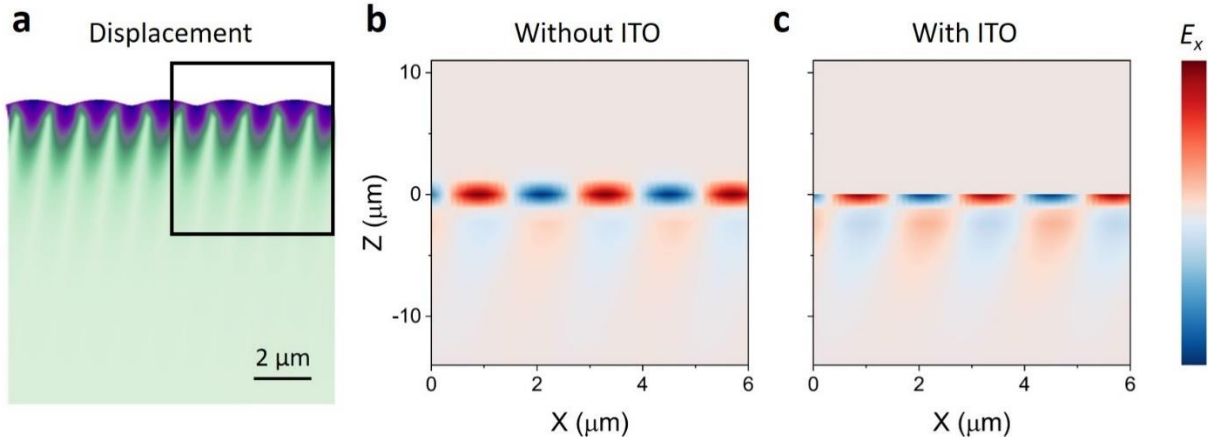

Figure 4.6. The shape and electric profiles of the SAW on the $LiNbO_3$ substrate. a) The geometry profile of the SAW. The SAW is confined along the surface of the $LiNbO_3$ substrate. b) The electric field profiles along the propagation direction. The SAW carries a large perpendicular electric field which can interact with the interlayer exciton devices on the substrate. The periodic E field will create the periodic potential for the interlayer exciton.

Analytically, the 20 mW/μm SAW can achieve the E_z filed about 4.6×10^7 V/m. Considering the perpendicular dipole polarization of the interlayer exciton about $e \times 7.5 \times 10^{-10}$ m, the maximum energy shift δE_{max} induced by the piezoelectric field will be 34.5 meV. With the ITO layer, it can provide an efficient screening of the in-plane field component for the SAW with different acoustic wave wavelengths as shown in table 4.1.

Table 4.2. The simulated piezoelectric field at 10 nm above the $LiNbO_3$ substrate with the top ITO electrode.

Power density: 1 mW/µm

$\lambda\ (\mu m)$	**0.6**	**1.2**	**1.8**	**2.4**	**3**	**3.6**
f (GHz)	5.8568	2.9242	1.9497	1.4626	1.1703	0.97539
E_z ***(V/nm)***	0.082	0.076	0.059	0.048	0.04	0.035
E_x ***(V/nm)***	8.6×10^{-3}	4×10^{-3}	2.1×10^{-3}	1.3×10^{-3}	8.5×10^{-4}	6.1×10^{-4}

As we know, the energy gradient of the exciton can contribute to the force to move the exciton. The resulting force applied on the exciton will be proportional to the gradient of the E_z field.

$$F = \frac{\partial(\delta E)}{\partial x} = ed\frac{\partial E_z}{\partial x} \tag{4.1}$$

With the CW laser excitation, the exciton concentration will reach the equilibrium condition, the dynamics of the exciton diffusion can be described by the equation.

$$D\frac{\partial^2 n}{\partial x^2} + \frac{D}{k_B T}\frac{\partial}{\partial x}\left(n\frac{\partial \phi}{\partial x}\right) + G - \frac{n}{\tau} = \frac{\partial n}{\partial t} \tag{4.2}$$

D is the diffusion coefficient of the exciton, ϕ is the potential of the exciton, *G* corresponds to the potential of the exciton. There are two components that can contribute to the transport of the exciton. The first term is the exciton diffusion term, the exciton will naturally diffuse from the high concentration region to the low concentration region. The net diffusion of the exciton can only happen from high concentration to low concentration, it becomes strong in the high excitation regime. The second term is related to the drift of the exciton under the energy gradient, this effect can be prominent when a large energy gradient is formed. According to the Einstein relation, the $D/(k_B T)$ of the second term is corresponding to the mobility of the electron in the semiconductor model. Considering the exciton moving in the periodic SAW field, the exciton diffusion speed could be estimated:

$$v = \mu_{eff} E_{eff};\ \mu_{eff} = D * \frac{e}{k_B T} \tag{4.3}$$

As result, the exciton would be carried by the acoustic wave. From the analytical calculation, we plot average velocity vs effective mobility.

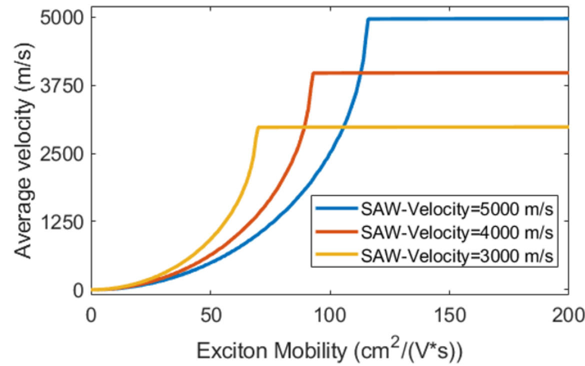

Figure 4.7. The relation between the exciton average velocity and the exciton mobility at different SAW velocities. As you expect, the higher exciton mobility contributes to larger drift velocity. When exciton mobility is large enough, the exciton velocity will be saturated due to the limit of the SAW velocity.

As mentioned in the recent paper, the diffusion coefficient can reach 0.1 cm^2/s at 10 K, which is equivalent to the mobility of more than 100 $cm^2/(V \cdot s)$. As the SAW is applied, the average velocity of the exciton can achieve 3000 m/s as indicated in Figure 4.7. Considering the long lifetime of the interlayer exciton, the lifetime is more than 100 ns. As the consequence, the diffusion length is estimated more than 30 μm that is close to the size of the $MoSe_2/WSe_2$ heterostructure. With enough SAW power, the transport of exciton with a long propagation length is promising.

Here, we demonstrate the long-range and directional transport of IXs in a bilayer WSe_2 using SAW at temperatures up to RT. The IXs in a bilayer WSe_2 are momentum indirect with a long lifetime of up to 10 ns at 10 K and ~1 ns even at RT. It was reported recently that the exciton energy of IXs in bilayer WSe_2 could be modulated by an out-of-plane static field. Consider a bilayer WSe_2 placed directly on a piezoelectric substrate (Figure 4.8 a). SAW is excited and propagates through the area where a bilayer WSe_2 is transferred to. On a piezoelectric substrate

such as $LiNbO_3$, the propagating SAW will generate a near-field piezoelectric field with a large out-of-plane field (E_z) amplitude on the order of 10^7 V/m at 1 mW/μm of acoustic power density. As such, the E_z component will periodically modulate the IX energy in space and time, creating a dynamic trapping potential for the IXs in the extrema of E_z. As the SAW propagates, the IXs will drift along the time-varying gradient of E_z and thus be carried by the SAW—like surfing on a wave—to travel a long distance before they recombine (Figure 4.8 b). With a SAW velocity of ~3.0×10^3 m/s and an exciton population lifetime >10 ns, the IXs can travel >30 μm, an order of magnitude longer than the exciton diffusion length.

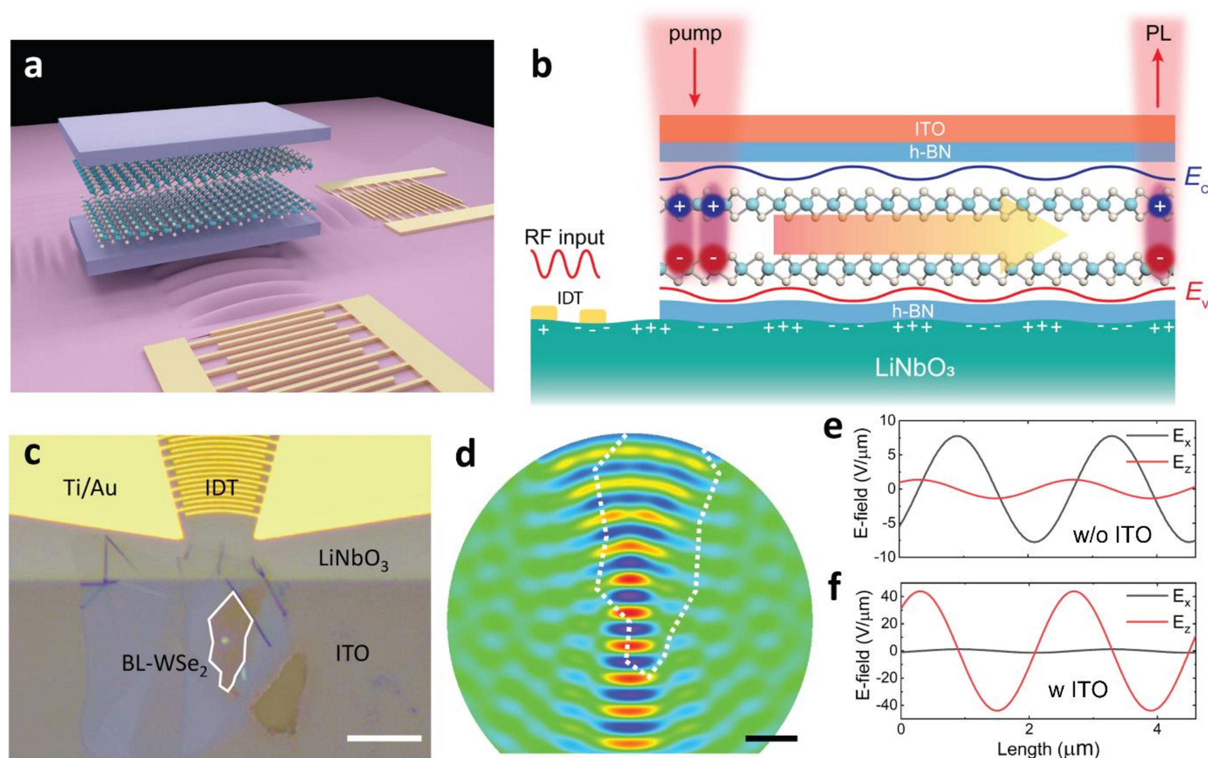

Figure 4.8. Bilayer WSe_2 integrated with SAW devices. a. Schematic illustration of the h-BN encapsulated bilayer WSe_2 stacked with SAW devices. The IDTs generate SAW to transport the excitons in different directions. b. The propagating SAW modulates the energy of the excitons and transports them from the pump spot to the flake edge, where they recombine to generate photoluminescence. For simplicity, we only plot +z interlayer exciton in bilayer WSe_2. See S.I. for

details. c, Optical microscope image of the device, with the white line outlining the bilayer WSe_2. Scale bar, 20 μm. d. The piezoelectric field profile of the SAW generated by the focusing IDT. The acoustic focal point has a waist of 3 μm and is at the edge of the bilayer WSe_2. The dotted line outlines the WSe_2 flake. Scale bar, 5 μm. e-f, The piezoelectric field distribution with (e) and without (f) the top ITO electrode. The field amplitude is calculated assuming an acoustic power density of 1mW/μm. The ITO electrode can efficiently suppress the in-plane piezoelectric field component (E_x), which causes undesirable exciton dissociation.

Figure 4.8 (b) depicts the scenario when a bilayer WSe_2 is under both optical pumping and SAW modulation. Since the bilayer WSe_2 is inversion symmetric, there are two energy degenerate IXs with dipole moment $\boldsymbol{p}$ pointing along the $+z$ and $-z$ directions, respectively. For simplicity, hereon, we use $+z$ IX to explain the transport process. The electric field $E(r,t)$ induced by the SAW modulates the IX energy by $\Delta E = -p \cdot E$ and thus creates a dynamic potential well moving at the acoustic velocity. At low temperatures, the optically excited IXs will quickly relax to the energy minimum created by the SAW in real space and travel with the propagating SAW. Figure 4.8 (c) shows the optical image of our device. We designed a focusing IDT structure that focuses the acoustic wave into the WSe_2 region (Figure 4.8 d) to concentrate the acoustic power density and enhance the piezoelectric field $\boldsymbol{E}$. From the simulated electric field profile of the focused beam of the acoustic wave, it has a waist of ~3.0 μm at the focal point.

The IDT device excites a strong SAW mode at 1.237 GHz with an acoustic wavelength of 2.832 μm, assuming an acoustic velocity of 3.5×10^3 m/s for the z-propagating Rayleigh mode in a y-cut $LiNbO_3$ substrate (see Figure 4.9).

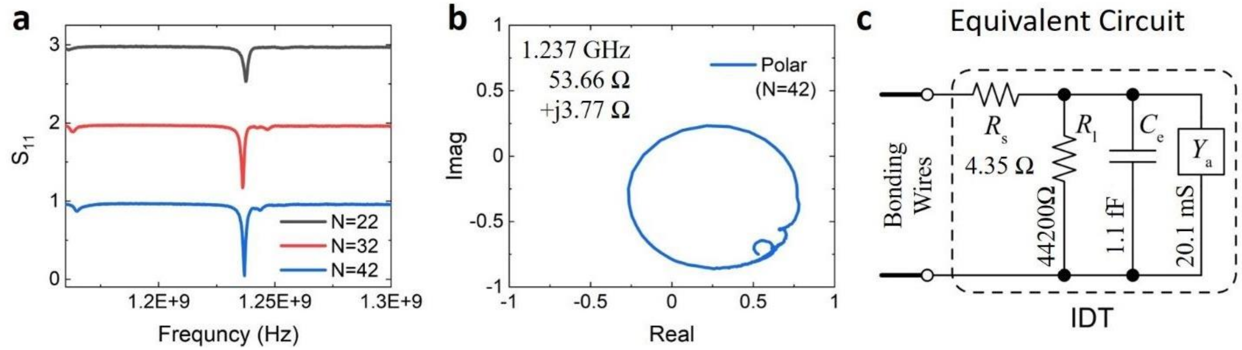

Figure 4.9. RF calibration of the IDT acoustic transducers. (a) RF reflection coefficient S11 measurement of the IDT devices. We test the IDTs with the varied number of periods N. Device with N=42 exhibits the best impedance matching according to the S11 measurements. (b) The vector analysis of the IDT resonance on a polar chart showing a strong acoustic resonance at 1.237 GHz with an on-resonance impedance 53.66 Ω+j3.77 Ω, closely matching the 50 Ω impedance of the RF source. (c) Equivalent circuit model of the IDT acoustic transducer for N=42 with component values of serial resistance R_s, shunt resistance R_l, capacitor Ce and admittance Y_a extracted from the data in (a) and (b).

Here, we also show the circuits model of the IDTs and give the estimate of the impedance for the particular device. The power ratio for different circuits components (Reflection, serial resistance R_s, shunt resistance R_l, and admittance Y_a) is then calculated from the data in Figure 4.9 (a) and (b). By scanning the period, we can make the device near impedance matching. For N=42, the on-resonance conversion efficiency is 91% indicating a strong RF to acoustic wave conversion.

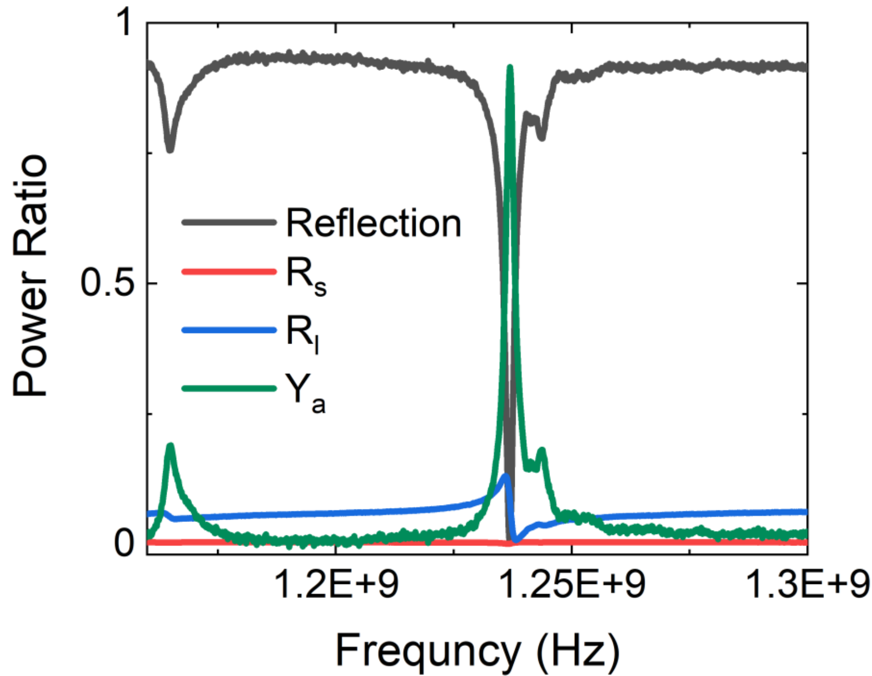

Figure 4.10. The RF power ratio for different circuits components (Reflection, serial resistance Rs, shunt resistance R_{1}, and admittance Y_{a}) calculated from the data in Fig.SI-11 (a) and (b).

To reduce the inhomogeneous broadening and exciton trapping from spatial variation of surface potential, we encapsulated the bilayer WSe_2 with ~10 nm hexagonal boron nitride (h-BN) flakes using the standard pick-up method and transferred onto the $LiNbO_3$ substrate with pre-patterned IDTs. A thin layer of indium-tin-oxide (ITO) was deposited on the heterostructure region as a top transparent electrode. This top electrode plays an important role by efficiently suppressing the in-plane piezoelectric field component (E_x), which may cause exciton dissociation[174], [183], [185], [186] while maintaining a relatively strong out-of-plane field component E_z. The finite-element method (FEM) simulation (Figure 4.8 e, f) compares the piezoelectric fields in the situations of with (Figure 4.8 e) and without (Figure 4.8 f) the top ITO layer, showing that the ITO layer suppresses E_x by about two orders of magnitude.

4.3 DEVICE FABRICATION AND MEASUREMENT SCHEMES

4.3.1 *Device Fabrication*

The WSe_2 device was fabricated by the standard polymer-assisted (PC) pick-up method[187], [188]. The 2D flakes of hBN and WSe_2 (HQ graphene) were exfoliated to a 90 nm SiO_2/ Si substrate and then picked up using PC/PDMS (Sylgard 184) stamps. The bilayer WSe_2 flakes were identified by their optical contrast and then confirmed with photoluminescent measurements. The IDTs were patterned on a y-cut $LiNbO_3$ wafer (MTI) using ebeam lithography. The IDT is aligned to generate SAW propagating along the z-axis of the $LiNbO_3$ wafer. Layers of 12 nm chromium and 120 nm gold were deposited using an ebeam evaporator under a high vacuum. The aligned transfer was then done by a home-built transfer stage with high accuracy so that the WSe_2/hBN heterostructure was precisely aligned at the focus region of the curved IDTs. PC residue was then removed using chloroform for 1 h and followed by a 5 min rinsing in the IPA. Finally, aligned ebeam writing was performed and 50 nm indium-tin-oxide (ITO) was deposited by a sputtering system (Evatec LLS EVO) under O_2 conditions. After deposition, the device was annealed in the atmosphere at 300 °C for 5 min to improve the conductivity of the ITO film, which can ensure a better screening of the in-plane field.

4.3.2 *Measurement setup*

A continuous-wave He-Ne laser (633 nm) was used to excite the excitons in bilayer WSe_2. With an objective lens (NA=0.42), the laser beam was focused with a diffraction-limited spot size of about 1 µm. The sample was mounted in a cryostat (Montana Instrument) with an optical window for optical access. Meanwhile, the RF signal was generated by a vector network analyzer (VNA) (Agilent E8362B) and then coupled to the wire-bonded device inside the cryostat. The calibration

kits (Keysight 8052D) were used to de-embed the system so that the IDT resonance can be resolved.

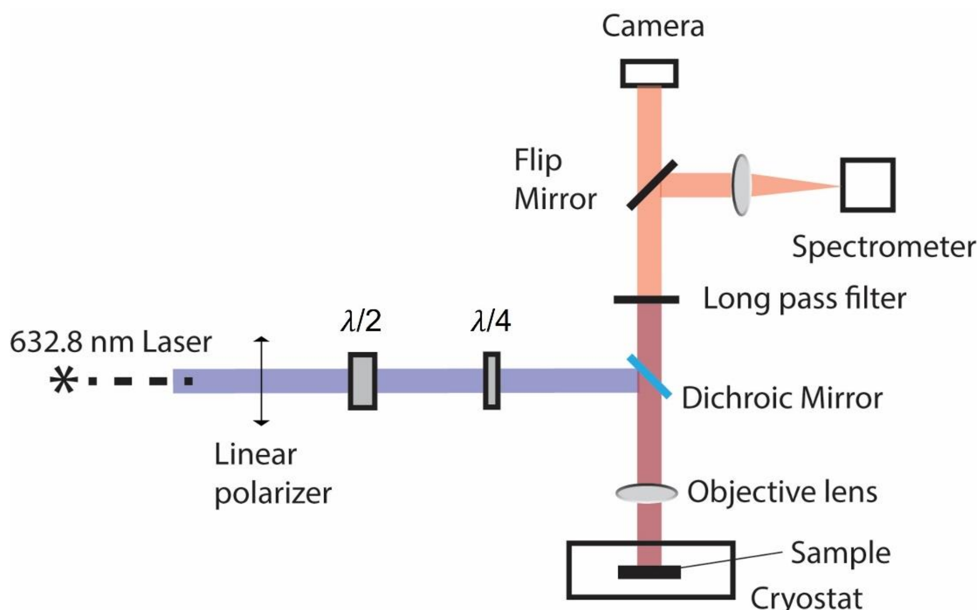

Figure 4.11. The measurement setup for the exciton transport. The device is measured in the cryostat from 6 K to RT with the RF capability.

The interlayer exciton emission was acquired with a spectrometer (Princeton Instrument) after the laser line was removed with a 633 notch filter (Thorlabs). To image the spatial transport of the exciton, the center wavelength of the spectrometer was set to be 0 so it functioned as a mirror. The filtered signal was then collected by a cooled camera (Pixis 400) operating at -70 °C to improve the signal-to-noise ratio. To collect the spectrum results, we set the center wavelength to 790 nm, which covered the emission spectrum of the interlayer exciton. To perform the spectral-PL imaging measurement of the exciton transport, the transport direction was aligned with the slit of the spectrometer, while the x-axis of the CCD camera displayed the spectrum information. The y-axis signal gave the spatial emission of the bilayer devices.

4.4 TRANSPORT OF 2D EXCITON AT 100 K

We first demonstrate efficient SAW transport of IXs by performing spatially resolved photoluminescence (PL) measurement. Without SAW and at a low pump power, the diffusive IX flux density can be described by the diffusion equation: $j = -D\nabla N$, where D is the temperature-dependent diffusion coefficient and N is the exciton density (inset, Fig. 1a). Due to the low D in TMDC, the IX diffusion is relatively weak. In comparison, when SAW is turned on, the IX population is strongly modulated by the piezoelectric field and drifts along the SAW propagation direction (inset, Fig. 2b). As the velocity of the SAW (~3,500 m/s) is much lower than the thermal velocity of excitons (10^4 – 10^5 m/s in our experimental condition, see S.I.), the IXs can be treated as an exciton gas in quasi-equilibrium. With sufficiently high SAW amplitude, the IX gas will be trapped in the energy minimum of SAW and drift with a center-of-mass velocity identical to the SAW velocity.

Figure 4.12 (a) and (b) compare the PL images measured at 100 K with SAW off and on, respectively. The IXs were excited with a He-Ne laser at 633 nm, having a power of P_p=20 μW, and focused to a diffraction-limited spot size of 1 μm. The excitation spot is placed near the edge of the WSe_2 flake close to the IDT and in the middle of the acoustic wave beam (Figure 4.8 d). Without SAW (Figure 4.12 a), the IXs diffuse by only 1-2 μm, consistent with previous measurement results. When SAW is turned on with power P_s=6 mW, as shown in Figure 4.12 (b), we observe strong exciton emission at two spots on the far edge of the WSe_2 flake, along the SAW propagation direction and ~20 μm away from the pump spot. The two separate emission spots are at the corners (one convex and one concave) of the flake edge, where the acoustic wave is most focused (Figure 4.12 d). The IXs are transported at the acoustic velocity of 3,500 m/s so the traveling time is less than 6 ns, shorter than their lifetime. The results reveal SAW-driven transport

of IXs over a device size limited distance, setting a lower bound of the propagation length to ~20 μm.

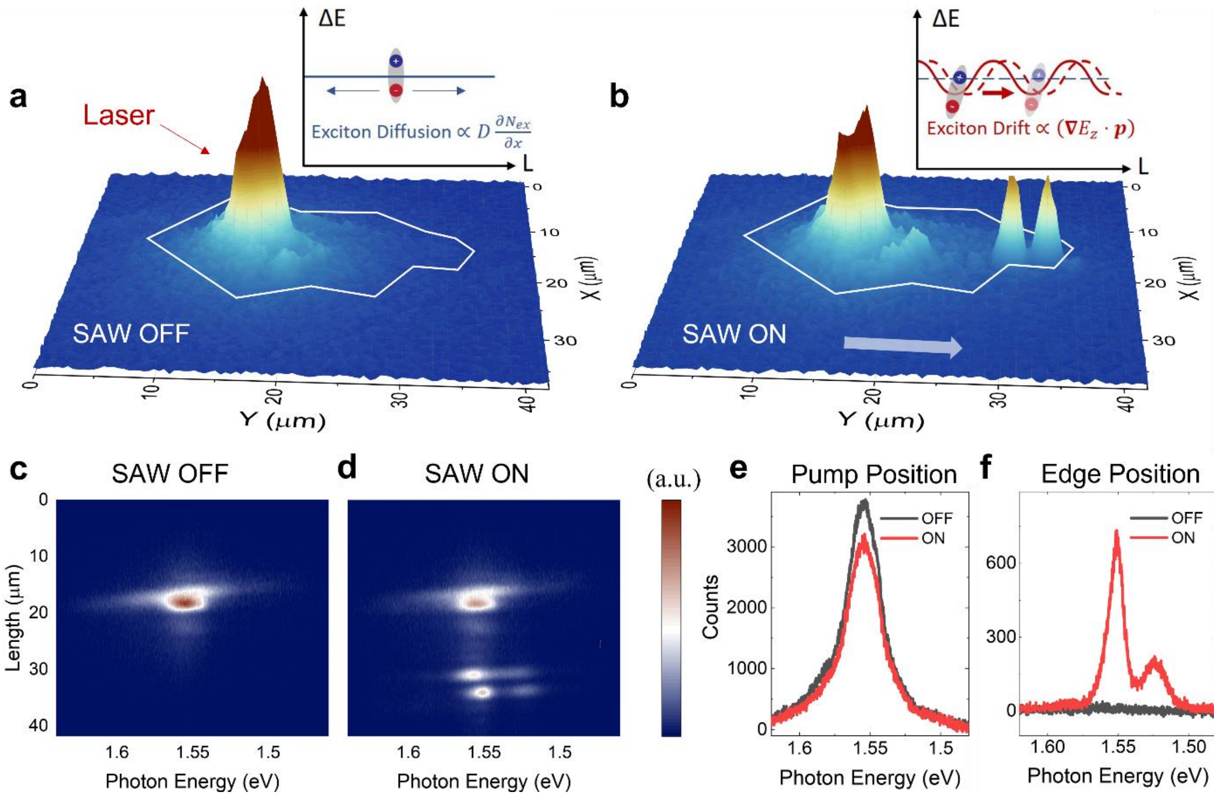

Figure 4.12. SAW-driven transport of IXs at 100 K. a-b, Real-space PL mapping (a), when SAW is off, and (b) when SAW is on with 6 mW power. Two bright emission spots appear at the edge of the flake and the focal point of the acoustic wave (see Figure 4.8 d) due to the SAW-driven transport of IXs. Insets: Illustration of free diffusion and SAW-driven drift of IXs. c-d, The spectral PL image at the same experimental conditions as a-b. The non-local exciton emission at the flake edge is clearly attributed to the IXs in WSe_2, which have an emission peak at 1.56 eV. e, The emission spectrum at the pump position slightly decreases when SAW is turned on. f, The emission spectrum at the flake edge position drastically increases when SAW is turned on.

To confirm the transport is indeed from IXs, we performed spatial and energy-resolved measurements. We aligned the slit of the spectrometer with the SAW propagation direction (y-axis) and acquired spectral PL images with SAW off and on. The emission of the transported IXs

is predominantly at the energy around 1.56 eV, which agrees with the IX energy of bilayer WSe_2. The result is consistent with our expectation that only IXs with perpendicular dipole moment are efficiently transported by SAW. At the pump spot (Figure 4.12 e), the IX emission slightly decreases when SAW is turned on, presumably due to the removal of IXs by the SAW. In contrast, at the far edge of the flake (Figure 4.12 f), the application of SAW increased the IX emission intensity by more than two orders of magnitude. In control devices without the top ITO layer, no IX emission (see Figure 4.13) can be observed beyond the IX diffusion distance.

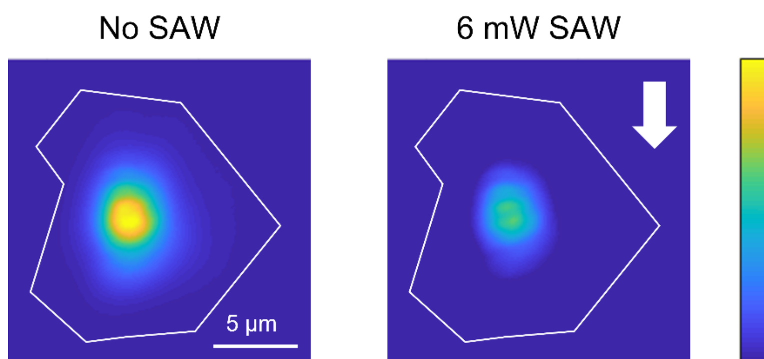

Figure 4.13. SAW modulation of the control devices that do not have the top ITO to screen the in-plane piezoelectric field. No transport of IXs beyond the diffusion distance can be observed. Rather, the SAW piezoelectric field dissociates the IXs to free carriers to suppress the emission everywhere.

It agrees with the expectation that the in-plane piezoelectric field, if not screened by the ITO (Figure 4.8 e), will dissociate the IXs to free carriers. These free carriers will have a very low recombination rate in the SAW because they are spatially separated by half the acoustic wavelength (~1.4 μm in our device). Therefore, we can confirm that the emission at the edge of the flake is from SAW transported IXs.

4.5 POWER DEPENDENT EXCITON TRANSPORT AT 100 K

We next characterize the IX transport at different SAW powers P_s. We find that the transported exciton density increases monotonically with the SAW power, but the trend is highly nonlinear with an activation behavior. For $P_s < 3.0$ mW, the IX transport is negligible, and the IX emission is localized near the laser excitation spot (Figure 4.14 a). When P_s increases to 4.5 mW, two emission spots appear at the flake edge (Figure 4.14 b), suggesting activation of the transport process. When P_s is further increased to 6 mW, the exciton transport becomes so efficient that the emission intensity at the flake edge is already comparable to that at the pump spot (Figure 4.14 c).

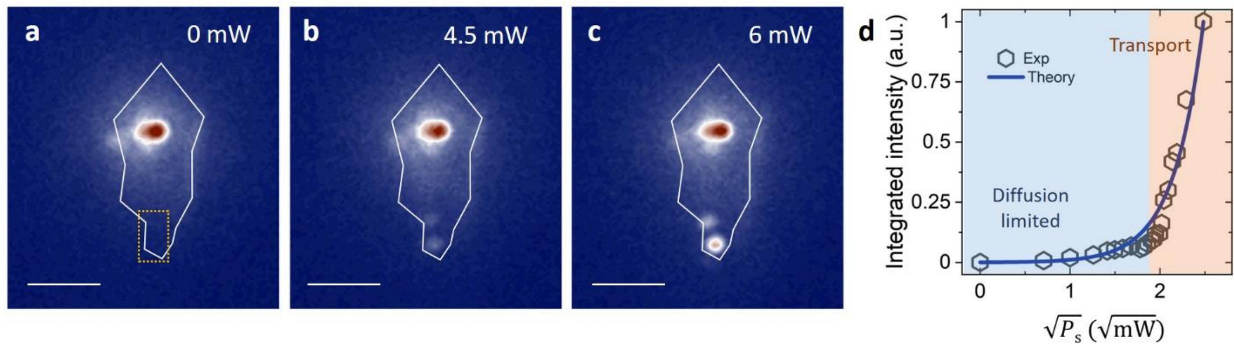

Figure 4.14. Acoustic power-dependent IX transport at 100 K. a-c PL images at different SAW power P_s of (a) 0 mW, (b) 4.5 mW, (c) 6 mW. The solid white line outlines the WSe_2 flake. The two bright emission spots at the edge of the WSe_2 flake highlight the SAW-driven transport of IXs. Scale bar, 10µm. d, The integrated emission intensity at the flake edge (in the area indicated by the yellow dashed box in a) depending on the SAW power P_s. The experimental data are fitted with the theoretical model that the transport exciton density exponentially depends on the square root of P_s. At low P_s, the exciton transport is diffusion-limited (blue shaded). A high P_s, SAW-driven transport is activated (red shaded).

Figure 4.14 (d) plots the integrated emission intensity at the flake edge, which is proportional to the transported exciton density n_T, as a function of P_s. The experimental result agrees with our theoretical model of SAW activated transport in which the transported exciton density n_T is

proportional to $e^{\sqrt{\frac{P_s}{P_t}}}$ at a given temperature. Fitting the result at 100 K gives a relatively small threshold power of P_t ~ 0.1 mW, beyond which exciton transport is activated by the SAW. Similar exponential behavior and power law have also been observed in coupled GaAs quantum wells[180], where exciton transport is impeded by disorder and defect-induced potential variations at the low SAW power limit. In TMDC such as bilayer WSe_2, the intrinsic defect density can be >7.0 $\times 10^{10}$ cm^{-2}[189], along with the strain-induced potential variation caused by the transfer process. For efficient IX transport to happen, the SAW modulation of IX energy ΔE needs to overcome the defect and strain induced potential variation, and the efficiency of exciton transport is sensitive to the material quality.

Besides scanning the acoustic power, we are also interested in the exciton phenomena under different optical pump power. As shown in figure 4.15, The portion of the transported exciton decreases with a higher optical pump.

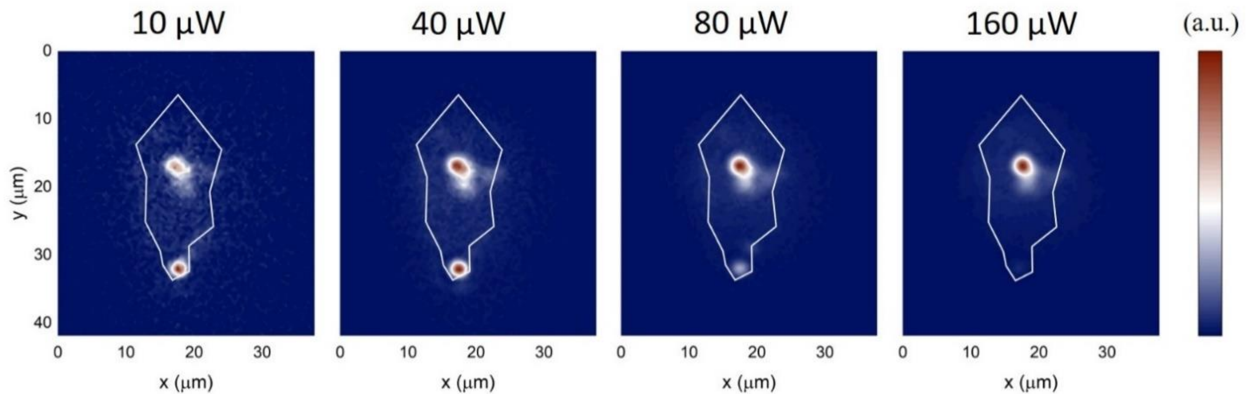

Figure 4.15. Optical power-dependent measurement of exciton transport at 100 K with 6 mW SAW power.

Under high power excitation, the exciton can reach the plasma regime in the bilayer TMDCs. The high density of excitons could screen the piezoelectric field of SAW and reduce the acoustic modulation of the exciton energy[190].

4.6 THEORY OF EXCITON TRANSPORT DRIVEN BY SURFACE ACOUSTIC WAVES

In the IXs of bilayer WSe_2, the bound electrons and holes live, respectively, in the Q (also called Λ in literature) and the K valleys of the Brillouin zone. Due to the spin-valley locking of bilayer WSe_2, the dipole moment of an IX can point along the +z or -z directions, depending on the layer localization of the electron and the hole in the IX. Under the periodic out-of-plane electric field induced by the SAW, the two types of IXs with opposite dipoles are driven to two nearby field extrema separated by half acoustic wavelength and propagate together in the same direction.

In the temperature range of 6 K – 300 K, excitons have an average kinetic energy of 0.6 meV – 26 meV. Taking the effective mass of an exciton to be ~ m_e (bare electron mass), the thermal velocity v_{IX} of the exciton is in the range of $1.5 \times 10^4 - 9.6 \times 10^4$ m/s. This value is an order of magnitude larger than the traveling velocity of SAW (~3.5×10^3 m/s). As a result, the IX ensemble can be approximated as an exciton gas under quasi-equilibrium, when it is trapped at the minima of the slowly-varying potential energy landscape. Here the trap can arise either from disorder or from the electric field gradient induced by SAW.

We next model the transport of excitons in the realistic bilayer WSe_2 device, assuming that the excitons do not recombine during the transport. The surface potential disorder caused by strain and other imperfections is described by potential wells that can trap excitons (Figure 4.16a), with a characteristic barrier height of Δ and length L. If L is much smaller than the wavelength of the SAW, the electric field gradient of SAW can help the excitons to overcome these potential barriers. An exciton that is not localized by the disorder should have kinetic energy larger than $E_{min} = \Delta - (\nabla E_{z-max} \cdot \mathbf{p})L$ (Figure 4.16 b) to overcome the barrier, where ∇E_{z-max} refers to the maximum

gradient of the electric field induced by the SAW. Under quasi-equilibrium, the population n of these excitons:

$$n(\nabla E_{z-max}, T) \int_{E_{min}}^{\infty} dE e^{-\frac{E-\mu}{k_B T}} \cdot e^{\frac{Lp}{k_B T}\nabla E_{z-max}} \tag{4.4}$$

The density of states factor is taken as a step function for 2D excitons.

At 100K, the PL intensity at the edge of the bilayer WSe_2 flake should be proportional to n. As the maximum electric field gradient induced by SAW is proportional to the square root of SAW power $\nabla E_{z-max} \sim \sqrt{P_s}$, we fit the PL intensity with $n(P_s) = n_0 e^{\sqrt{\frac{P_s}{P_t}}}$, where P_t is a temperature and sample-quality dependent factor, above which the exciton can respond efficiently to the electric field generated by SAW. Figure 4.16 (c) shows this exponential dependence is consistent with experimental observations.

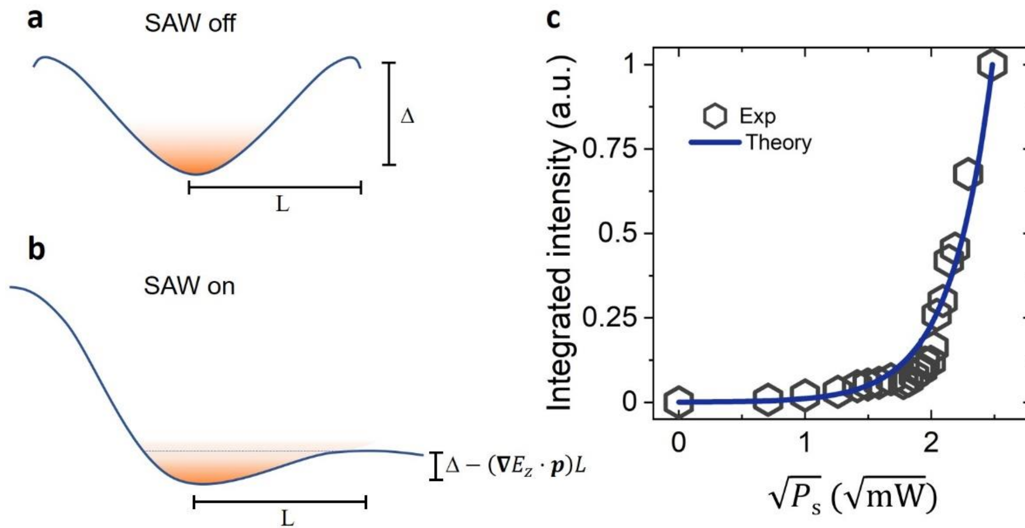

Figure 4.16. Exciton transport by surface acoustic wave under disorder potential. (a) Schematic exciton gas in a trap with a characteristic depth in energy of Δ and length L. The exciton gas in quasi-equilibrium is shown in orange. (b) Schematic exciton gas when maximum electric potential gradient from SAW is applied, creating a shallower potential barrier on one side of the trap. The exciton population above the dotted line can travel with SAW. (c) Fitting the power-dependent PL intensity to the SAW power.

4.7 Temperature-dependent exciton transport

The activation behavior motivates us to further measure SAW-driven IX transport at different temperatures. Figure 4.17 shows the spectral PL mapping at temperatures from 6 K to 200 K with fixed pump power P_p=20 μW and SAW power P_s = 6 mW. In this wide temperature range, we observe rich features showing the roles of exciton localization, SAW-driven transport, and recombination and phonon scattering. Note that the measurement at each temperature is normalized to its respective maxima for clarity. At 6 K and with SAW off, the emission spectrum shows a series of sharp resonances (Figure 4.17 a), which are attributed to defect emission and phonon-assisted recombination of the IXs. When SAW is on, the sharp resonances disappear, and the emission intensity decreases significantly (Figure 4.17 b and Appendix). Meanwhile, IX transport at this low temperature is very weak. The suppression of IX emission can be explained by that the SAW reduces the coupling between excitons and recombination centers such as defects. When the temperature increases to 30 K, the sharp exciton resonances disappear (Figure 4.17 c). At this elevated temperature range, the excitons are thermalized into exciton gas, leading to weaker couplings with the local defects. As a result, the SAW-driven transport starts to make the PL at the flake's edge observable (Figure 4.17 d). When the temperature reaches 100 K, the IX emission becomes more than two times brighter at the pump spot (Figure 4.17 e) than at 30 K. This is because indirect IX recombination becomes more efficient when the thermal phonon density is high. The SAW-driven transport is also the most prominent at this temperature (Figure 4.17 f) because the defects and disorders have a less trapping effect on the thermalized excitons and the exciton population lifetime is still sufficiently long. At 200 K (above the Debye temperature), the thermal phonon population is high. As a result, IX emission has a broad spectrum and high

intensity without SAW (Figure 4.17 g). However, the IX transport is impeded due to strong exciton-phonon scattering and decreased exciton population lifetime (Figure 4.17 h).

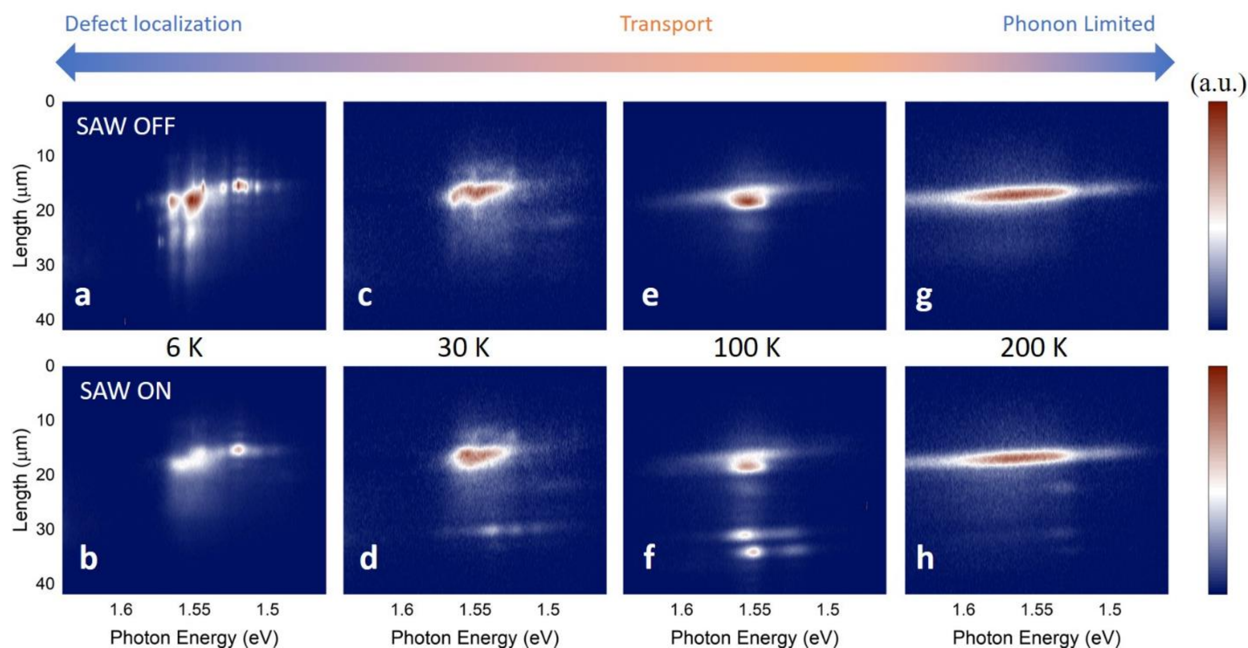

Figure 4.17. SAW-driven IX transport at varying temperatures. The spectral PL image of exciton transport at 6-200 K with SAW off (a, c, e, g) and on (b, d, f, h). For clarity, the data at each temperature is normalized separately. a, b, At low temperature (6K), IXs show narrow peaks as they are highly localized to recombination centers such as defects or couple strongly to local vibrational modes. SAW can delocalize the IXs so to suppress the emission. However, the transported IXs remain dark because of the reduced phonon-assisted recombination at low temperatures. c, d, At elevated temperatures (30 K), the IXs are thermalized with broad emission. SAW transport turns on with visible emission at the flake edge. e, f, At 100 K, SAW transport of IXs is most prominent as IXs have a sufficiently long lifetime and are less susceptible to defect trapping. G, h, At even higher temperatures, SAW transport, although still visible, is inefficient as exciton-phonon scattering dominates and the IX population lifetime is short.

Overall, our systematic measurements have revealed three regimes of IX behaviors and the transition between them. At the lowest temperatures, the IXs are highly localized and their transport is diffusion-limited. At intermediate temperatures, the IXs are bright with phonon-

assisted recombination. At the same time, they still have a long lifetime, allowing for efficient SAW-driven transport over a long distance.

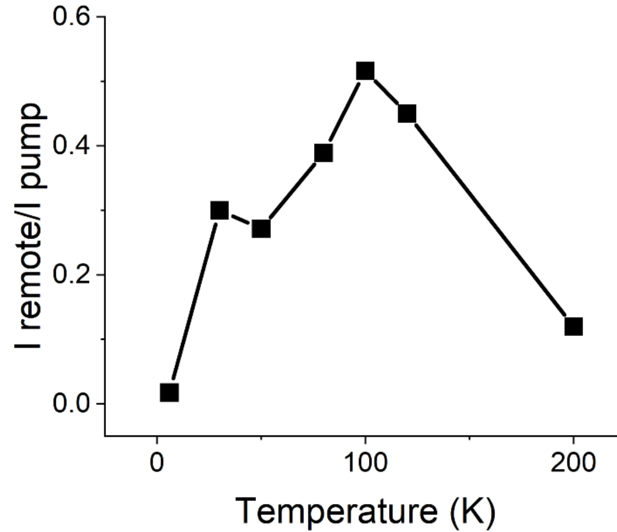

Figure 4.18. Evaluation of the exciton transport at different temperatures. The exciton emission at the edge is normalized to the emission intensity at the pump center. The exciton transport reaches the maximum at 100 K.

At further elevated temperatures, strong phonon scattering decreases exciton mobility and lifetime, preventing efficient transport. Nevertheless, thanks to the strong SAW modulation, even at room temperature, we still observe a SAW-driven transport distance of ~2.0 μm (see Figure 4.19).

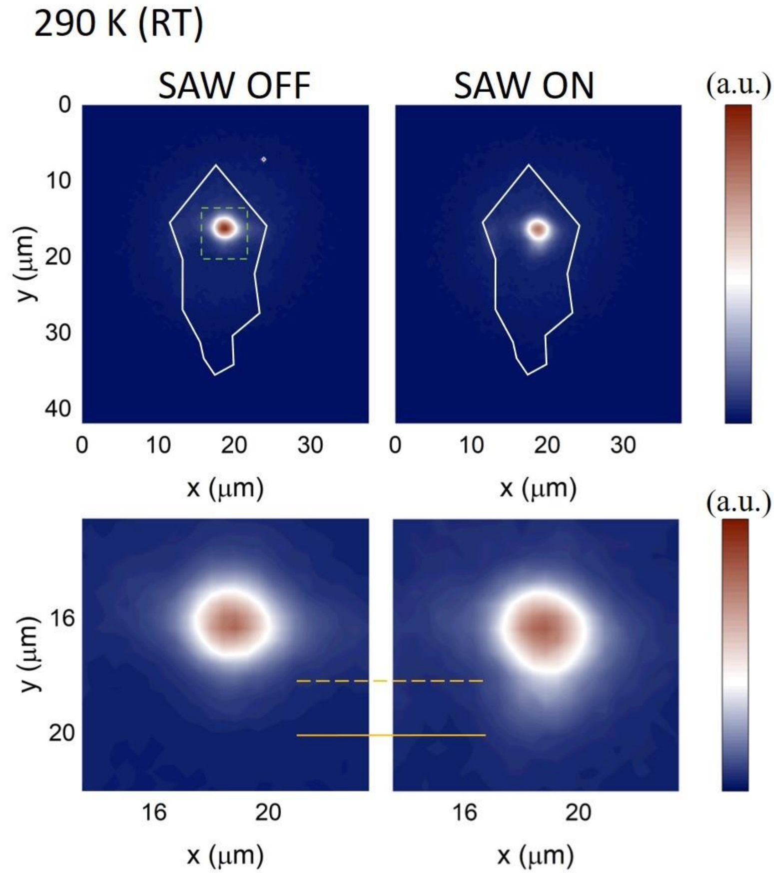

Figure 4.19. Exciton transport at 290 K. The lower panels are zoomed in view of the dashed box. The exciton transport over ~2 μm can still be observed at room temperature owing to the strong SAW modulation.

4.8 Conclusion and outlook

In conclusion, we have demonstrated that SAW is an efficient, contact-free approach to transport IXs in bilayer WSe_2 over a distance far beyond the diffusion length. The SAW-driven transport happens when the SAW modulation of IX energy can overcome the local potential variation and defect traps. Since the transport distance depends on the exciton lifetime of the optically active material and the acoustic velocity of the substrate, using TMDCs with longer lifetimes and piezoelectric substrate with higher acoustic velocity can lead to a much longer transport distance. The contact-free transport driven by the acoustic wave that is launched remotely also preserves the

high quality of the materials and prevents undesired effects induced by local gates. Although the maximal transport distance is reached at the temperature of 100 K in the current device, further improvement of the material quality and interface cleanness will make the efficient room-temperature operation possible. We note that SAW is a universal approach to control excitons with both its piezoelectric field and strain field can be utilized to manipulate and transport excitons in many other 2D material systems. SAW can also be guided and circulated in phononic circuits and resonators, which will afford rich functionality and flexibility.

Chapter 5. CONCLUSION AND OUTLOOK

5.1 SUMMARY OF THIS THESIS

2D semiconductors show remarkable optoelectronic properties, they are considered as the outstanding candidate for the applications of photodetectors, modulators, and novel optoelectronic devices. The high responsivity, broad optical-spectrum range, and effective field modulation make 2D materials distinct from the traditional bulk materials. Contrary to the bulk materials, 2D materials can be simply stacked onto any arbitrary substrates by the standard transfer techniques owing to the nature of the Van der Waals interaction. The fabrication of the 2D devices does not suffer any lattice mismatch which usually limits the integration of bulk materials. Up to now, there are enormous demonstrations of 2D optoelectronic devices including light-emitting diodes, photodetectors, and modulators which show improved performance compared to the commercial devices based on bulk materials. Recently, the development of the wafer-scale growth of 2D materials facilitates the application for large-scale electronics, sensors which contribute to the study of integrated circuits, artificial intelligence, and edge computing. The advantages of edge computing have also urged the development of novel optoelectronic edge sensors that combine vision-sensory and computational functionalities in the same devices, which recently have been demonstrated using TMDCs and bP for broadband spectral imaging. Based on the progress of the 2D optoelectronics, it will be very interesting to further extend the functionalities of the 2D devices and explore the novel physical platforms to study the optoelectronic properties of the 2D materials. In chapter 2, we studied the field modulation of the absorption in few-layer bP. We have resolved the transitions between the same and different band indices which show strong layer dependence. The main results of the electro-optical modulation were measured from the 9 nm bP device which has modulation resonances at the mid-IR region with the modulation depth of 5%. The direct band

transitions E_{11}, E_{22}, and hybrid band transitions such as E_{12}, E_{21}, have shown opposite modulation signs under the influence of the gate voltage. The modulation effects have also been calculated by the quasi-1D tight-binding model which shows strong agreement with the measurements results. The results of gate modulation provide insights for future applications of bP as the optical modulators in the mid-IR region.

In chapter 3, we analyzed the modulation results measured in chapter 2 by the transfer matrix method. The extinction coefficient of few-layer bP has been extracted for different gate voltages. We then simulated the integration of bP with Si waveguide structures. By considering the anisotropic properties of bP, the alignment of the optical mode and bP crystal orientation has been optimized to achieve the maximum modulation depth in the bP device. The simulated results have shown that 5 dB modulation depth with less than 1 dB insertion loss can be achieved with 120 μm interaction length. For the experiment, we fabricated the on-chip integrated bP devices with Si as the back gate to control the bP absorption. The integrated devices have performed as both photodetectors and modulators in the mid-IR region. We have demonstrated the responsivity of 3 mA/W as the photodetector, and a modulation depth of 8 dB/mm as the modulator.

In chapter 4, we have demonstrated an excitonic transistor based on the interlayer exciton of the TMDC bilayers. The perpendicular dipole moment of the interlayer exciton can couple with the vertical electric field. To achieve the exciton transport, we developed the surface acoustic wave approach which can induce the periodic modulation of the interlayer exciton energy owing to the piezoelectric response of the $LiNbO_3$ substrate. As result, the record long exciton transport has been demonstrated with the propagation length up to 20 μm. Also, we systematically studied the power and temperature dependence of the exciton transport which have shown a clear transition from localization to transport. With the strong modulation of the interlayer exciton, the room

temperature operation of the excitonic transistors has been realized with the transport of 2 μm. The discovery of acoustic transport of 2D excitons has paved the way for studying the exciton behaviors such as the exciton valley hall effect. The SAW technique can also be applied to a similar system including Moire exciton in $MoSe_2/WSe_2$ heterobilayer.

5.2 FUTURE PERSPECTIVES

With the growing interest in 2D optoelectronics, significant improvements in device performance and operation stability have been achieved in material growth and device fabrication. With the high quality and clean material processing, the optoelectronic properties of the 2D materials are well maintained which have potential and importance in developing the next generation of optoelectronic devices. In this section, I will discuss the difficulties for the commercial applications of 2D devices and highlight the future directions which might be important to the 2D research community. Also, I am going to discuss how the techniques developed in our paper can contribute to the research field beyond 2D materials.

As for the bP devices, there are many issues with the materials for real applications. On the one hand, bP is quite air-sensitive and degrade fast under ambient conditions[70], [130]–[133]. On the other hand, the growth of the large-scale bP film is quite challenging. Many efforts have been done to passivate the materials of the surface to extend the device lifetime. Our group has collaborated with Alexandra's group at UW chemistry to develop the approach of the Lewis acid to passivate the surface and extend the lifetime to several days without obvious degradation of the electrical and optical properties[136]. For the device application, more strict requirements for stability are required which need the collaboration between the device Physics and Chemistry group to study the bP reaction inside the atmosphere. Recently, significant progress has been done by the USTC group to achieve the wafer-scale growth of the bP film with uniform thickness and consistent

performance[191]. However, the bP film so far has more defects level compared to the freshly exfoliated flakes where the performance can still be improved. The development of both material growth and passivation is urgently required for large-scale optoelectronic circuits.

Remarkable progress has been done in developing the circuit-level TMDC devices[192], [193]. However, the films have suffered the high defect density and large device-to-device variations which urge the development of more advanced growth techniques. As for the interests in the TMDC exciton, there are enormous reports on the valley effect of the 2D exciton and the prediction of the exciton valley hall effect. They require long-distance exciton transport to observe the small valley hall angle of the 2D excitons. As proved in our SAW devices that more than 20 μm transport has been observed, our SAW approach offers a novel platform to study the transport behaviors of the valley excitons. With the growing interest in the Moire bilayer devices, we can utilize the SAW techniques to study the competition between the oscillating acoustic field and the periodic Moire potential. Both strain and field effects can influence the local Moire potential which can be the future direction of our SAW project.

Also, we noticed that the technology developed for 2D device fabrication can also be applied to other physical systems. For example, people also apply the dry transfer and pick-up techniques of 2D flakes to other bulk samples that they made the photonic crystal cavity and transferred to the diamond for the quantum applications. Also, the 2D materials and their heterostructures provide a simple platform to verify the theory developed in condensed matter physics that many interesting topological and superconducting phenomena have been demonstrated. More importantly, the acoustic approach we developed for exciton transport can also be utilized for other purposes. For instance, we can couple the acoustic wave to the color centers that the quantum states of defect can be precisely controlled.

In summary, we aim for the improving stability and scale of bP devices as the future direction for optoelectronic applications[194], [195]. The devices based on a bP array can enable edge computing and motion camera. The demonstrated multispectral infrared imaging and in-sensor computing with the black phosphorous optoelectronic sensor array can be scaled up to build a more complex visionary neural network, which will find many promising applications for distributed and remote multispectral sensing. As for the excitonic devices, we propose to use the acoustic wave to modulate the Moire exciton in $MoSe_2$ and WSe_2 which have the vertical dipole moment, and maintain the valley information simultaneously[170], [171], [196]. It will be very interesting to observe the acoustic modulation of the Moire potentials and demonstrate the exciton valley hall effect in the Moire bilayer devices. Therefore, there are plenty of rooms and possibilities for the exploration and future impact of these 2D optoelectronic devices.

BIBLIOGRAPHY

[1] N. D. M. Neil W. Ashcroft, *Solid State Physics*. 1976.

[2] R. Shankar, *Principles of quantum mechanics*. Springer Science & Business Media, 2013.

[3] K. K. N. Sze, Simon M., Yiming Li, *Physics of semiconductor devices*. John wiley & sons, 2021.

[4] Antonio Arnau Vives, *Piezoelectric Transducers and Applications*. Berlin: Springer, 2004.

[5] E. P. Ippen and R. H. Stolen, "Stimulated Brillouin scattering in optical fibers," *Appl. Phys. Lett.*, vol. 21, no. 11, pp. 539–541, 1972.

[6] T. L. Avouris, Phaedon, Tony F. Heinz, *2D materials*. Cambridge University Press, 2017.

[7] Z. Sun, A. Martinez, and F. Wang, "Optical modulators with 2D layered materials," *Nature Photonics*, vol. 10, no. 4. pp. 227–238, 2016.

[8] F. Xia, H. Wang, D. Xiao, M. Dubey, and A. Ramasubramaniam, "Two-dimensional material nanophotonics," *Nat. Photonics*, vol. 8, no. 12, pp. 899–907, 2014.

[9] A. Krasnok, S. Lepeshov, and A. Alú, "Nanophotonics with 2D transition metal dichalcogenides [Invited]," *Opt. Express*, vol. 26, no. 12, p. 15972, 2018.

[10] K. F. Mak and J. Shan, "Photonics and optoelectronics of 2D semiconductor transition metal dichalcogenides," *Nat. Photonics*, vol. 10, no. 4, pp. 216–226, 2016, [Online]. Available: http://dx.doi.org/10.1038/nphoton.2015.282.

[11] H. Yu, X. Cui, X. Xu, and W. Yao, "Valley excitons in two-dimensional semiconductors," *National Science Review*, vol. 2, no. 1. pp. 57–70, 2015.

[12] J. Xiao, M. Zhao, Y. Wang, and X. Zhang, "Excitons in atomically thin 2D semiconductors and their applications," *Nanophotonics*, vol. 6, no. 6, pp. 1309–1328, 2017.

[13] B. Zhu, X. Chen, and X. Cui, "Exciton binding energy of monolayer WS2," *Sci. Rep.*, vol. 5, p. 9218, 2015.

[14] H. Liu, Y. Li, Y. S. You, S. Ghimire, T. F. Heinz, and D. A. Reis, “High-harmonic generation from an atomically thin semiconductor,” *Nat. Phys.*, vol. 13, no. 3, pp. 262–265, 2017.

[15] Y. Ye *et al.*, “Monolayer excitonic laser,” *Nat. Photonics*, vol. 9, no. 11, pp. 733–737, 2015.

[16] S. Wu *et al.*, “Monolayer semiconductor nanocavity lasers with ultralow thresholds,” *Nature*, vol. 520, no. 7545, pp. 69–72, 2015.

[17] Y. Liu *et al.*, “Room temperature nanocavity laser with interlayer excitons in 2D heterostructures,” *Sci. Adv.*, vol. 5, no. 4, p. eaav4506, 2019.

[18] W. Liu *et al.*, “Strong Exciton-Plasmon Coupling in MoS2 Coupled with Plasmonic Lattice,” *Nano Lett.*, vol. 16, no. 2, pp. 1262–1269, 2016.

[19] F. Barachati *et al.*, “Interacting polariton fluids in a monolayer of tungsten disulfide,” *Nat. Nanotechnol.*, vol. 13, no. 10, pp. 906–909, 2018, [Online]. Available: http://dx.doi.org/10.1038/s41565-018-0219-7.

[20] J. Cuadra, D. G. Baranov, M. Wersäll, R. Verre, T. J. Antosiewicz, and T. Shegai, “Observation of Tunable Charged Exciton Polaritons in Hybrid Monolayer WS2-Plasmonic Nanoantenna System,” *Nano Lett.*, vol. 18, no. 3, pp. 1777–1785, 2018.

[21] J. B. Khurgin, “Two-dimensional exciton–polariton—light guiding by transition metal dichalcogenide monolayers,” *Optica*, vol. 2, no. 8, p. 740, 2015.

[22] X. Liu, W. Bao, Q. Li, C. Ropp, Y. Wang, and X. Zhang, “Control of Coherently Coupled Exciton Polaritons in Monolayer Tungsten Disulphide,” *Phys. Rev. Lett.*, vol. 119, no. 2, 2017.

[23] W. Liu *et al.*, “Observation and Active Control of a Collective Polariton Mode and Polaritonic Band Gap in Few-Layer WS2 Strongly Coupled with Plasmonic Lattices,” *Nano Lett.*, vol. 20, no. 1, pp. 790–798, 2020.

[24] J. Gu, B. Chakraborty, M. Khatoniar, and V. M. Menon, “A room-temperature polariton light-emitting diode based on monolayer WS2,” *Nat. Nanotechnol.*, vol. 14, no. 11, pp. 1024–1028, 2019, [Online]. Available: http://arxiv.org/abs/1905.12227.

[25] S. Dufferwiel *et al.*, “Exciton-polaritons in van der Waals heterostructures embedded in

tunable microcavities," *Nat. Commun.*, vol. 6, no. May, pp. 1–7, 2015.

[26] N. Lundt *et al.*, "Room-temperature Tamm-plasmon exciton-polaritons with a WSe2 monolayer," *Nat. Commun.*, vol. 7, p. 13328, 2016.

[27] L. Zhang, R. Gogna, W. Burg, E. Tutuc, and H. Deng, "Photonic-crystal exciton-polaritons in monolayer semiconductors," *Nat. Commun.*, vol. 9, no. 1, p. 713, 2018.

[28] B. Lee *et al.*, "Electrical Tuning of Exciton-Plasmon Polariton Coupling in Monolayer MoS2 Integrated with Plasmonic Nanoantenna Lattice," *Nano Lett.*, vol. 17, no. 7, pp. 4541–4547, 2017.

[29] L. Zhang *et al.*, "Van der Waals heterostructure polaritons with moiré-induced nonlinearity," *Nature*, vol. 591, no. 7848, pp. 61–65, 2021.

[30] R. Peng, C. Chen, and M. Li, "Broadband Waveguide Integrated Black Phosphorus Modulator for Mid Infrared Application," 2018.

[31] A. Castellanos-Gomez, "Black Phosphorus: Narrow Gap, Wide Applications," *Journal of Physical Chemistry Letters*, vol. 6, no. 21. pp. 4280–4291, 2015.

[32] M. Long *et al.*, "Room temperature high-detectivity mid-infrared photodetectors based on black arsenic phosphorus," *Sci. Adv.*, vol. 3, no. 6, 2017.

[33] R. Peng, K. Khaliji, N. Youngblood, R. Grassi, T. Low, and M. Li, "Midinfrared Electro-optic Modulation in Few-Layer Black Phosphorus," *Nano Lett.*, vol. 17, no. 10, pp. 6315–6320, 2017.

[34] T. Low *et al.*, "Tunable optical properties of multilayer black phosphorus thin films," *Phys. Rev. B - Condens. Matter Mater. Phys.*, vol. 90, no. 7, 2014.

[35] G. Zhang *et al.*, "Infrared fingerprints of few-layer black phosphorus," *Nat. Commun.*, vol. 8, 2017.

[36] B. Deng *et al.*, "Efficient electrical control of thin-film black phosphorus bandgap," *Nat. Commun.*, vol. 8, 2017.

[37] W. S. Whitney *et al.*, "Field Effect Optoelectronic Modulation of Quantum-Confined Carriers in Black Phosphorus," *Nano Letters*, vol. 17, no. 1. pp. 78–84, 2020.

[38] J. Kim *et al.*, "Observation of tunable band gap and anisotropic Dirac semimetal state in black phosphorus," *Science*, vol. 349, no. 6249, pp. 723–726, 2015.

[39] C. Lin, R. Grassi, T. Low, and A. S. Helmy, "Multilayer Black Phosphorus as a Versatile Mid-Infrared Electro-optic Material," *Nano Lett.*, vol. 16, no. 3, pp. 1683–1689, 2016.

[40] A. Castellanos-Gomez *et al.*, "Deterministic transfer of two-dimensional materials by all-dry viscoelastic stamping," *2D Mater.*, vol. 1, no. 1, 2014.

[41] C. H. Liu *et al.*, "Nanocavity integrated van der Waals heterostructure light-emitting tunneling diode," *Nano Lett.*, vol. 17, no. 1, pp. 200–205, 2017.

[42] X. Gan *et al.*, "Chip-integrated ultrafast graphene photodetector with high responsivity," *Nat. Photonics*, vol. 7, no. 11, pp. 883–887, 2013.

[43] N. Youngblood, C. Chen, S. J. Koester, and M. Li, "Waveguide-integrated black phosphorus photodetector with high responsivity and low dark current," *Nat. Photonics*, vol. 9, no. 4, pp. 247–252, 2015.

[44] Y. Q. Bie *et al.*, "A MoTe2-based light-emitting diode and photodetector for silicon photonic integrated circuits," *Nat. Nanotechnol.*, vol. 12, no. 12, pp. 1124–1129, 2017.

[45] A. K. Geim and I. V. Grigorieva, "Van der Waals heterostructures," *Nature*, vol. 499, no. 7459. pp. 419–425, 2013.

[46] L. Li *et al.*, "Direct observation of the layer-dependent electronic structure in phosphorene," *Nat. Nanotechnol.*, vol. 12, no. 1, pp. 21–25, 2017.

[47] M. Buscema, D. J. Groenendijk, G. A. Steele, H. S. J. Van Der Zant, and A. Castellanos-Gomez, "Photovoltaic effect in few-layer black phosphorus PN junctions defined by local electrostatic gating," *Nat. Commun.*, vol. 5, pp. 1–6, 2014, [Online]. Available: http://arxiv.org/abs/1407.2863.

[48] T. Hong *et al.*, "Polarized photocurrent response in black phosphorus field-effect transistors," *Nanoscale*, vol. 6, no. 15, pp. 8978–8983, Aug. 2014, Accessed: Oct. 02, 2014. [Online]. Available: http://arxiv.org/abs/1409.4729.

[49] H. Yuan *et al.*, "Polarization-sensitive broadband photodetector using a black phosphorus vertical p-n junction," *Nat. Nanotechnol.*, vol. 10, no. 8, pp. 707–713, 2015.

[50] J. Wu *et al.*, “Colossal Ultraviolet Photoresponsivity of Few-Layer Black Phosphorus,” *ACS Nano*, vol. 9, no. 8, pp. 8070–8077, 2015.

[51] H. Yuan *et al.*, “Broadband Linear-Dichroic Photodetector in a Black Phosphorus Vertical p-n Junction,” *Arxiv*, p. 18, Sep. 2014, Accessed: Jan. 13, 2015. [Online]. Available: http://arxiv.org/abs/1409.4729%0Ahttp://dx.doi.org/10.1038/nnano.2015.112.

[52] M. Xu, Y. Gu, R. Peng, N. Youngblood, and M. Li, “Black phosphorus mid-infrared photodetectors,” *Appl. Phys. B Lasers Opt.*, vol. 123, no. 4, 2017.

[53] M. Engel, M. Steiner, and P. Avouris, “Black phosphorus photodetector for multispectral, high-resolution imaging,” *Nano Lett.*, vol. 14, no. 11, pp. 6414–6417, Oct. 2014.

[54] H. Zeng, J. Dai, W. Yao, D. Xiao, and X. Cui, “Valley polarization in MoS 2 monolayers by optical pumping,” *Nat. Nanotechnol.*, vol. 7, no. 8, pp. 490–493, 2012.

[55] P. Rivera *et al.*, “Valley-polarized exciton dynamics in a 2D semiconductor heterostructure,” *Science*, vol. 351, no. 6274, pp. 688–691, 2016.

[56] J. R. Schaibley *et al.*, “Valleytronics in 2D materials,” *Nature Reviews Materials*, vol. 1, no. 11. p. 16055, 2016.

[57] D. Unuchek *et al.*, “Valley-polarized exciton currents in a van der Waals heterostructure,” *Nature Nanotechnology*, vol. 14, no. 12. pp. 1104–1109, 2019.

[58] P. Rivera, H. Yu, K. L. Seyler, N. P. Wilson, W. Yao, and X. Xu, “Interlayer valley excitons in heterobilayers of transition metal dichalcogenides,” *Nature Nanotechnology*, vol. 13, no. 11. pp. 1004–1015, 2018.

[59] H. Shi *et al.*, “Exciton dynamics in suspended monolayer and few-layer MoS2 2D crystals,” *ACS Nano*, vol. 7, no. 2, pp. 1072–1080, 2013.

[60] Z. Li *et al.*, “Revealing the biexciton and trion-exciton complexes in BN encapsulated WSe2,” *Nat. Commun.*, vol. 9, no. 1, 2018.

[61] M. Massicotte *et al.*, “Dissociation of two-dimensional excitons in monolayer WSe2,” *Nat. Commun.*, vol. 9, no. 1, 2018.

[62] A. Javey *et al.*, “Neutral exciton diffusion in monolayer MoS2,” *ACS Nano*, vol. 14, no. 10, pp. 13433–13440, 2020.

[63] C. T. Phare, Y. H. Daniel Lee, J. Cardenas, and M. Lipson, “Graphene electro-optic modulator with 30 GHz bandwidth,” *Nat. Photonics*, vol. 9, no. 8, pp. 511–514, 2015.

[64] N. Youngblood, Y. Anugrah, R. Ma, S. J. Koester, and M. Li, “Multifunctional graphene optical modulator and photodetector integrated on silicon waveguides,” *Nano Lett.*, vol. 14, no. 5, pp. 2741–2746, 2014.

[65] S. J. Koester and M. Li, “High-speed waveguide-coupled graphene-on-graphene optical modulators,” *Appl. Phys. Lett.*, vol. 100, no. 17, 2012.

[66] M. Liu *et al.*, “A graphene-based broadband optical modulator,” *Nature*, vol. 474, no. 7349, pp. 64–67, 2011.

[67] O. Lopez-Sanchez, D. Lembke, M. Kayci, A. Radenovic, and A. Kis, “Ultrasensitive photodetectors based on monolayer MoS 2,” *Nat. Nanotechnol.*, vol. 8, no. 7, pp. 497–501, 2013.

[68] B. Radisavljevic, A. Radenovic, J. Brivio, V. Giacometti, and A. Kis, “Single-layer MoS2 transistors,” *Nat. Nanotechnol.*, vol. 6, no. 3, pp. 147–150, 2011.

[69] L. Li *et al.*, “Black phosphorus field-effect transistors,” *Nat. Nanotechnol.*, vol. 9, no. 5, pp. 372–377, 2014.

[70] A. Favron *et al.*, “Exfoliating pristine black phosphorus down to the monolayer: photo-oxidation and electronic confinement effects,” Aug. 2014, Accessed: Oct. 02, 2014. [Online]. Available: http://arxiv.org/abs/1408.0345.

[71] Y. Du, H. Liu, Y. Deng, and P. D. Ye, “Device perspective for black phosphorus field-effect transistors: Contact resistance, ambipolar behavior, and scaling,” *ACS Nano*, vol. 8, no. 10, pp. 10035–10042, 2014.

[72] J. Miao, S. Zhang, L. Cai, M. Scherr, and C. Wang, “Ultrashort Channel Length Black Phosphorus Field-Effect Transistors,” *ACS Nano*, vol. 9, no. 9, pp. 9236–9243, 2015.

[73] J. Na *et al.*, “Few-layer black phosphorus field-effect transistors with reduced current fluctuation,” *ACS Nano*, vol. 8, no. 11, pp. 11753–11762, 2014.

[74] N. Peimyoo *et al.*, “Electrical tuning of optically active interlayer excitons in bilayer MoS2,” *Nat. Nanotechnol.*, vol. 16, pp. 888–893, 2021.

[75] L. A. Jauregui *et al.*, "Electrical control of interlayer exciton dynamics in atomically thin heterostructures," *Science*, vol. 366, no. 6467, pp. 870–875, 2019.

[76] M. M. Altaiary, E. Liu, C. Liang, F. Hsiao, and J. Van Baren, "Electric-field-tunable intervalley excitons and phonon replicas in bilayer WSe 2," *arXiv*, p. 2101.11161, 2021.

[77] J. Lee, K. F. Mak, and J. Shan, "Electrical control of the valley Hall effect in bilayer MoS 2 transistors," *Nat. Nanotechnol.*, vol. 11, no. 5, pp. 421–425, 2016.

[78] J. Klein *et al.*, "Electric-field switchable second-harmonic generation in bilayer MoS2 by inversion symmetry breaking," *Nano Lett.*, vol. 17, no. 1, pp. 392–398, 2017.

[79] S. Huang *et al.*, "Strain-tunable van der Waals interactions in few-layer black phosphorus," *Nat. Commun.*, vol. 10, no. 1, 2019.

[80] H. Kim *et al.*, "Actively variable-spectrum optoelectronics with black phosphorus," *Nature*, vol. 596, no. 7871, pp. 232–237, 2021.

[81] W. Wu *et al.*, "Piezoelectricity of single-atomic-layer MoS2 for energy conversion and piezotronics," *Nature*, vol. 514, no. 7253, pp. 470–474, 2014.

[82] H. Guo, N. Lu, L. Wang, X. Wu, and X. C. Zeng, "Tuning electronic and magnetic properties of early transition-metal dichalcogenides via tensile strain," *J. Phys. Chem. C*, vol. 118, no. 13, pp. 7242–7249, 2014.

[83] I. Niehues *et al.*, "Strain Control of Exciton-Phonon Coupling in Atomically Thin Semiconductors," *Nano Lett.*, vol. 18, no. 3, pp. 1751–1757, 2018.

[84] X. Zhao *et al.*, "Strain Modulation by van der Waals Coupling in Bilayer Transition Metal Dichalcogenide," *ACS Nano*, vol. 12, no. 2, pp. 1940–1948, 2018.

[85] A. Branny, S. Kumar, R. Proux, and B. D. Gerardot, "Deterministic strain-induced arrays of quantum emitters in a two-dimensional semiconductor," *Nat. Commun.*, vol. 8, 2017.

[86] Y. Luo *et al.*, "Deterministic coupling of site-controlled quantum emitters in monolayer WSe2 to plasmonic nanocavities," *Nature Nanotechnology*, vol. 13, no. 12. pp. 1137–1142, 2018.

[87] L. Sortino *et al.*, "Bright single photon emitters with enhanced quantum efficiency in a two-dimensional semiconductor coupled with dielectric nano-antennas," *Nat. Commun.*, vol. 12,

no. 1, 2021.

[88] R. W. Keyes, “The electrical properties of black phosphorus,” *Phys. Rev.*, vol. 92, no. 3, pp. 580–584, 1953.

[89] X. Ling, H. Wang, S. Huang, F. Xia, and M. S. Dresselhaus, “The renaissance of black phosphorus,” *Proceedings of the National Academy of Sciences of the United States of America*, vol. 112, no. 15. pp. 4523–4530, 2015.

[90] F. Xia, H. Wang, and Y. Jia, “Rediscovering black phosphorus as an anisotropic layered material for optoelectronics and electronics,” *Nat. Commun.*, vol. 5, 2014.

[91] A. Brown and S. Rundqvist, “Refinement of the crystal structure of black phosphorus,” *Acta Crystallogr.*, vol. 19, no. 4, pp. 684–685, 1965.

[92] X. Wang *et al.*, “Highly anisotropic and robust excitons in monolayer black phosphorus,” *Nat. Nanotechnol.*, vol. 10, no. 6, pp. 517–521, 2015.

[93] Q. Wei and X. Peng, “Superior mechanical flexibility of phosphorene and few-layer black phosphorus,” *Appl. Phys. Lett.*, vol. 104, no. 25, 2014.

[94] J. Qiao, X. Kong, Z. X. Hu, F. Yang, and W. Ji, “High-mobility transport anisotropy and linear dichroism in few-layer black phosphorus,” *Nat. Commun.*, vol. 5, 2014.

[95] S. Biswas, M. Y. Grajower, K. Watanabe, T. Taniguchi, and H. A. Atwater, “Broadband electro-optic polarization conversion with atomically thin black phosphorus,” *Science*, vol. 374, no. 6566, pp. 448–453, 2021.

[96] S. Biswas *et al.*, “Tunable intraband optical conductivity and polarization-dependent epsilon-near-zero behavior in black phosphorus,” *Sci. Adv.*, vol. 7, no. 2, 2021.

[97] E. Van Veen *et al.*, “Tuning Two-Dimensional Hyperbolic Plasmons in Black Phosphorus,” *Phys. Rev. Appl.*, vol. 12, no. 1, 2019.

[98] F. Wang *et al.*, “Prediction of hyperbolic exciton-polaritons in monolayer black phosphorus,” *Nat. Commun.*, vol. 12, no. 1, 2021.

[99] Q. Liu, X. Zhang, L. B. Abdalla, A. Fazzio, and A. Zunger, “Switching a normal insulator into a topological insulator via electric field with application to phosphorene,” *Nano Lett.*, vol. 15, no. 2, pp. 1222–1228, 2015.

[100] S. Das, W. Zhang, M. Demarteau, A. Hoffmann, M. Dubey, and A. Roelofs, "Tunable transport gap in phosphorene," *Nano Lett.*, vol. 14, no. 10, pp. 5733–5739, 2014.

[101] Q. Guo *et al.*, "Black phosphorus mid-infrared photodetectors with high gain," *Nano Lett.*, vol. 16, no. 7, pp. 4648–4655, 2016.

[102] H. K. Choi and G. W. Turner, "InAsSb/InAlAsSb strained quantum-well diode lasers emitting at 3.9 μm," *Appl. Phys. Lett.*, vol. 67, p. 332, 1995.

[103] J. M. Dell *et al.*, "HgCdTe mid-wavelength IR photovoltaic detectors fabricated using plasma induced junction technology," *J. Electron. Mater.*, vol. 29, no. 6, pp. 841–848, 2000.

[104] H. Shao, W. Li, A. Torfi, D. Moscicka, and W. I. Wang, "Room-temperature InAsSb photovoltaic detectors for mid-infrared applications," *IEEE Photonics Technol. Lett.*, vol. 18, no. 16, pp. 1756–1758, 2006.

[105] N. Youngblood and M. Li, "Ultrafast photocurrent measurements of a black phosphorus photodetector," *Appl. Phys. Lett.*, vol. 110, no. 5, 2017.

[106] F. Xia, T. Mueller, Y. M. Lin, A. Valdes-Garcia, and P. Avouris, "Ultrafast graphene photodetector," *Nat. Nanotechnol.*, vol. 4, no. 12, pp. 839–843, 2009.

[107] T. Mueller, F. Xia, and P. Avouris, "Graphene photodetectors for high-speed optical communications," *Nat. Photonics*, vol. 4, no. 5, pp. 297–301, 2010.

[108] X. Wang, Z. Cheng, K. Xu, H. K. Tsang, and J. Bin Xu, "High-responsivity graphene/silicon-heterostructure waveguide photodetectors," *Nat. Photonics*, vol. 7, no. 11, pp. 888–891, 2013.

[109] A. Pospischil *et al.*, "CMOS-compatible graphene photodetector covering all optical communication bands," *Nat. Photonics*, vol. 7, no. 11, pp. 892–896, 2013.

[110] L. Ye, H. Li, Z. Chen, and J. Xu, "Near-Infrared Photodetector Based on MoS2/Black Phosphorus Heterojunction," *ACS Photonics*, vol. 3, no. 4, pp. 692–699, 2016.

[111] J. Bullock *et al.*, "Polarization-resolved black phosphorus/molybdenum disulfide mid-wave infrared photodiodes with high detectivity at room temperature," *Nat. Photonics*, vol. 12, no. 10, pp. 601–607, 2018.

[112] A. Gao *et al.*, "Observation of ballistic avalanche phenomena in nanoscale vertical InSe/BP

heterostructures," *Nature Nanotechnology*, vol. 14, no. 3. pp. 217–222, 2019.

[113] Z. Wang *et al.*, "Black phosphorus nanoelectromechanical resonators vibrating at very high frequencies," *Nanoscale*, vol. 7, no. 3, pp. 877–884, 2015.

[114] H. Liu *et al.*, "Phosphorene: An unexplored 2D semiconductor with a high hole mobility," *ACS Nano*, vol. 8, no. 4, pp. 4033–4041, 2014.

[115] Y. Yao *et al.*, "Electrically tunable metasurface perfect absorbers for ultrathin mid-infrared optical modulators," *Nano Lett.*, vol. 14, no. 11, pp. 6526–6532, 2014.

[116] B. Sensale-Rodriguez *et al.*, "Broadband graphene terahertz modulators enabled by intraband transitions," *Nat. Commun.*, vol. 3, 2012.

[117] D. A. B. Miller, D. S. Chemla, and S. Schmitt-Rink, "Relation between electroabsorption in bulk semiconductors and in quantum wells: The quantum-confined Franz-Keldysh effect," *Phys. Rev. B*, vol. 33, no. 10, pp. 6976–6982, 1986.

[118] J. Liu *et al.*, "Waveguide-integrated, ultralow-energy GeSi electro-absorption modulators," *Nat. Photonics*, vol. 2, no. 7, pp. 433–437, 2008.

[119] D. Feng *et al.*, "High speed GeSi electro-absorption modulator at 1550 nm wavelength on SOI waveguide," *Opt. Express*, vol. 20, no. 20, p. 22224, 2012.

[120] R. A. Soref, G. Sun, and H. H. Cheng, "Franz-Keldysh electro-absorption modulation in germanium-tin alloys," *J. Appl. Phys.*, vol. 111, no. 12, 2012.

[121] X. Fu *et al.*, "5 x 20 Gb/s heterogeneously integrated III-V on silicon electro-absorption modulator array with arrayed waveguide grating multiplexer," *Opt. Express*, vol. 23, no. 14, p. 18686, 2015.

[122] A. Morita, "Semiconducting black phosphorus," *Appl. Phys. A Solids Surfaces*, vol. 39, no. 4, pp. 227–242, 1986.

[123] M. N. Polyanskiy, "Refractive index database," *https://refractiveindex.info*. .

[124] J. Miao, L. Zhang, and C. Wang, "Black phosphorus electronic and optoelectronic devices," *2D Materials*, vol. 6, no. 3. 2019.

[125] A. Soibel *et al.*, "Midinfrared interband cascade laser for free space optical

communication," *IEEE Photonics Technol. Lett.*, vol. 22, no. 2, pp. 121–123, 2010.

[126] G. Wysocki and D. Weidmann, "Molecular dispersion spectroscopy for chemical sensing using chirped mid-infrared quantum cascade laser," *Opt. Express*, vol. 18, no. 25, p. 26123, 2010.

[127] N. Gayraud *et al.*, "Mid-infrared gas sensing using a photonic bandgap fiber," *Appl. Opt.*, vol. 47, no. 9, pp. 1269–1277, 2008.

[128] C. Palacios-Berraquero *et al.*, "Atomically thin quantum light-emitting diodes," *Nat. Commun.*, vol. 7, 2016.

[129] Y. Yin *et al.*, "High-Speed and High-Responsivity Hybrid Silicon/Black-Phosphorus Waveguide Photodetectors at 2 µm," *Laser Photonics Rev.*, vol. 13, no. 6, 2019.

[130] Z. Hu *et al.*, "Water-Catalyzed Oxidation of Few-Layer Black Phosphorous in a Dark Environment," *Angew. Chemie - Int. Ed.*, vol. 56, no. 31, pp. 9131–9135, 2017.

[131] Y. Huang *et al.*, "Interaction of black phosphorus with oxygen and water," *Chem. Mater.*, vol. 28, no. 22, pp. 8330–8339, 2016.

[132] J. Gómez-Pérez, B. Barna, I. Y. Tóth, Z. Kónya, and Á. Kukovecz, "Quantitative Tracking of the Oxidation of Black Phosphorus in the Few-Layer Regime," *ACS Omega*, vol. 3, no. 10, pp. 12482–12488, 2018.

[133] K. L. Utt *et al.*, "Intrinsic defects, fluctuations of the local shape, and the photo-oxidation of black phosphorus," *ACS Cent. Sci.*, vol. 1, no. 6, pp. 320–327, 2015.

[134] J. D. Wood *et al.*, "Effective passivation of exfoliated black phosphorus transistors against ambient degradation," *Nano Lett.*, vol. 14, no. 12, pp. 6964–6970, 2014.

[135] C. R. Ryder *et al.*, "Covalent functionalization and passivation of exfoliated black phosphorus via aryl diazonium chemistry," *Nat. Chem.*, vol. 8, no. 6, pp. 597–602, 2016.

[136] D. Tofan *et al.*, "Surface Modification of Black Phosphorus with Group 13 Lewis Acids for Ambient Protection and Electronic Tuning," *Angew. Chemie - Int. Ed.*, vol. 60, no. 15, pp. 8329–8336, 2021.

[137] C. V. Poulton *et al.*, "Coherent solid-state LIDAR with silicon photonic optical phased arrays," *Opt. Lett.*, vol. 42, no. 20, p. 4091, 2017.

[138] A. Martin *et al.*, “Photonic integrated circuit-based FMCW coherent LiDAR,” *J. Light. Technol.*, vol. 36, no. 19, pp. 4640–4645, 2018.

[139] J. K. Doylend and S. Gupta, “An overview of silicon photonics for LIDAR,” 2020, p. 17.

[140] Wikipedia, “Infrared window,” *https://en.wikipedia.org/wiki/Infrared_window*. .

[141] T. Hemati and B. Weng, “The Mid-Infrared Photonic Crystals for Gas Sensing Applications,” in *Photonic Crystals - A Glimpse of the Current Research Trends*, 2019.

[142] M. Nedeljkovic *et al.*, “Silicon-on-insulator free-carrier injection modulators for the mid-infrared,” *Opt. Lett.*, vol. 44, no. 4, p. 915, 2019.

[143] H. Lin *et al.*, “Chalcogenide glass-on-graphene photonics,” *Nat. Photonics*, vol. 11, no. 12, pp. 798–805, 2017.

[144] ISOMET, “Modulator Mid-IR,” *https://isomet.com/modmidnir.html*. .

[145] S. Lee, R. Peng, and M. Li, “Broadband, waveguide-integrated mid-infrared black phosphorus modulator with high modulation depth,” in *Optics InfoBase Conference Papers*, 2020, vol. Part F183-.

[146] M. Ono *et al.*, “Ultrafast and energy-efficient all-optical switching with graphene-loaded deep-subwavelength plasmonic waveguides,” *Nat. Photonics*, vol. 14, no. 1, pp. 37–43, 2020.

[147] D. Kufer and G. Konstantatos, “Highly Sensitive, Encapsulated MoS2 Photodetector with Gate Controllable Gain and Speed,” *Nano Lett.*, vol. 15, no. 11, pp. 7307–7313, 2015.

[148] J. Shi *et al.*, “Plasmonic Enhancement and Manipulation of Optical Nonlinearity in Monolayer Tungsten Disulfide,” *Laser Photonics Rev.*, vol. 12, no. 10, 2018.

[149] Y. K. Srivastava *et al.*, “MoS2 for Ultrafast All-Optical Switching and Modulation of THz Fano Metaphotonic Devices,” *Adv. Opt. Mater.*, vol. 5, no. 23, 2017.

[150] Z. Q. Xu *et al.*, “Atomically thin lateral p-n junction photodetector with large effective detection area,” *2D Mater.*, vol. 3, no. 4, 2016.

[151] R. C. Miller, D. A. Kleinman, W. T. Tsang, and A. C. Gossard, “Observation of the excited level of excitons in GaAs quantum wells,” *Phys. Rev. B*, vol. 24, no. 2, pp. 1134–1136,

1981.

[152] Z. Wang *et al.*, “Evidence of high-temperature exciton condensation in two-dimensional atomic double layers,” *Nature*, vol. 574, no. 7776, pp. 76–80, 2019.

[153] M. Waldherr *et al.*, “Observation of bosonic condensation in a hybrid monolayer MoSe2-GaAs microcavity,” *Nat. Commun.*, vol. 9, no. 1, 2018.

[154] C. Anton-Solanas *et al.*, “Bosonic condensation of exciton–polaritons in an atomically thin crystal,” *Nat. Mater.*, vol. 20, no. 9, pp. 1233–1239, 2021.

[155] A. M. Jones *et al.*, “Optical generation of excitonic valley coherence in monolayer WSe 2,” *Nat. Nanotechnol.*, vol. 8, no. 9, pp. 634–638, 2013.

[156] H. Deng, H. Haug, and Y. Yamamoto, “Exciton-polariton Bose-Einstein condensation,” *Rev. Mod. Phys.*, vol. 82, no. 2, pp. 1489–1537, 2010.

[157] K. Parto, S. I. Azzam, K. Banerjee, and G. Moody, “Defect and strain engineering of monolayer WSe2 enables site-controlled single-photon emission up to 150 K,” *Nat. Commun.*, vol. 12, no. 1, 2021.

[158] A. A. High, E. E. Novitskaya, L. V. Butov, M. Hanson, and A. C. Gossard, “Control of exciton fluxes in an excitonic integrated circuit,” *Science*, vol. 321, no. 5886, pp. 229–231, 2008.

[159] J. A. Brum and G. Bastard, “Electric-field-induced dissociation of excitons in semiconductor quantum wells,” *Phys. Rev. B*, vol. 31, no. 6, pp. 3893–3898, 1985.

[160] C. Rocke, A. Govorov, A. Wixforth, G. Böhm, and G. Weimann, “Exciton ionization in a quantum well studied by surface acoustic waves,” *Phys. Rev. B - Condens. Matter Mater. Phys.*, vol. 57, no. 12, pp. R6850–R6853, 1998.

[161] J. Hegarty, L. Goldner, and M. D. Sturge, “Localized and delocalized two-dimensional excitons in GaAs-AlGaAs multiple-quantum-well structures,” *Phys. Rev. B*, vol. 30, no. 12, pp. 7346–7348, 1984.

[162] A. Gärtner, A. W. Holleitner, J. P. Kotthaus, and D. Schuh, “Drift mobility of long-living excitons in coupled GaAs quantum wells,” *Appl. Phys. Lett.*, vol. 89, no. 5, p. 52108, 2006.

[163] F. Cadiz *et al.*, “Exciton diffusion in WSe2 monolayers embedded in a van der Waals

heterostructure," *Appl. Phys. Lett.*, vol. 112, no. 15, p. 152106, 2018.

[164] M. Kulig *et al.*, "Exciton Diffusion and Halo Effects in Monolayer Semiconductors," *Phys. Rev. Lett.*, vol. 120, no. 20, p. 207401, 2018.

[165] F. Withers *et al.*, "WSe2 Light-Emitting Tunneling Transistors with Enhanced Brightness at Room Temperature," *Nano Lett.*, vol. 15, no. 12, pp. 8223–8228, 2015.

[166] Z. Wang, Y. H. Chiu, K. Honz, K. F. Mak, and J. Shan, "Electrical Tuning of Interlayer Exciton Gases in WSe2 Bilayers," *Nano Lett.*, vol. 18, no. 1, pp. 137–143, 2018.

[167] K. L. Seyler *et al.*, "Signatures of moiré-trapped valley excitons in MoSe2/WSe2 heterobilayers," *Nature*, vol. 567, no. 7746, pp. 66–70, 2019.

[168] C. Jin *et al.*, "Observation of moiré excitons in WSe2/WS2 heterostructure superlattices," *Nature*, vol. 567, no. 7746, pp. 76–80, 2019.

[169] K. Tran *et al.*, "Evidence for moiré excitons in van der Waals heterostructures," *Nature*, vol. 567, no. 7746, pp. 71–75, 2019.

[170] P. Rivera *et al.*, "Observation of long-lived interlayer excitons in monolayer MoSe 2-WSe 2 heterostructures," *Nat. Commun.*, vol. 6, p. 6242, 2015.

[171] H. Yu, G. Bin Liu, J. Tang, X. Xu, and W. Yao, "Moiré excitons: From programmable quantum emitter arrays to spin-orbit–coupled artificial lattices," *Sci. Adv.*, vol. 3, no. 11, 2017.

[172] D. Unuchek, A. Ciarrocchi, A. Avsar, K. Watanabe, T. Taniguchi, and A. Kis, "Room-temperature electrical control of exciton flux in a van der Waals heterostructure," *Nature*, vol. 560, no. 7718, pp. 340–344, 2018.

[173] Y. Liu, K. Dini, Q. Tan, T. Liew, K. S. Novoselov, and W. Gao, "Electrically controllable router of interlayer excitons," *Sci. Adv.*, vol. 6, no. 41, p. eaba1830, 2020.

[174] P. Delsing *et al.*, "The 2019 surface acoustic waves roadmap," *Journal of Physics D: Applied Physics*, vol. 52, no. 35. p. 353001, 2019.

[175] S. Maity *et al.*, "Coherent acoustic control of a single silicon vacancy spin in diamond," *Nat. Commun.*, vol. 11, no. 1, 2020.

[176] D. A. Fuhrmann *et al.*, “Dynamic modulation of photonic crystal nanocavities using gigahertz acoustic phonons,” *Nat. Photonics*, vol. 5, no. 10, pp. 605–609, 2011.

[177] S. Takada *et al.*, “Sound-driven single-electron transfer in a circuit of coupled quantum rails,” *Nat. Commun.*, vol. 10, no. 1, 2019.

[178] M. V. Gustafsson, T. Aref, A. F. Kockum, M. K. Ekström, G. Johansson, and P. Delsing, “Propagating phonons coupled to an artificial atom,” *Science*, vol. 346, no. 6206, pp. 207–211, 2014.

[179] A. Violante, K. Cohen, S. Lazić, R. Hey, R. Rapaport, and P. V. Santos, “Dynamics of indirect exciton transport by moving acoustic fields,” *New J. Phys.*, vol. 16, p. 33035, 2014.

[180] J. Rudolph, R. Hey, and P. V. Santos, “Long-range exciton transport by dynamic strain fields in a GaAs quantum well,” *Phys. Rev. Lett.*, vol. 99, no. 4, p. 47602, 2007.

[181] C. Rocke, S. Zimmermann, A. Wixforth, J. P. Kotthaus, G. Böhm, and G. Weimann, “Acoustically driven storage of light in a quantum well,” *Phys. Rev. Lett.*, vol. 78, no. 21, pp. 4099–4102, 1997.

[182] E. A. Cerda-Méndez *et al.*, “Polariton condensation in dynamic acoustic lattices,” *Phys. Rev. Lett.*, vol. 105, no. 11, p. 116402, 2010.

[183] K. Datta, Z. Li, Z. Lyu, and P. B. Deotare, “Piezoelectric Modulation of Excitonic Properties in Monolayer WSe2under Strong Dielectric Screening,” *ACS Nano*, vol. 15, no. 7, pp. 12334–12341, 2021.

[184] D. V. Gulyaev and K. S. Zhuravlev, “Mechanisms of exciton photoluminescence quenching in the electric field of a standing surface acoustic wave,” *Int. J. Mod. Phys. B*, vol. 33, no. 6, 2019.

[185] A. R. Rezk *et al.*, “Acoustic-Excitonic Coupling for Dynamic Photoluminescence Manipulation of Quasi-2D MoS2 Nanoflakes,” *Adv. Opt. Mater.*, vol. 3(7), pp. 888–894, 2015.

[186] A. R. Rezk *et al.*, “Acoustically-Driven Trion and Exciton Modulation in Piezoelectric Two-Dimensional MoS2,” *Nano Lett.*, vol. 16, no. 2, pp. 849–855, 2016.

[187] P. J. Zomer, M. H. D. Guimarães, J. C. Brant, N. Tombros, and B. J. Van Wees, “Fast pick

up technique for high quality heterostructures of bilayer graphene and hexagonal boron nitride," *Appl. Phys. Lett.*, vol. 105, no. 1, 2014.

[188] D. G. Purdie, N. M. Pugno, T. Taniguchi, K. Watanabe, A. C. Ferrari, and A. Lombardo, "Cleaning interfaces in layered materials heterostructures," *Nat. Commun.*, vol. 9, no. 1, 2018.

[189] D. Rhodes, S. H. Chae, R. Ribeiro-Palau, and J. Hone, "Disorder in van der Waals heterostructures of 2D materials," *Nature Materials*, vol. 18, no. 6. pp. 541–549, 2019.

[190] J. Wang *et al.*, "Optical generation of high carrier densities in 2D semiconductor heterobilayers," *Sci. Adv.*, vol. 5, no. 9, 2019.

[191] Z. Wu *et al.*, "Large-scale growth of few-layer two-dimensional black phosphorus," *Nat. Mater.*, vol. 20, no. 9, pp. 1203–1209, 2021, doi: 10.1038/s41563-021-01001-7.

[192] T. Li *et al.*, "Epitaxial growth of wafer-scale molybdenum disulfide semiconductor single crystals on sapphire," *Nat. Nanotechnol.*, vol. 16, no. 11, pp. 1201–1207, 2021, doi: 10.1038/s41565-021-00963-8.

[193] W. Meng *et al.*, "Three-dimensional monolithic micro-LED display driven by atomically thin transistor matrix," *Nat. Nanotechnol.*, vol. 16, no. 11, pp. 1231–1236, 2021, doi: 10.1038/s41565-021-00966-5.

[194] S. Lee, R. Peng, C. Wu, and M. Li, "Programmable black phosphorus image sensor for broadband optoelectronic edge computing," *arXiv*, 2021.

[195] Z. Zhang, S. Wang, C. Liu, R. Xie, W. Hu, and P. Zhou, "All-in-one two-dimensional retinomorphic hardware device for motion detection and recognition," *Nat. Nanotechnol.*, vol. 17, no. 1, pp. 27–32, 2022, doi: 10.1038/s41565-021-01003-1.

[196] Z. Huang *et al.*, "Robust Room Temperature Valley Hall Effect of Interlayer Excitons," *Nano Lett.*, vol. 20, no. 2, pp. 1345–1351, 2020, doi: 10.1021/acs.nanolett.9b04836.

APPENDIX A

Figure A.1. The emission spectrum of bilayer WSe_2 at the pump position when T=6 K. When the SAW is on, all the sharp emission resonances disappear due to delocalization of the excitons and reduced coupling with localized phonon modes.

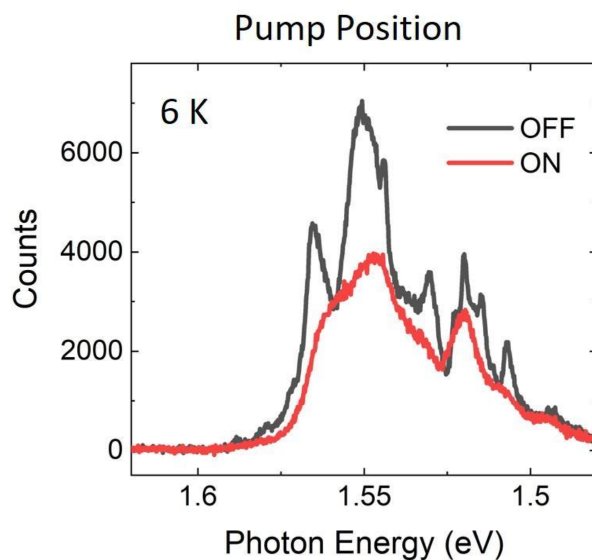

Figure A.2. The emission spectrum of bilayer WSe_2 at the pump (a) and edge (b) position when T=30 K.

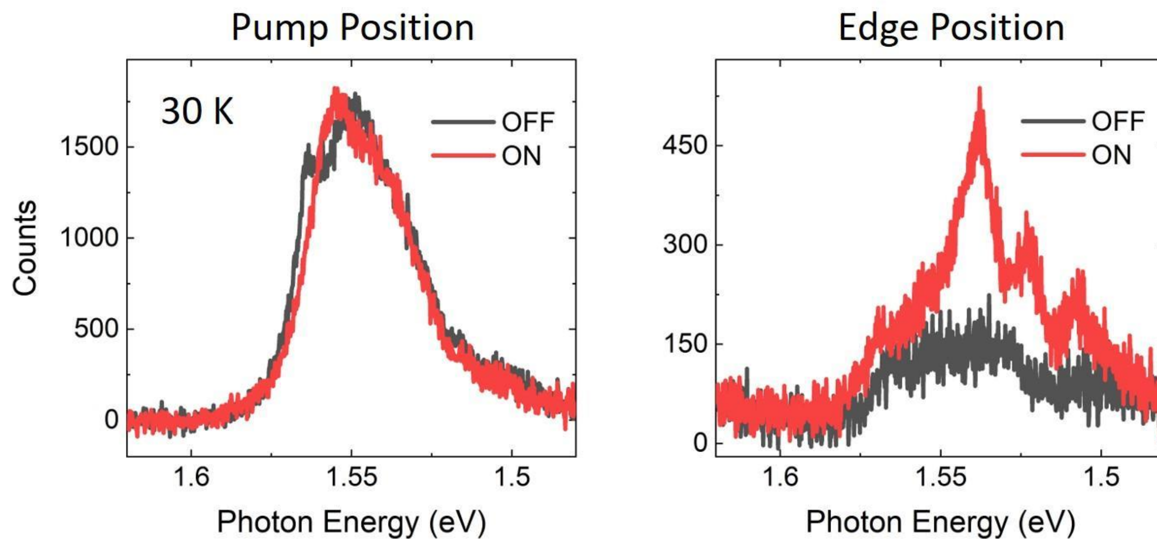

Figure A.3. The emission spectrum of bilayer WSe_2 at the pump (a) and edge (b) position when T=200 K.

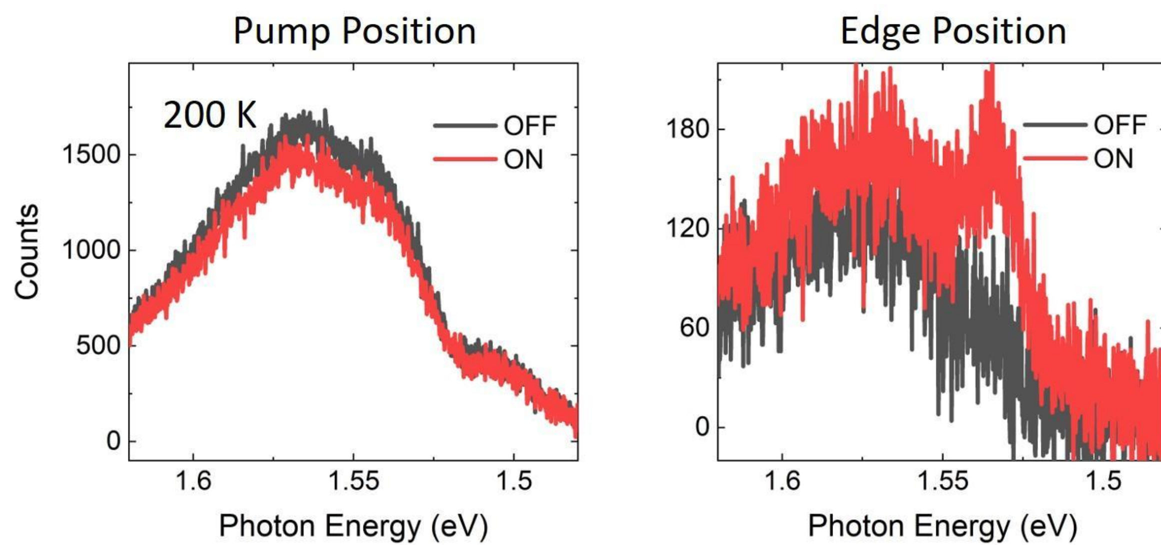

Figure A.4. Exciton transport of bilayer WSe_2 at 50 K.

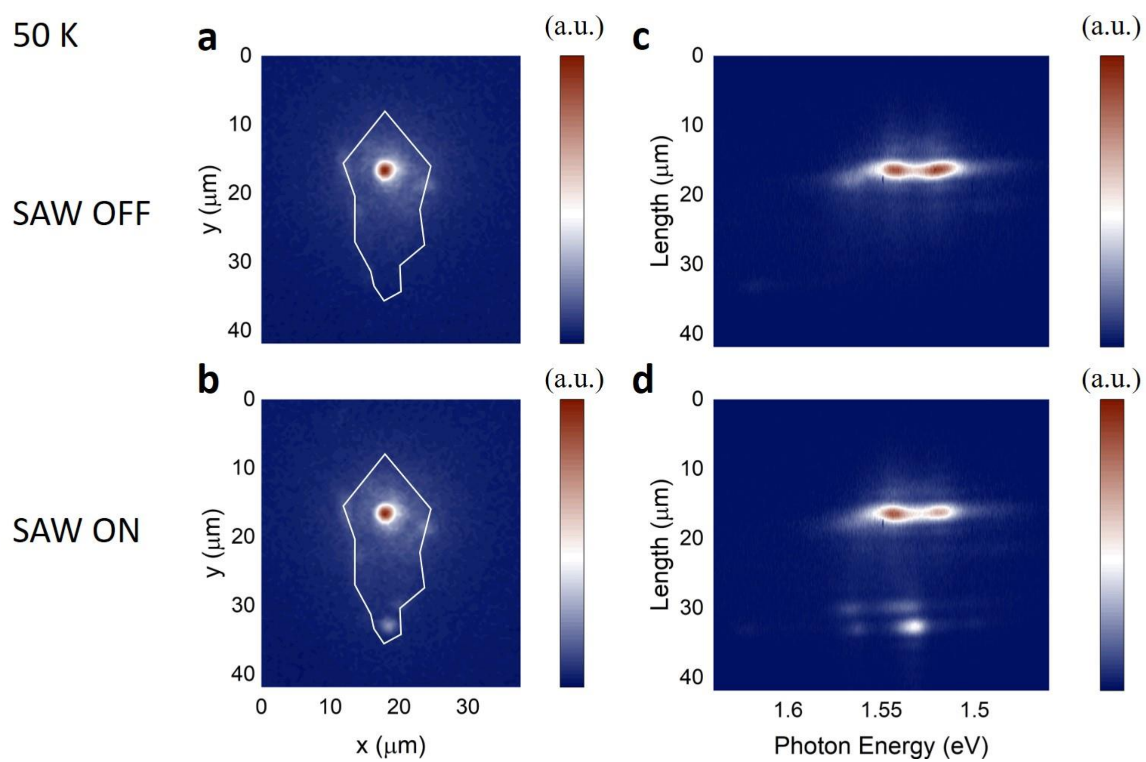

Figure A.5. Exciton transport of bilayer WSe_2 at 80 K.

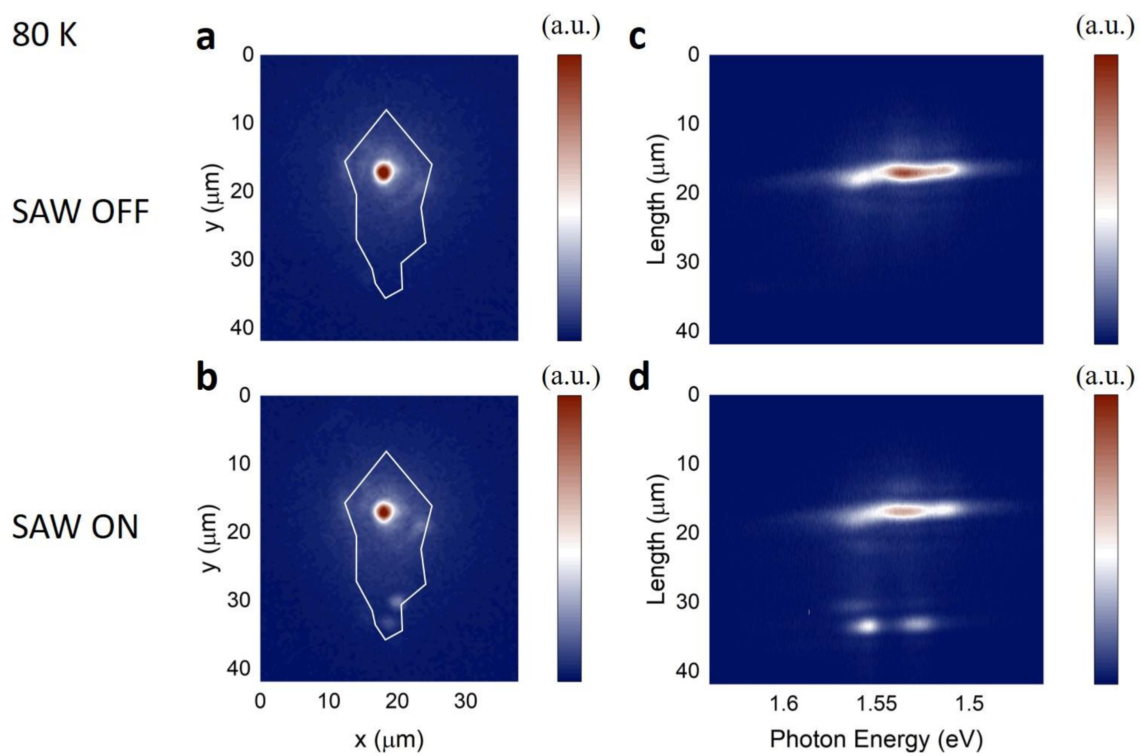

Figure A.6. Exciton transport of bilayer WSe_2 at 120 K.

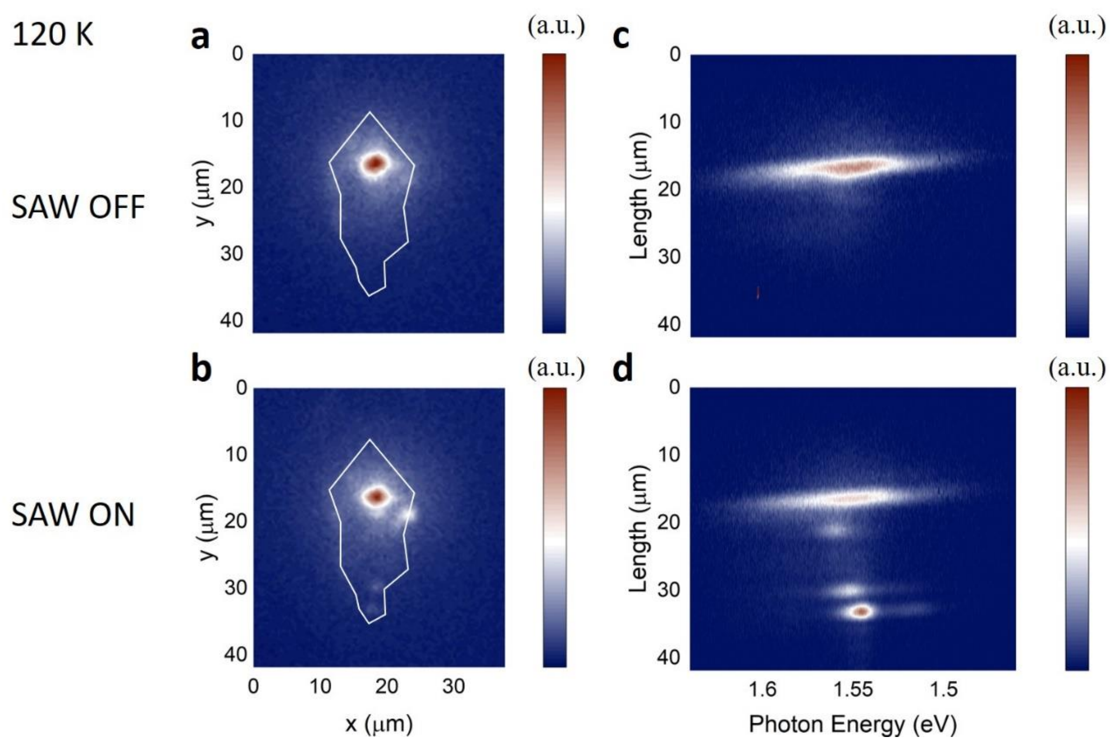

VITA

Ruoming was born in Huangshi, China which is located in southeastern Hubei province, primarily along the southwestern bank of the Yangtze River. He received a bachelor's degree in Microelectronics from the University of Electronic Science and Technology of China. In 2015, Ruoming started the journey of the Ph.D. in Electrical Engineering at the University of Minnesota under the supervision of Prof. Mo Li and then transferred with the Li group to the University of Washington in 2018. He has developed broad interests in semiconductor physics especially 2D semiconductors including black Phosphorus and TMDCs during his Ph.D. career. Ruoming was awarded Clairmont L. Egtvedt Endowed Engineering Fellowship in 2020 and also the Materials Research Society travel grant in 2021. After graduation, Ruoming will join Prof. Tian Zhong's group at the University of Chicago and focus his research on integrated quantum photonics.